8-4-2020

Catalyst-free Heteroepitaxy of III-V Semiconductor Nanowires on Silicon, Graphene, and Molybdenum Disulfide

Mohadeseh Asadolahi Baboli
mxa9934@rit.edu

RIT

Catalyst-free Heteroepitaxy of III-V Semiconductor Nanowires on Silicon, Graphene, and Molybdenum Disulfide

by

Mohadeseh Asadolahi Baboli

A dissertation submitted in partial fulfillment of the requirements

for the degree of Doctorate of Philosophy in Microsystems Engineering

Microsystems Engineering

Kate Gleason College of Engineering

Rochester Institute of Technology

Rochester, New York

August 4, 2020

Catalyst-free Heteroepitaxy of III-V Semiconductor Nanowires on Silicon, Graphene, and Molybdenum Disulfide

by

Mohadeseh Asadolahi Baboli

Committee Approval:

We, the undersigned committee members, certify that we have advised and/or supervised the candidate on the work described in this dissertation. We further certify that we have reviewed the dissertation manuscript and approve it in partial fulfillment of the requirements of the degree of Doctorate of Philosophy in Microsystems Engineering.

Parsian K. Mohseni, Ph.D. — Date
Assistant Professor, Microsystems Engineering

Karl D. Hirschman, Ph.D. — Date
Professor, Department of Electrical and Microelectronic Engineering

---

Seth M. Hubbard, Ph.D. — Date
Professor, Physics

Santosh K. Kurinec, Ph.D. — Date
Professor, Department of Electrical and Microelectronic Engineering

Certified By:

Bruce W. Smith, Ph.D. — Date
Director, Microsystems Engineering

Abstract

Kate Gleason College of Engineering

Rochester Institute of Technology

Degree: Doctor of Philosophy **Program:** Microsystems Engineering

Author's Name: Mohadeseh Asadolahi Baboli

Advisor's Name: Parsian K. Mohseni, Ph.D.

Dissertation Title: Catalyst-free Heteroepitaxy of III-V Semiconductor Nanowires on Silicon, Graphene, and Molybdenum Disulfide

The research presented in this dissertation pioneered three novel nano-material systems, including vertically aligned InAlAs nanowires (NWs) on two-dimensional (2-D) graphene, InAs NWs on 2-D MoS_2, and GaAsP NWs on Si using metalorganic chemical vapor deposition (MOCVD). Bottom up integratiton of NW structures enable heteroepitaxy of largely dissimilar III-V compounds on foreign substrates and provide a basis for design of high-performance devices that are otherwise inaccessible using thin-films or planar geometries. During conventional heteroepitaxy of planar geometries, strict constraints are imposed by the need to match lattice parameters, thermal expansion coefficients, and polar coherence between adjacent dissimilar materials. Semiconductor III-V NWs with small substrate footprints can permit relief of lattice mismatch-induced strain in heteroepitaxial systems. Thus, high crystalline quality III-V compound semiconductor NWs can be monolithically integrated with foreign substrates for novel electronic and optoelectronic device designs.

This dissertation presents wafer-scale production of vertically oriented $InAs_yP_{1-y}$ and $In_xAl_{1-x}As$ NWs on single layer graphene (SLG) and MoS_2 substrates, grown via pseudo-van der Waals epitaxy (vdWE). The morphology, areal density, and crystal

structure of $InAs_yP_{1-y}$ NWs within the $1 \leq y \leq 0.8$ range and $In_xAl_{1-x}As$ in the $1 \leq x \leq 0.5$ range are quantitatively analyzed by mapping a wide growth parameter space as a function of growth temperature, V/III ratio, total precursor flow rate, and molar flow ratio of precursors. Furthermore, through manipulation of growth kinetics, selective-area vdWE of III-V NWs on 2-D MoS_2 surfaces is demonstrated, and pattern-free positioning of single NWs on isolated MoS_2 micro-plates with one-to-one NW-to-MoS_2 placement is highlighted. Here, the highest axial growth rate of 840 nm/min and NW number density of $\sim 8.3 \times 10^8$ cm^{-2} for vdWE of high aspect ratio (>80) InAs NW arrays on graphitic surfaces is reported.

Additionally, selective-area epitaxy (SAE) of GaAsP-GaP core-multi shell NW arrays on patterned Si(111) substrates is reported. The composition of $GaAs_yP_{1-y}$ NWs is tuned toward a targeted value of $y = 0.73$ to achieve the bandgap of 1.75 eV. The effect of growth rate on morphology, total yield, and symmetric yield of GaAsP NWs is explored through modulation of the effective local supply of growth species. Under the optimized SAE growth condition, $> 90\%$ yield of hexagonally symmetric GaAsP NWs on Si is realized using a 100 μm $\times$ 100 μm field of nano-hole arrays in the center of a 400 μm $\times$ 400 μm mesa with border width of 100 μm.

Acknowledgments

I am momentously grateful to my thesis advisor, Prof. Parsian Mohseni, for his invaluable guidance, support and encouragement throughout the years of collaboration. I would like to express my utmost gratitude for his excellent mentorship. His valuable insight and passion for research has always been a source of inspiration for me.

I would like to express my sincere gratitude toward my thesis committee member, Prof. Seth Hubbard, Prof. Karl Hirschman, and Prof. Santosh Kurinec, for their instrumental guidance. I very much appreciate support and help of all of my collogues and friends at NPRL, SMFL and Microsystem engineering program. I would like to thanks my research group members, Dr. Tom Wilhelm and Alireza Abrand, for all the interesting collaborations and supports. I would like to recognize the invaluable technical assistance and support of Dr. Mike Slocum and Dr. Steve Polly on the MOCVD equipment. I am thankful for support and help of SMFL staffs, Thomas Grimsley, Patricia Meller, Sean O'Brien, Scott Blondell, Bruce Tolleson, John Nash, and Richard Battaglia. A special thanks to John Grazul and Mick Thomas of CCMR center at Cornell university for their technical training and support.

I wish to express my deepest gratitude to my family for their immense support and care, no word can describe how much I am indebted to them. I would like to thanks my partner, Mycahya Eggleston, for all of his support and encouragement, even from 2,281 miles away! I wish to show my appreciation to my friends, Karen, Anthony, Hillary and Yoshiko, for being source of inspiration and support throughout the years.

I would like to gratefully acknowledge Microsystems engineering program and national science foundation (NSF) for financial support.

Dedicated to my parents, Zinat Yahyapour and Ebrahim Asadolahi Baboli

Contents

List of Tables

List of Figures

Chapter 1

Motivations and Background

1.1 Motivations

Since the first methodical thermometer-based record of global temperature fluctuation in 1880, the average temperature of the Earth climate systems has been warming [1]. This change of temperature, known as global warming, causes adverse effects on human health and the environment [2], [3]. In search for the underlying cause of global warming, 97% of scientific papers expressing a position on this issue believe that human actions, such as emission of greenhouse gases including carbon dioxide, methane, and nitrous oxide, is the main reason [4], [5]. This scientific consensus often uses the term anthropogenic global warming (AGW) to emphasis on the role of human in this soon to be crisis and highlights the urge for taking actions. To mitigate the emission of greenhouse gases, 195 countries as part of the united nations framework convention on climate change (UNFCCC), agreed to keep the change in average global temperature below 2.0 °C in the present time, compared to the pre-industrial level and limit the increase to 1.5 °C. This historic climate accord is known as the Paris Agreement. The roadmap designed by the international renewable energy agency (IRENA), suggests that achieving this goal is technically possible if the global energy system transformed from mainly based fossil fuels to an alternative renewable energy that enhances efficiency [6].

Among different clean energy-conversion solutions, solar photovoltaics (PV) that

directly convert sunlight to electricity, offers the second largest cumulatively installed capacity [7]. Figure 1.1 shows how the total global cumulative installed PV capacity has changed through years. By the end of 2017 this value had reached to 415 gigawatt peak (GWp) with almost 25% increase in a year [7]. In the last 37 years, technological improvements and economies of scale have led to 24% reduction in price of PV modules with each doubling of the cumulated module production (Figure 1.2) [7]. While PV market has shown significant improvement, historically high cost-per-watt ($/W) of solar cells (SCs) productions has prevented PV to be able to compete with conventional power plants. To further decrease cost-per-watt ($/W) in the PV market, PV systems should either become less expensive or more efficient. For a PV system in utility scale, the module itself takes less than 50% of the total cost with the rest breaks down between different expenses such as wiring, inverters, labor, and land in use [7]. Since share of module cost is decreasing in a faster rate than other parts, it seems the

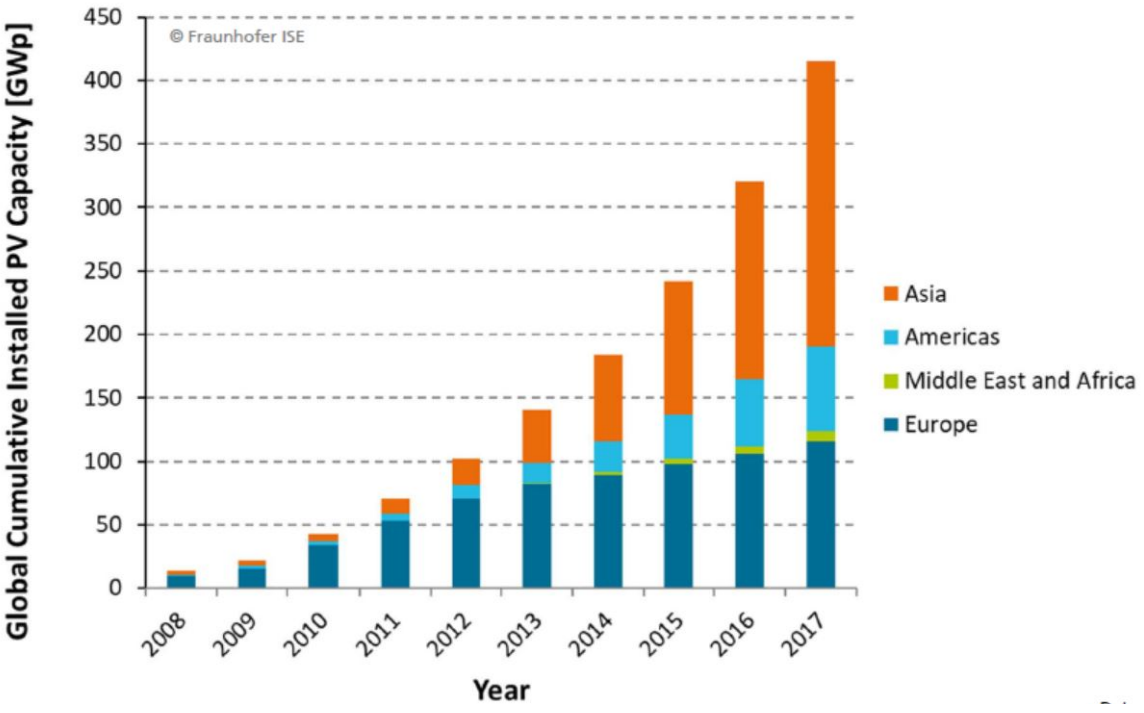

Figure 1.1: Global cumulative PV installation between 2008 and 2017. This graph shows the fast growth of PV, in different markets [7].

solution for a lower cost-per-watt ($/W) lies in realizing a PV module with higher efficiency but within the current cost margin.

Due to their low-cost and long-term stability, the current PV market is dominated by silicon-based cells that are capable of converting 8-19% of solar energy [8]. In contrast, other more expensive technologies such as III-V semiconductors multijunction SCs (MJSCs) offer high conversion efficiencies (>40%) [9]. One way to reach reasonable $/W is to integrate efficient III-V-based cells with the mature low-cost silicon modules. Theoretically such a two-junction cell architecture can reach more than 40% efficiency [10]. Though after two decades of research and development, the fundamental challenges are still impeding the realization of this concept. One of the main challanges in integraiton of planar III-V epilayer on Si substrate is the difference between crystal lattice constant and thermal expansion coefficient of these two material systems. One way to overcome these challenges is to use nanostructures such as nanowires as the active medium in SC devices. In this way, the requirement

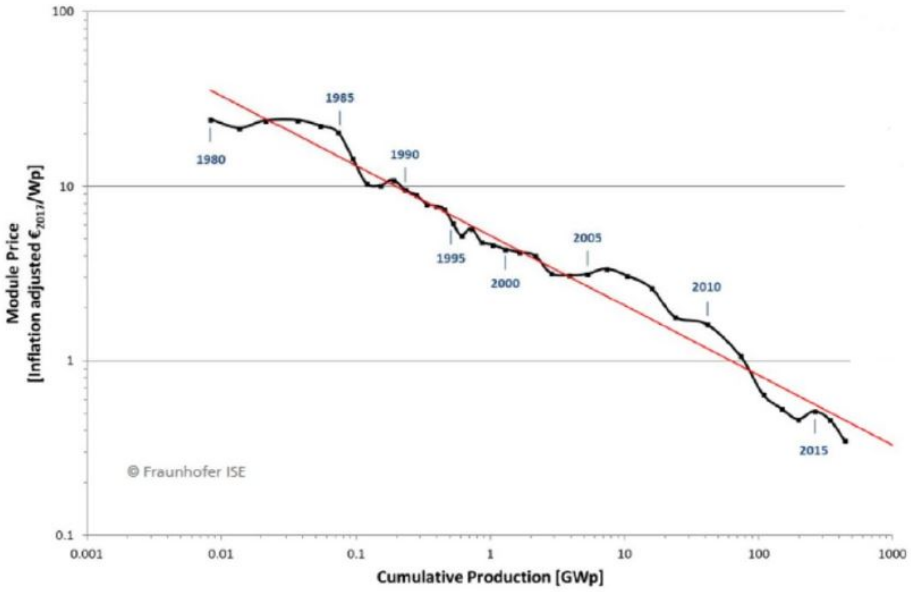

Figure 1.2: The price learning curve for PV module price in the market between 1980 and 2015. The Y-axis shows module price in logarithmic scale, the X-axis represents cumulative power production. By doubling the cumulative production, module price has experienced 24% reduction [7].

of the lattice matching criteria is reduced and novel designs for optoelectronic devices can be implemented.

1.2 Challenges for Heteroepitaxy of Planar III-Vs-on-Si

Different approaches for integration of planar III-V films on Si have been introduced. Since GaAs is one of the most studied and used substrates in MJSCs, realizing GaAs-on-Si as a platform for growth of following top layers was one of the initial approaches [44, 45]. Among other techniques is metamorphic SiGe graded buffer layers as a bridge between GaAs and Si lattice constants. However, the low band gap of such a buffer layer limits the application of Si to an inactive substrate and prevents Si to be used as an active subcell. Choice of buffer layers with larger bandgap such as GaAsP can solve this problem. Other approaches include: (1) lattice matched dilute nitrides GaAsPN on Si [46], (2) lattice mismatched InGaN-on-Si [47]. In this section critical challenges in heteroepitaxy of planar III-Vs on Si is discussed.

Mismatch in Lattice Constant and Thermal Expansion Coefficient The inherent variance in lattice constant and thermal expansion coefficient between III-V compounds and Si leads to crucial challenges in heteroepitaxy of III-V films on Si. For example, GaAs and Si have large lattice mismatch of 4%, and large difference in thermal expansion coefficient with 2.6×10^{-6} $^{\circ}C^{-1}$ for Si versus 5.73×10^{-6} $^{\circ}C^{-1}$ for GaAs. This large variation in basic films parameters translates into incorporation of defects and dislocations including antiphase domains, twinning and stacking faults, misfit and threading dislocations. Such a degradation in quality of epitaxial layers have a critical influence on performance of SCs by decreasing the minority carriers lifetime. Multiple approaches are introduced for reducing the threading dislocation density in GaAs-on-Si, such as thermal cycle annealing [48], and increasing GaAs buffer layer thickness [44]. The mismatch in thermal expansion coefficient can cause microscopic size cracks in the GaAs film. These cracks can introduce limitation in cell

size and performance, and overall reduces the reliability of devices. Optimizing the cooling process in a controlled fashion is one of the ways to minimize density of cracks.

Difference in Polarity of III-Vs and Si

Another critical challenge in achieving III-V-on-Si SC platform is formation of antiphase domains (APDs) during heteroepitaxy of polar III-V compounds (e.g. GaAs) on non-polar Si substrate. This type of crystallographic defects initiates from antisite defects at the monoatomic steps located at the top surface of the substrate. For instance, in the specific case of GaAs on Si, Si atoms form dimers in perpendicular directions along a step. By initiating the III-V growth, As atoms (or Ga atoms) follow the Si dimers directions, which results in As-As (or Ga-Ga) bonds. This extension of antisite defect from Si to the III-V layer causes the APDs to shape. In heteroepitaxy of thin films, one way to minimize density of APDs is to use offcut substrates [49].

Limitation in Design of Buffer Layer

Incorporation of buffer layers in a PV modules limits the choice of layer material, design criteria, and fabrication cost. For the specific case of cells based on III-V-on-Si, in order to use the Si substrate as an active cell, the buffer layer should be optically transparent. For this reason, the wide bandgap GaAsP graded buffer layer is a better option than narrow bandgap SiGe layer. In addition, it is important to minimize the series resistance by choosing a material with high electrical conductivity for the buffer layer. This is in specific important for the case of concentrator MJSCs. Another criteria is that the selected buffer layer material should offer good surface passivation for a Si sub-cell and can function as a window layer. In order to bridge the lattice constant of Si and III-Vs, generally thick buffer layers are designed which add additional fabrication cost. To compensate this problem, dilute nitride buffer layers, such as GaAsPN, and strained layer superlattice for GaAs-on-Si are introduced. These techniques allow design of a thinner metamorphic buffer layer. Therefore, there are restricted tradeoffs for designing a thin, optically transparent buffer layer than can

deliver minimized dislocation density, with good electrical conductivity and surface passivation characteristics.

1.3 Heteroepitaxy of Semiconductor Nanowires on Foreign Substrates

Nanowire (NW) morphologies enable heteroepitaxy of largely dissimilar III-V compounds and provide a basis for design of high performance electronic [11], [13] and photonic [12, 13] devices that are otherwise inaccessible with planar structures. During conventional heteroepitaxy of planar geometries, strict constraints are imposed by the need to match lattice parameters, thermal expansion coefficients, and polar coherence between adjacent dissimilar materials. For example, tetragonal distortion suffered at the hetero-interface of two cubic compounds with largely incongruent lattice parameters results in the formation of misfit and threading dislocations after relaxation of the epilayer beyond a pseudomorphic critical thickness. Several approaches are available in thin film technology to overcome this fundamental limitation, such as growth of compositionally graded buffer layers [14–16], epitaxial lateral overgrowth [17–19], and aspect ratio trapping [20–22]. Although such techniques successfully achieve heterogeneous integration while preserving high crystalline quality, they also introduce additional pre-growth processing steps and/or require growth of passive layers, which add design complexity and increase fabrication costs. On the other hand, high aspect ratio structures with large surface area-to-volume ratios, such as NWs, offer the potential for elastic relaxation via strain accommodation along their free surfaces [23–25]. Consequently, without sacrificing the crystal quality or introducing cost- intensive fabrication steps, III-V semiconductor NWs can be directly integrated with various foreign substrates such as Ge [26], Si [27–29], glass [30], and even flexible carbon-nanotube composite films [31, 32]. A summary of research conducted by the author on growth of III-V NWs on foreign substrates is illustrated in Figure 1.3. Except for the case of planar GaAs NWs, epitaxial growths of NWs exhibited in Figure 1.3 are carried out by the metalorganic chemical vapor deposition (MOCVD)

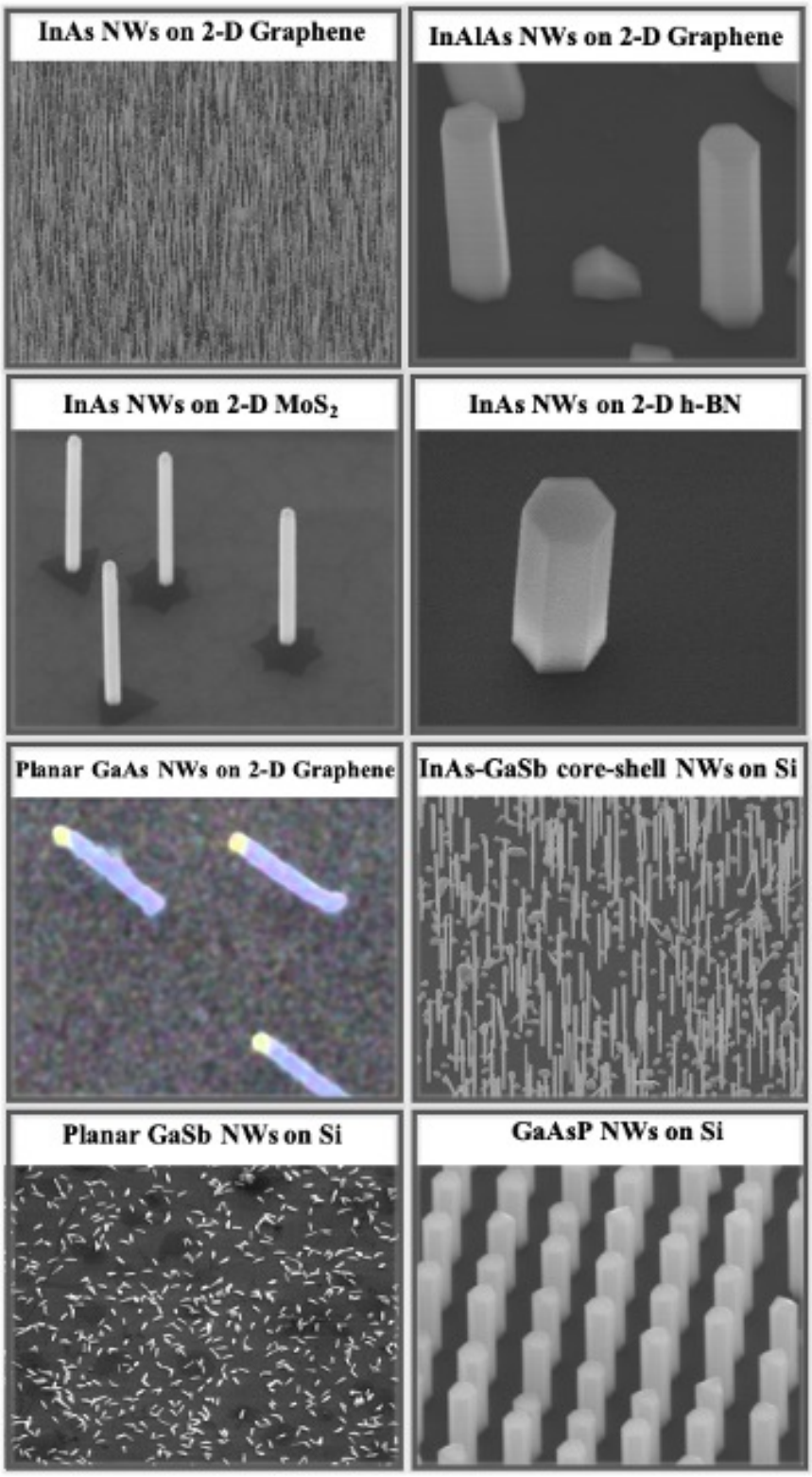

Figure 1.3: Various III-V semiconductor NWs grown on foreign substrates.

tool at RIT. This dissertation focuses on three material systems. In particular, growth and optimization of InAs-based NWs on graphene is presented in Chapter 3. The first realization of InAs NWs on molybdenum disulfide (MoS_2) nanohybrid system is reported in Chapter 4.

Semiconductor NWs in contrast to their thin film counterparts can be adapted to more highly lattice-mismatched material systems. This is mainly due to their small foot-print, which equip NWs with excellent strain tolerance from differences in thermal expansion and lattice constants between NWs and the substrate. Semiconductor NWs have been used in different applications such as photovoltaic cells [33] light-emitting diodes [34], and lasers [35]. Studies show that arrays of III-V NWs are a promising platform for fabrication of SCs thanks to their crystal structure tunability with growth conditions, advanced light absorption due to their large surface area to volume ratio, and design flexibility for maximizing the light-matter interactions [36].

Furthermore, photovoltaic cells with NW configuration are cost-efficient because while consuming less material compared to thin film heterostructure they can still exhibit high absorption efficiency. Wallentin et al. reported an InP NW array-based

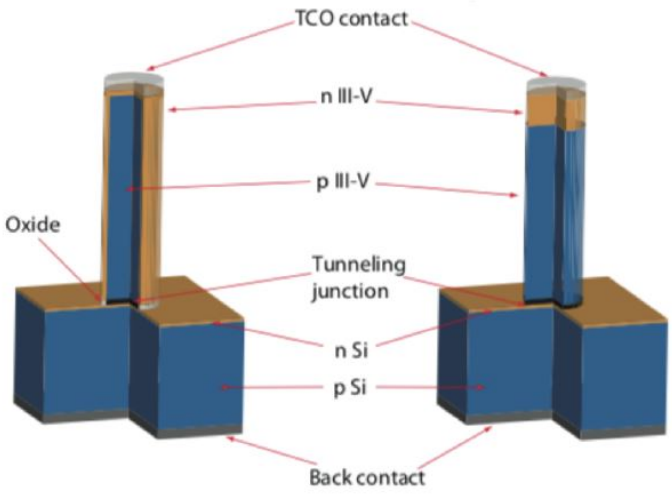

Figure 1.4: The two common doping profile in NW structures are in form of axial or radial geometries. Different components of tandem SCs based on NW on Si [37].

SC that generates short-circuit current of about 83% of the best planar InP cells with only 12% surface coverage [33]. Development of various NW based photovoltaic cells were reported in literature using binary or ternary III-V compounds such as InP, GaAs, InGaAs, and InGaP [33], [38–40].

In addition, the ability to control the physical and chemical states of NWs including length, diameter and alignment of nanowires as well as their elemental composition allows for tunable optical and electrical properties of optoelectronic devices. The two common NW heterostructures are in axial or radial geometries, shown in Figure 1.4. For axial heterostructures, growth species and dopant precursors are changed during NW epitaxy. In contrast, radial geometries can be realized by changing growth conditions (e.g., growth temperature, V/III ratio, etc.) to promote radial growth on a core NW segment similar to film growth. Specifically, epitaxy of core segment material at high temperature is followed by shell segment growth at lower temperature on NW sidewalls. For PV cells based on NWs, axial or radial p-i-n junctions can be achieved for various type of material systems and doping species. Reviews on NW growth and their device applications can be found in [36], [41–43].

1.4 Nanowires for Photovoltaics Applicaitons

1.4.1 Ideal Solar Cell Device Operation

The Sun, with surface temperature of 5777 K, emits radiation like a black body which can be described with Planck's radiation law shown in Equation 1.1 [38]

$$I_{\mathrm{A}} = \frac{2\pi hc^2}{\lambda^5}\left(\frac{1}{e^{\frac{hc}{\lambda kT}}-1}\right) \tag{1.1}$$

Where λ and c are the wavelength and speed of light, respectively. T is temperature, k and h are the Boltzmann and Planck constants, respectively. Based on Equation 1.1, the solar energy spectrum that PV panels installed on satellites utilize is equivalent to the spectra plotted in Figure 1.5, labeled as AM0 [32]. For the case of terrestrial SCs, photons passing through atmosphere experience different diffraction and absorption phenomena, resulting in changes of solar spectra intensity

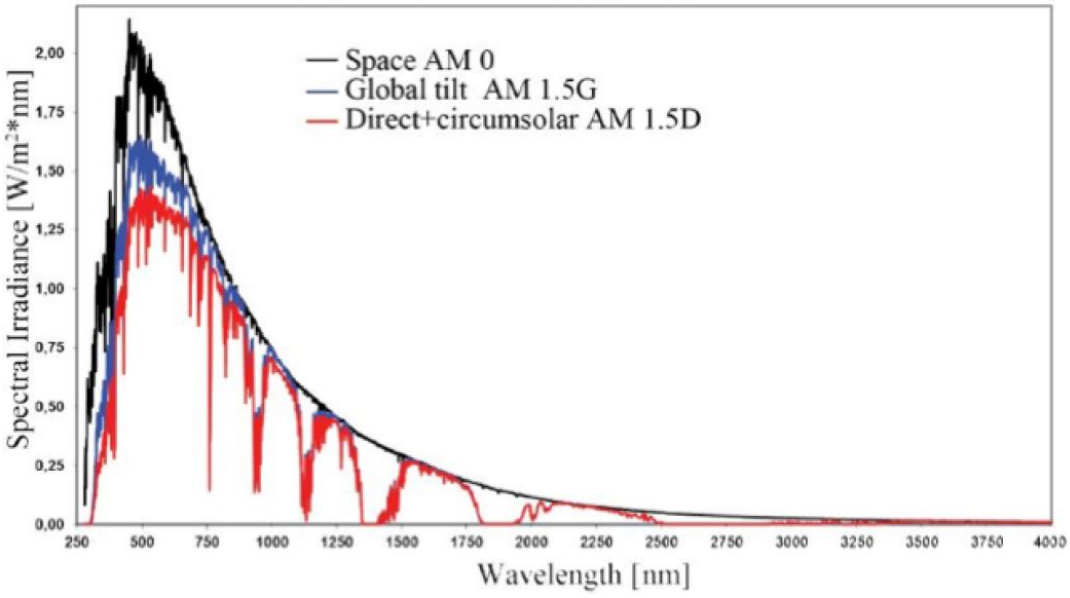

Figure 1.5: Solar spectrum as a function of wavelength for three scenarios. The plot in black illustrates solar spectrum outside Earth's atmosphere, known as AM0. The spectrum plotted in the blue line shows AM 1.5G which is related to direct and difused sunlight hitting a surface on Earth sitting at an angle equal to 37°. AM 1.5D, shown in red line, has the same definition as AM 1.5G except it only considers direct light [32].

similar to AM 1.5D, considering only diffused sunlight, and AM 1.5G, taking both direct and diffused lights into accounts. These spectra are illustrated in Figure 1.5. Considering various atmosphere thickness and relative positioning of Earth and sun angle, PV modules in different locations on Earth experience dissimilar intensity of solar spectrum. In order to be able to compare a variety of PV modules, a standard solar spectrum is used for SC performance measurements. A solar simulator is a light source that produces integrated power of 100 mW/cm^2, defines as 1-Sun intensity, with an air mass 1.5 global (AM1.5G) spectrum, shown in Figure 1.5.

Solar cells (SCs) are a type of optoelectronic device that convert the energy of sunlight into electrical energy in two main steps. First, partial absorption of incident photons within the solar spectrum, with energies higher or equal to the bandgap energy of cell material, allows electron excitation from the valence to the conduction band and generation of holes in the valence band. The introduced external energy of photons to the system (i.e. energy difference between electrons and holes) would ultimately disperse as carrier recombination, meaning energy in sunlight converts to the undesirable thermal energy. Before this happen, the task of the SC device is separate the photo-generated carriers, and promote their recombination via an external circuit where the released energy can be put in a desirable work. This task can be done by incorporation of a p-n-junction in a PV cells.

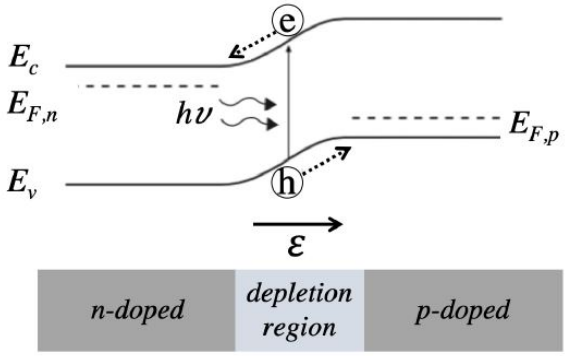

Figure 1.6: A simple schematic of a p-n junction and the corresponding band alignment.

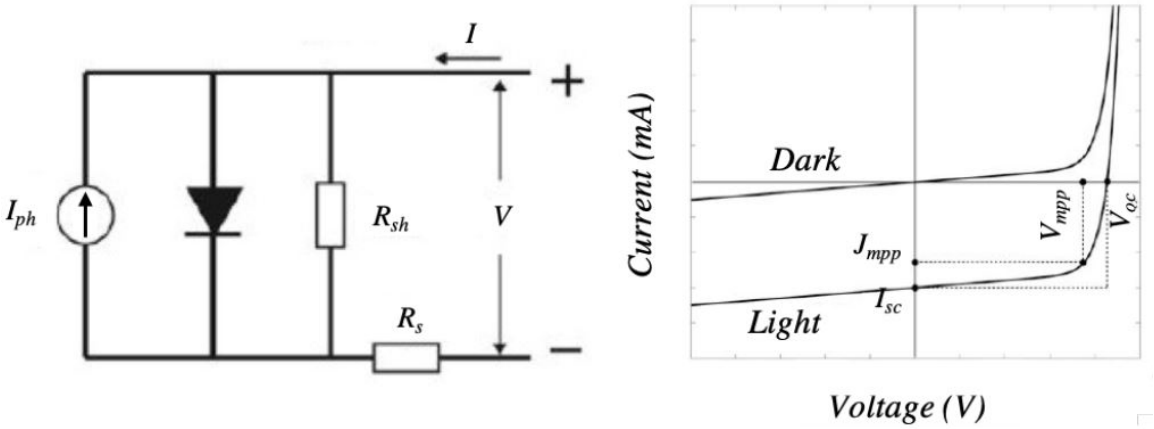

Figure 1.7: (a) A circuit model for a semiconductor PV cell, (b) A typical characteristics plot of a SC showing the dark- and light- I -V curves.

Shown in Figure 1.6 is a simple schematic of a p-n junction and the corresponding band alignment. The electric field in the depletion region of the p-n-junction (shown as ε) promotes drift of electrons to the n-side (n-doped region) and holes to the p-side (p-doped region). This results in generation of the photocurrent, Iph. As the built-in electric field in the depletion region of a p-n junction restricts the current to flow only in one direction, a p-n-junction can essentially be modeled by a rectifying diode. Figure 1.7 (a) illustrates circuit model for a typical semiconductor PV cell. Increasing the applied bias voltage at SC terminal counteracts the built-in potential difference at the junction, reducing the barrier for diffusion current to across the junction. This leads to an exponential boost in forward bias current [50]. Thermally generated carriers, on the other hand, flow in the reverse bias condition of the diode and drift through the built-in potential. The photogenerated current, is modeled as an ideal current source parallel to diode and opposing its diffusion current (Figure 11.7(a)). As in a typical electric circuit, the ideal current source shifts I -V characteristics on the I axis. For an ideal cell, the *I-V* characteristics under sunlight is a superposition of a simple diode under no light, i.e. dark I-V, and the generated photocurrent under

sun, formulated in Equation 1.2 and illustrated in Figure 1.7(b)

$$J = J_0(e^{\frac{ev}{nkT}} - 1) - J_{\text{ph}} \tag{1.2}$$

In Equation 1.2, J_0 and J_{ph} are the p-n-junction saturation current density and photo generated current density, respectively. T is cell temperature, k and n are Boltzmann constant and ideality factor, respectively. This equation shows the current density of a SC connected to an external circuit with cell terminal voltage of V. Use of current density (J) notation instead of current (I), makes performance comparison between different cells be independent of cell size.

A typical current-voltage (I -V) characteristics plot of a SC is shown in 1.5(b). Such a plot reveal characteristic information about a cell. The I -V characteristic can be produced for a cell under illumination from a solar simulator (light I -V) or absence of light (dark I -V). To produce such a plot, voltage at terminals of a SC are kept constant and the resulting current is measured. To quantify the performance of a PV cell, and be able to compare performances of different cells, a series of parameters can be extracted from the measured I -V curve. These parameters are: recombination current densities in the quasi-neutral regions and surfaces ($J_{0,1}$) and in the space-charge regions ($J_{0,2}$), ideality factors n_1 and n_2 , series resistance (R_s), and the shunt resistance (R_{sh}). In addition to these parameters, open-circuit voltage (V_{OC}), short-circuit current (I_{SC}), filling factor (FF), maximum power point (MPP), and power conversion efficiency (PCE) are other important measures. The interception of the I -V curve and the axes are the two extremes scenario in an ideal SC model: (1) cell is connected to zero load (V = 0) which results in short-circuit current density (J_{sc}) (Equation 1.3), and (2) case of an external circuit with an infinite load (J = 0), leading to the V_{OC} characteristic (Equation 1.4).

$$J_{\text{sc}} = J_{\text{ph}} \tag{1.3}$$

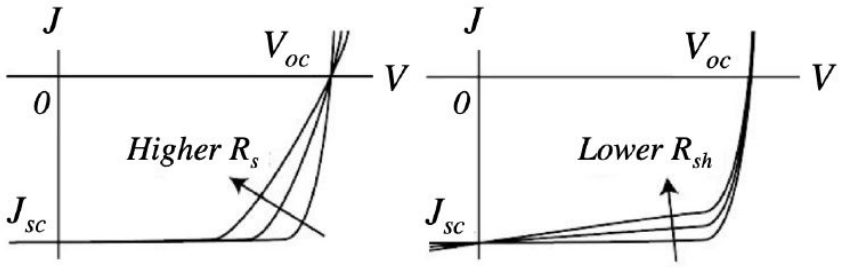

Figure 1.8: The adverse effect of impedance phenomena on the FF.

$$V_{\mathrm{OC}} = \frac{nkT}{q} ln(\frac{J_{\mathrm{sc}}}{J_0} + 1) \tag{1.4}$$

Here, q stands for the elementary charge and all other variables are defined above. The PCE for SCs is defined as the ratio of maximum output power to the total incident power upon the cell (Equation 1.5). The output power is maximized when the product of cell current and voltage is maximized, denoted as $\mathrm{J_{mpp}}$ and $\mathrm{V_{mpp}}$, respectively. Another measure of SC performance is the *FF*, which defines how well photogenerated charges can be extracted from the cell, and it can be calculated with Equation 1.6

$$PCE = \frac{P_{\mathrm{out}}}{P_{\mathrm{in}}} = \frac{J_{\mathrm{mpp}} \times V_{\mathrm{mpp}}}{P_{\mathrm{in}}} = \frac{J_{\mathrm{sc}} \times V_{\mathrm{oc}} \times FF}{P_{\mathrm{in}}} \tag{1.5}$$

$$FF = \frac{J_{\mathrm{mpp}} \times V_{\mathrm{mpp}}}{J_{\mathrm{sc}} \times V_{\mathrm{oc}}} \tag{1.6}$$

The recombination processes in the depletion region [50], [51] or at grain boundaries [52] of cell material can be modeled as a parasitic resistance parallel to the diode (R_{sh}). Another type of parasitic phenomena is the impedance at the cell contacts that can be modeled as a series resistance (R_s). For a solar cell to act as an ideal current source-rectifier diode, the R_{sh} should have an infinite value, whereas, Rs should have a minimum value. These impedance phenomena adversely affect the *FF*. From the system point of view, effect of these parasitic resistors are evident by looking at a

typical *I-V* characteristics of a PV cell. This is illustrated in Figure 1.8. The decrease in *FF* due to increase in R_s, is shown in Figure 1.8 where the slope of the *I-V* curve changes without any alteration in the value of V_{oc}. In general, the slope of an *I-V* curve at $\mathrm{V_{oc}}$ is a fair quantitative estimation value for R_s. In contrast, increase in curve slope near J_{sc} of an *I-V* characteristics is associated with increase in the $\mathrm{R_{sh}}$, leading to decrease in *FF* and, therefore, reduction in PCE.

1.4.2 Light Management in Nanowire Solar Cells

The percent of reflected sunlight form the top surface of SCs depends on the wavelength and angle of incoming light, as well as the cell material. There are two main techniques to reduce this type of loss mechanism, (1) anti-reflection coating (ARC), (2) surface texturing. Regarding ARC technique, the refractive indices of coating and cell materials have relation similar to Equation 1.7

$$n_{\mathrm{ARC}} = \sqrt{n_{\mathrm{air}} n_{\mathrm{solar}}} \tag{1.7}$$

where $\mathrm{n_{ARC}}$, $\mathrm{n_{air}}$, and $\mathrm{n_{solar}}$ are refractive indices of ARC, air, and SC materials. To design a coating for a cell with absorption peak at λ, selection of film thickness in range of 4λ will permit maximum transmission at this wavelength. In other words, the more divergent the wavelength of a photon is from the central designed λ, the higher the probability of reflection will be. This allows filtering of a useful part of solar spectrum for solar cell through ARC layer on top surface of a cell. One of the challenges with ARC is that for cells without sun tracking systems, the incident angle of sunlight on a cell changes constantly throughout a day. To change the sensitivity of ARC material to incident angle and wavelength, multiple layers of ARC can be implemented. For a reasonable tradeoff between cost and efficiency, usually two ARC layers are used.

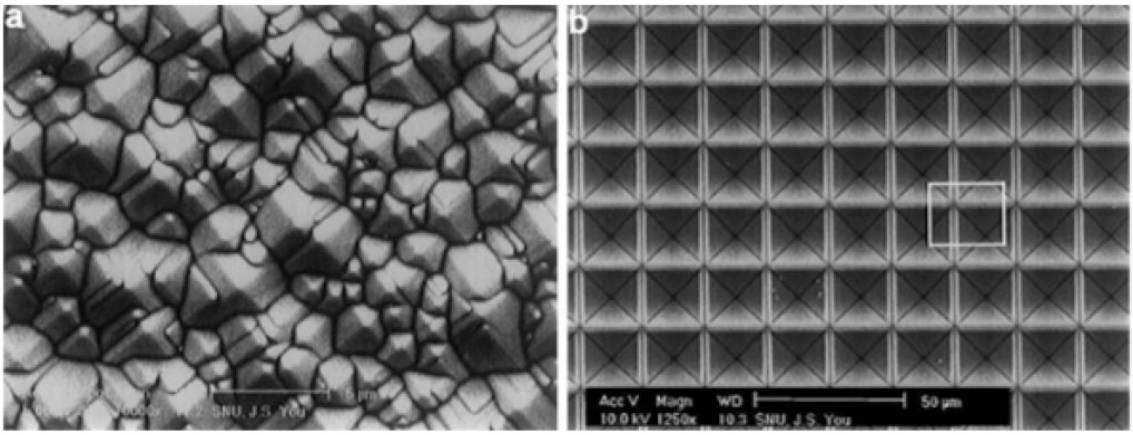

Figure 1.9: SEM images of (a) randomly distributed pyramids on a mono-Si (100) surface, (b) an uniform array of inverted pyramids [53].

Texturing, on the other, hand increases the chance of re-absorption of reflected beams. To design a cell with an optimum thickness, there is a tradeoff between absorption efficiency, material cost, and extraction efficiency. The thickness of a cell should be higher than a limit for majority of incoming photons, with energies higher than the SC material bandgap, to get absorbed. On the contrary, in addition to the need for minimizing material cost, and therefore PV module price, cells should be thin enough so that the photogenerated carriers can be extracted within a diffusion length of a p-n-junction. To overcome this issue, usually structures are designed to be physically thin but optically deep. This goal can be achieved by texturing the top and back surfaces of the cells. This allows the incoming beam to get trapped in the cell by multiple reflection events from the top and bottom surfaces. With an ideal scenario of a Lambertian reflector, optical path length of photons can be enhanced by factor of $4n_{solar}$ [48]. While implementing perfect texturing is very expensive, many PV modules in the market take adventure of simple texturing designs. For monocrystalline silicon (mono-Si) cells, pyramids texturing with random distribuiton can be obtained by anisotropic etching in alkaline soluiton.

An example of such surface texturing is shown in Figure 1.9(a). An uniform array of inverted pyramids can be realized on the surface of a cell by applying an etching

mask, illustrated in Figure 1.9(b) [53]. In contrast, these texturing mechanisms are not suitable for polycrystalline silicon (poly-Si) based PV cells. Instead, reactive ion etching [54] and wet etching [55] are used for texturing poly-Si cells. For instance, hydrofluoric acid (HF) and nitric acid (HNO_3) isotropically etch poly-Si wafers resulting in rounded surface features [55].

For planar SC structures, coupling of sunlight into the cell for a broad range of wavelengths and angles is a major challenge. To compensate optical loss mechanism originated from reflection of sunlight at the top surface of SCs, it is a common practice to use ARCs. But in this method, it is challenging to absorb a broad wavelength range. Broad band antireflection approaches can be realized by surface texturing to increase the light trapping in cells. For example, inverted pyramid structures are known as very effective texturing methods, but they add complexity to the fabrication process and therefore increase cell cost [56–58].

In contrast, cell structures based on NWs show strong antireflection capabilities for different wavelength, polarization and angles of incident. It is well studied that a vertical array of NWs show higher absorption ability than the same amount of material in planar configuration. For instance, for a planar Si SC without any antireflection coating or texturing treatment, nearly 30% of incoming sun light can be reflected and be lost [59]. For wavelengths below 700 nm, Tsakalakos et al. showed reflectance measurements from Si samples with and without Si NWs showed superior absorption for samples with NWs. In particular, reflectance for samples with Si film was more than 30%, this value reduced to 5% for samples with Si NWs [60]. In a similar study, Garnett et al. observed a 2.9 to 7.8 times reduction in transmission over the broad range of 600 to 1100 nm for samples with NWs with average length of 2 μm in comparison with planar Si film samples [61]. They also showed that this transmission reduction factor between Si NW and film sample can be further maximized to factors of 12-29 simply by increasing average NWs length to 5 μm [61].

Superior functionality of NWs as an absorber layer in PV cells originates from a combination of light interaction features that separates these nanostructures from planar bulk geometries. In general, an array of NWs shows excellent light trapping ability due to multiple scattering effect for a diffused beam into the absorbing medium.. In this way, a reflected beam of light from a NW surface can be absorbed by another wire. This leads to a longer optical path and wider effective absorption angle for cells based on NWs. Garnett et al. showed that for arrays of Si NWs, the optical path length of incident sunlight is 73 times longer than for bare Si wafer [61].

Another optical feature of NW arrays is their effective refractive index being between that of air and the substrate or the active underlying planar sub-cell [61, 62]. In this way, the incoming light does not experience an abrupt change in refractive index [62, 63]. For GaP NWs on AlInP/GaAs substrate, Diedenhofen et al. demonstrated enhancement in light transmission into the substrate as well as reduced reflectance for a broadband absorption for a wide range of incident angles [64]. Guo et al. optimized diameter (D), length (L), and filling ratio (D/P) to maximize absorption for vertical array of GaAs NWs [65]. They found that for D = 180 nm, L = 2 μm, and D/P = 0.5, the NW array demonstrates more than 90% absorption in visible light region. Zhang et al. showed that with light trapping ability of InGaAs NWs, the short-circuit current can be extended to 61.3 mA/cm^2, three times more than an equivalent thin-film layer [66]. Anttu et al. experimentally illustrated a PV cell based on array of vertical InP NWs with 96% of the ISC of a perfectly absorbent bulk InP SC [66].

1.4.3 Charge Collection and Transport in Core-Shell Nanowires

To achieve high PCE in a PV cell, the active layer must be optically thick to facilitate enhanced light absorption and electrically thin to facilitate carrier transport and collection. In other words, one of the challenges in planar bulk SCs is that photogenerated charge carries need to travel the depth (thickness) of a cell, to be collected by the

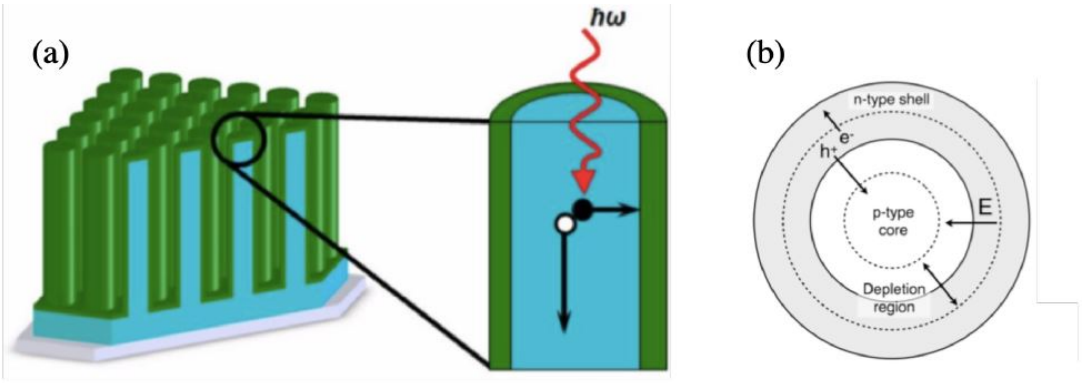

Figure 1.10: Carriers (a) collection and (b) transport in core-shell NW structure.

contacts. On the other hand, the carrier collection efficiency is strongly influenced by the minority carrier diffusion length, and therefore by density of defects in the cell, meaning in this type of cell architecture, for a cell with low recombination loss the crystal quality of the cell materials should be very high.

This challenge can be addressed by decoupling the optical path for absorption and electrical path for carrier transport and collection. Core-shell NWs enable light absorption along their length and carrier separation and collection by radial p-n (or p-i-n) junctions. This way, the distance that photo-generated carriers need to travel is in range of tens to hundreds of nanometer and is comparable with minority carrier diffusion length. This concept is depicted in Figure 1.10. While photons are absorbed along the length of NWs, the in-built electric field between core p-segment and shell n-segment, makes it possible for photogenerated charge carriers to be collected radially, perpendicular to the absorption of photos. This superiority of core-shell structures is most beneficial when the minority carrier diffusion length is shorter than optical absorption length of the cell material. As a result, NWs open the possibilities for fabrication of SCs based on materials with short minority carrier diffusion length, that are not suitable for planar NWs structure. Sulfides [67], oxides [68], and heavy doped Si [69] are some examples.

There are some challenges regarding core-shell NWs for PV applications. While

large surface area to volume ratio of NWs provides a critical advantage for heteroepitaxy, feature in excellency of NWs for heteroepitaxy, it makes NW SCs sensitive to depletion region recombination [70, 71]. By optimizing abruptness of p-i-n junction and crystallinity of shell segment, the V_{OC} of silicon NW based SCs was improved from 260 mV to 500mV, and the FF from 55% to 73% [11, 71]. Another design and growth optimization challenge is related to thickness and relative doping level in the core and shell segments. A thin core (or shell) segment containing low carrier concentration, can easily be depleted if the shell (or core) junction is more heavily doped. Another challenge is related to high density of surface states for NWs geometry with large surface to volume ratio. Here, it is worth noting that a theoretical study by Yu et al. illustrated the advantage of radial p-i-n architecture in III-V NW array SCs in comparison to cells based on NWs with axial junction structures. One possible explanation here is that unlike radial junctions configuration, in axial junctions the depletion region is exposed to the surface of wires.

1.4.4 Detailed Balance Limit for Solar Cells Based on Nano-Structures

Extensive studies have been done on calculating the limit of SC efficiency by means of investigating the underlying thermodynamics in conversion of solar energy to electrical work [72, 73]. In 1961, Shockley and Queisser applied the detailed balance theory and calculated the maximum solar conversion efficiency of 33.7% with the following assumptions: [72–74].

(i) A single p-n junction with bandgap energy of 1.34 eV under AM1.5 solar spectrum

(ii) The absorption function for the solar cell is a step function, meaning only photons with energy above the bandgap of the cell can be absorbed

(iii) For carriers with energy above the bandgap, thermal relaxation will happen

(iv) Radiative recombination is the only recombination loss mechanism

(v) The Sun's radiation spectrum is defined as a black body radiation with temperature T_{sun}

In addition to these assumptions, the detailed balance limit indicates that for a system at thermal equilibrium, absorption of every photon is accompanied by emission of an electron hole pair (EHP), and this absorption-emission balance is true for every frequency and solid angle. The direct implementation of the detailed balance limit for the case of SCs, however, is not realistic since the operating point of PV cells is far from thermal equilibrium. However, Shockley and Queisser found that the difference between the emission spectrum at equilibrium and non-equilibrium conditions can be compensated by using a scaling factor [72]. This idea was one of the main contributions toward understanding of the efficiency limit of SCs in 1961.

In general, recombination mainly takes place with two mechanisms; either it is a radiative recombination mechanism that produces a photon, or it is a non-radiative mechanism, which is a loss mechanism for the cell. However, the SQ limit only takes the former mechanism into account. The absorbed photons excite the valance band

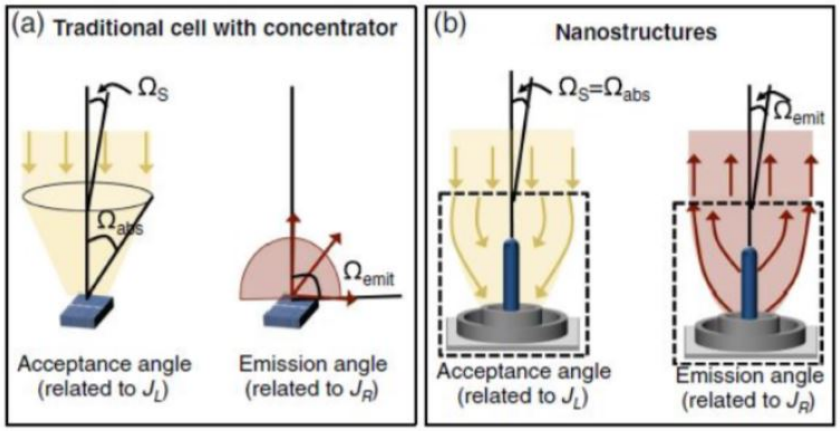

Figure 1.11: An illustration of how a nano-scale structure can minimize the entropy factor of $\Omega_{emit}/\Omega_{abs}$, (a) A conventional planar bulk solar cell with concentration optics can exhibit larger conversion efficiency than the same cell without a concentrator. This is because the $\Omega_{emit}/\Omega_{abs}$ criteria will decrease as Ω_{abs} increases and approaches Ω_{emit}, (b) A nanosructure photovoltaic cell uses opposite mechanism for diminishing the $\Omega_{emit}/\Omega_{abs}$ factor. small top surface area of a nano-scale SC results in minuscule emission angle [75].

electrons. For photons with energy larger than the bandgap energy, excited electrons lose their energy in the form of thermal energy and reach an equilibrium state with the solar cell lattice through the thermalization process. The reason for this change in energy is that excited electrons interact with lattice modes; after energy and momentum of electrons transfer to the SC lattice, they form a thermally equilibrium state with the lattice [76]. By applying an external voltage, these thermalized electrons either flow as electrical current or recombine with valence band holes and emit luminescent photons. Increasing the external voltage leads to enhanced luminescent recombination. At a certain external voltage all the absorbed photons convert to the luminescent. Hence this voltage is known as the open-circuit voltage (V_{OC}) as no electrical current can be generated and we only have radiative recombination. If we compare the electrons energies at the thermalized stage and at the V_{OC} condition, we can calculate the thermodynamic loss [76]. The open-circuit voltage can be calculated form Equation 1.8 [77].

$$qV_{\mathrm{oc}} = E_{\mathrm{g}}(1 - \frac{T_{\mathrm{c}}}{T_{\mathrm{sun}}}) - kT[ln(\frac{\Omega_{\mathrm{emit}}}{\Omega_{\mathrm{abs}}}) + ln(\frac{4n^2}{C}) - ln(QE)] \tag{1.8}$$

It is worth noting that V_{OC} is less than the bandgap energy. In order to understand the formulation of V_{OC}, we van separate the above relation into two terms. The first term on the left-hand side of 1.8 is based on Carnot's theorem that described the thermodynamics loss in photovoltaic conversion process, in which T_C is the cell temperature and T_{Sun} is the Sun temperature. The second factor is the effect of change in entropy on V_{OC}. There are three different terms related to entropy change. The first term (also the first term in the brackets) is related to the photon absorption and emission of the cell with, respectively, solid angles of Ω_{abs} and Ω_{emit}. This term indicates that the entropy increases because of the mismatch between these two angles that is generally the case for most solar cells. Hence, this term of entropy loss would be minimized if the emission angle become equal to the absorption angle of Ω_{abs}. This

concept is illustrated in Figure 1.11 by comparing the absorption and emission angles for a traditional cell with a concentrator and a nano-scaled solar cell. From this simple illustration it can be concluded that for a PV cell with NW structures, the V_{OC} and, consequently, the efficiency would increase due to near unity value of Ω_{emit}=Ω_{abs} [77].

For the second factor of entropy, n represents refractive index of the cell and C is the light concentration term. This factor demonstrates the relation of the V_{OC} with the light coupling capability of the device. Many different methods were suggested for increasing C to reach value of $4n^2$ such as use of surface texturing [78]. In 1982, Yablonovitch et al. proved that assuming classical ray optics limit the maximum possible amount of light concentration is $4n^2$ [79]. However, Munday et al., in 2011, showed that this limit can be exceeded by using nanostructures [80]. It should be noted than for photons with energy slightly more than the absorber's bandgap this factor has a large impact on their absorption as they would not absorb strongly by the nature of the material itself.

Finally, ln(QE) is included in V_{OC} calculation when the non-radiative recombination is taken into account. Here, the quantum efficiency (QE) is calculated by Equation 1.9

$$QE = \frac{R_{\text{rad}}}{R_{\text{rad}} + R_{\text{nrad}}} \tag{1.9}$$

When R_{rad} is the radiative recombination rate and R_{nrad} is the non-radiative recombination rate.

In 2015 [75], Munday et al. tried to revisit the SQ limit for nanostructured solar cells and asked an important question; is it possible for a non-third generation photovoltaic cell to exceed the SQ limit? The answer to this question can be crucial for avoiding the further misconception in the field of photovoltaics based on nanostructures such as nanowires and lead the direction of future researches into the right direction. Munday et al. suggested that nanostructured solar cells with any architecture such as wires, cones or pyramids are limited to the efficiency limit of a planar photovoltaic cell

with concentrating optics such as lens or parabolic mirrors. Also the only origin of the efficiency improvement is due to an increase in the V_{OC}. Based on the previously presented introduction, the SQ limit assumes that the radiative recombination is the only recombination mechanism. The maximum current of solar cell then can be written as seen in Equation 1.10,

$$I_{\text{total}} = q(N_{\text{abs}} - N_{\text{emit}}) \tag{1.10}$$

Where N_{abs} and N_{emit} are the numbers of absorbed and emitted photons per unit time by the solar cell, respectively, and q is the electron electric charge. The rates of absorption (N_{abs}) and emission (N_{emit}), can be calculated by Equation 1.11 [75].

$$N(\theta_{\max}, V, T) = \int_0^{\infty} \int_{\phi=0}^{2\pi} \int_{\theta=0}^{\theta_{\max}} \sigma_{\text{abs}}(\theta, \phi, E) \times F(E, T, V) cos(\theta) sin(\theta) d\phi d\theta dE \tag{1.11}$$

where $\theta_{\max}$ is the maximum angle for absorption or emission. Moreover, *F(E,T,V)* is photon flux, which can be calculated from the generalized Planck blackbody law [81] by Equation 1.12

$$F(E, T, V) = \frac{2n^2}{h^3 c^2} \frac{E^2}{e^{\frac{E-qV}{k_B T}} - 1} \tag{1.12}$$

where h, k_b, and c are respectively the Planck's constant, Boltzmann's constant and the speed of light. Also, n stands for the refractive index of the surrounding ambient, which is usually equal to zero for vacuum. In addition, in Equation 1.13, $\sigma_{\text{abs}}(\theta, \phi, \text{E})$ is the absorption cross-section, which is defined as the product of the top surface of the cell and the probability of photon absorption based on the photons energy and its angle of incidence (Equation 1.13)

$$\sigma_{\text{abs}}(\theta, \phi, E) = A_{\text{cell}} \times a(\theta, \phi, E) \tag{1.13}$$

The cross-section absorption for a typical bulk solar cell structure can be idealized to

a simple step function. In this case, the half-angle for cell emission is $\theta_{\max} = \theta_{\mathrm{c}} = 90^{\circ}$ and the half-angle of incoming light from the Sun at the Sun temperature of 5760 K is equal to $\theta_{\max} = \theta_{\mathrm{c}} = 0.267^{\circ}$ [82]. Thus, the photogenerated current and the dark current are calculated according to Equation 1.14 and Equation 1.15,

$$I_{\mathrm{L}} = qN(\theta_{\mathrm{s}}, T_{\mathrm{s}}, V = 0) \tag{1.14}$$

$$I_0 = I_{\mathrm{R}}[e^{\frac{qV}{k_{\mathrm{B}}T_{\mathrm{c}}}} - 1] = qN(\theta_{\mathrm{s}}, T_{\mathrm{s}}, V) - qN(\theta_{\mathrm{s}}, T_{\mathrm{s}}, V = 0) \tag{1.15}$$

where I_R stands for the reverse saturation current. Here we use the notation of I_L^{Bulk} and I_R^{Bulk} for the photocurrent and reverse current of an ideal bulk solar cell with the above stated angles and top surface area. On the other hand, one can increase the V_{OC} by increasing the photocurrent or reducing the reverse saturation current (Equation 1.16).

$$V_{\mathrm{oc}} = \frac{k_{\mathrm{b}}T_{\mathrm{c}}}{q} ln(\frac{I_{\mathrm{L}}}{I_{\mathrm{R}}} + 1) \approx \frac{k_{\mathrm{b}}T_{\mathrm{c}}}{q} ln(\frac{I_{\mathrm{L}}}{I_{\mathrm{R}}}) \tag{1.16}$$

Since, except the emission angle, all the other parameters in Equation 1.14 and Equation 1.15 remain the same from case of an ideal bulk SC and a NW-based SC, Munday et al. suggested a general absorption cross-section function as Equation 1.17

$$\begin{cases} \sigma_{\mathrm{abs}} = \sigma_{\max} & 0 < \theta < \theta_{\max} \\ \sigma_{\mathrm{abs}} = \sigma_{\min} & \theta_{\max} < \theta < \theta_{\mathrm{c}} \end{cases} \tag{1.17}$$

where θ_{m} is defined by the structure. As expected, absorption cross-section is defined as a step function for photon energies ($\sigma_{\mathrm{m}} = 0$ for $E<E_g$). Using Equation 1.11 the photocurrent and dark current of a nanostructured photovoltaic cell with

above parameters can be calculated by Equation 1.18 and Equation 1.19 [75] :

$$I_{\mathrm{L}} = qN(\theta_{\mathrm{s}}, T_{\mathrm{s}}, V=0) = q\sigma_{\max}\int_{E_{\mathrm{g}}}^{\infty}\int_{\phi=0}^{2\pi}\int_{\theta=0}^{\theta} F(E, T_{\mathrm{s}}, V=0)\times cos(\theta)sin(\theta)d\phi d\theta dE$$
$$= \frac{\sigma_{\max}}{A_{\mathrm{cell}}} I_L^{Bulk} \tag{1.18}$$

$$I_{\mathrm{R}} = qN(\theta_{\mathrm{c}}, T_{\mathrm{c}}, V=0) = \frac{\pi q\sigma_{\min}}{2}[cos(2\theta_{\mathrm{m}}) - cos(2\theta_{\mathrm{c}})]\times\int_{E_{\mathrm{g}}}^{\infty} F(E, T_{\mathrm{s}}, V=0)dE$$
$$+\frac{\pi q\sigma_{\max}}{2}[1 - cos(2\theta_{\mathrm{m}})]\times\int_{E_{\mathrm{g}}}^{\infty} F(E, T_{\mathrm{s}}, V=0)dE$$
$$= \frac{\sigma_{\max} + \sigma_{\min} + (\sigma_{\min} - \sigma_{\max})\times cos(2\theta_{\mathrm{m}})}{2A_{\mathrm{cell}}} I_L^{Bulk} \tag{1.19}$$

where θ_{m}=0 for E<E_g, $I_{L,0}$ is the light generated current for an ideal bulk cell with area A_{cell}. And then the open-circuit voltage will be as Equation 1.20

$$V_{\mathrm{oc}} = \frac{k_{\mathrm{B}}T_{\mathrm{c}}}{q} ln(\frac{2\sigma_{\max}}{\sigma_{\max} + \sigma_{\min} + (\sigma_{\min} - \sigma_{\max})\times cos(2\theta_{\mathrm{m}})})$$
$$+\frac{k_{\mathrm{B}}T_{\mathrm{c}}}{q}[ln(\frac{I_L^{Bulk}}{I_R^{Bulk}})]$$
$$= \frac{k_{\mathrm{B}}T_{\mathrm{c}}}{q}[ln(\frac{I_L^{Bulk}}{I_R^{Bulk}}) + ln(X)] \tag{1.20}$$
$$X = \frac{2\sigma_{\max}}{\sigma_{\max} + \sigma_{\min} + (\sigma_{\min} - \sigma_{\max})}$$

The factor X in Equation 1.20 is equivalent to the concentration factor for a bulk solar cell with a concentration optics. By maximizing this factor for $\theta_{\mathrm{m}} = \theta_{\mathrm{s}}$ and $\theta_{\min} = 0$ the concentration factor will be approximately equal to 46 and the maximum efficiency will be 42% for a nanostructured photovoltaic cell. This amount

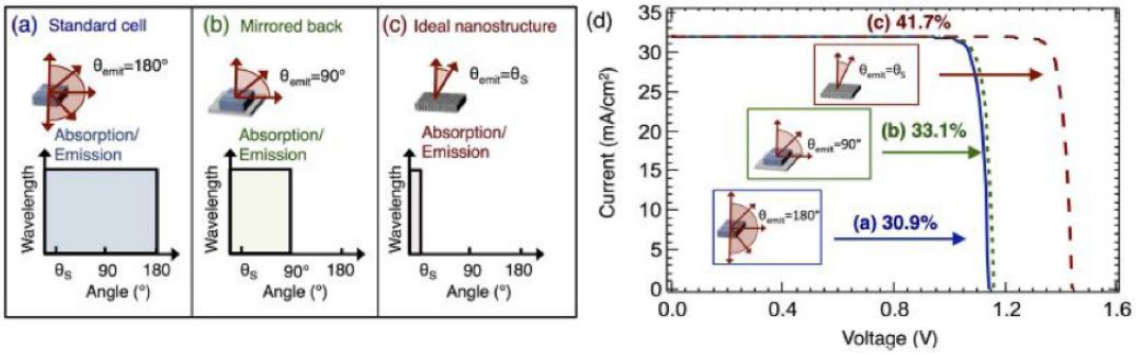

Figure 1.12: The effect of absorption and emission angle on V_{OC} for three different cases of (a) A conventional bulk solar cell without back mirror. The emission half-angle for this case is 2π because of the lack of reflection at back surface (b) A conventional bulk solar cell with a back mirror configuration. The emission half-angle in this case equals π which can result in an increas in V_{OC}. (c) The ratio between emission angle and absorption angle will be approximately equal to unity. (d) The I-V curves for three cases of (a-c). These curves show efficiency improvement by means of reduced emission to absorption angle [75].

is exactly equal to the case of a bulk SC with concentration optics [82]. Additionally, we can rewrite Euaiton 1.16 for the described nano-cell as a function of its absorption cross-section assuming that minimum cross-section is bounded to the geometrical top surface of the cell leading to $X = \sigma_{max}/\sigma_{geo}$, then,

$$V_{oc} = \frac{k_B T_c}{q} ln[\frac{\sigma_{max}}{\sigma_{min}}(\frac{I_{L,0}}{I_{R,0}})] \tag{1.21}$$

Based on various studies on nanostructured SCs, the concentration factor is commonly in the range of 1 to 10, therefore, efficiency of a nanostructured SC can be increased due to its V_{OC} [75]. In general, the efficiency of PV cells has direct relation to the V_{OC} and inverse relation to the input power [78]. As a result, the same advantage of nanostructured SC can be formulated into the efficiency calculation using Equation 1.8. As it was explained, the emission and absorption solid angles can affect the open circuit voltage with the term $kTln(\Omega_{emit}=\Omega_{sun})$. The effect of this factor is depicted in Figure 1.12. In conventional solar cells, without a back mirror configuration, the difference between the absorption and emission angle is large with $\Omega_{emit} = 4\pi$. But the ratio of these unmatched solid angles decreases in solar

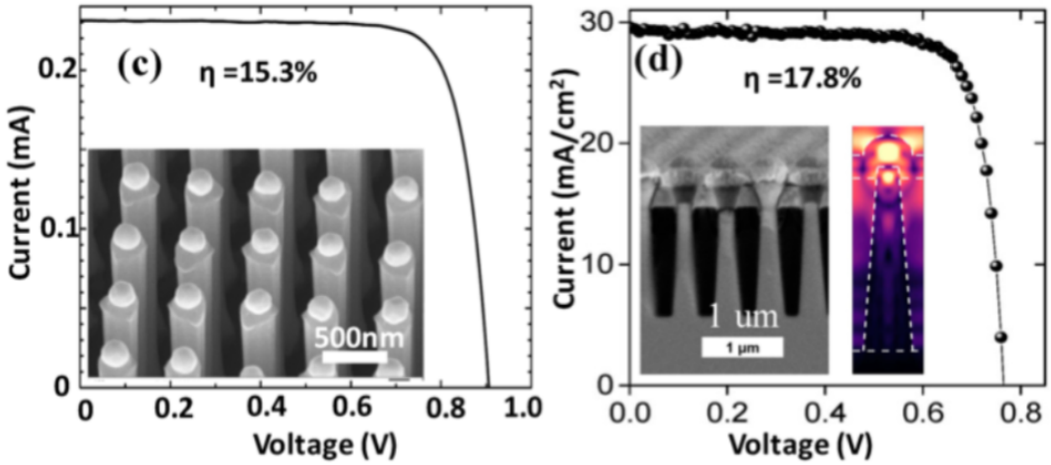

Figure 1.13: Reported I-V characteristics of (a) GaAs NW arrays SC [83], and (b) InP NW arrays SCs [84] for 1 sun AM1.5G illuminaiton.

cells with back mirror, which reduced the emission angle to 2π. Nanostructured SCs, on the other hand, minimizes this entropy-related factor by reducing the emission angle such that it becomes so close to the absorption angle that their ratio will be approximately equal to unity. This, in fact, is the origin of an elevated open-circuit voltage in nanostructured photovoltaic cells.

1.4.5 State of the Art Nanowire-based Solar Cells

To date, the world record for SCs based on vertical NWs with highest efficiency belongs to Hwang et al. with 18.9% for flexible cells based on vertically aligned Si microwires realized by deep reactive ion etching (DRIE) on 50 μm c-Si substrate [85]. The next best reported NW-based SC is realized by a top-down approach, where n- and p-doped InP layers were epitaxially grown on an InP substrate followed by deposition and patterning of a silicon nitride (SiN) template layer for dry etch of InP epilayers into vertically aligned InP NWs. In this study, Dam et al. reported cell efficiency of 17.8% [84].

In addition, studies from Åberg et al. on GaAs NWs array with 15.3% [83] and Wallentin et al. on InP NWs array with 13.8% [33] demonstrated highest efficiencies

for SCs based on epitaxially grown III-V NWs, which are the focus of this dissertation. It is worth noting here that both cells were grown on their native III-V substrates via Au-seeded VLS approach in a MOCVD reactor, with axial doping profile. To date, published reports on NWs with radial junction geometry have not exceeded 7.5% [86–92]. The main challenges in fabricaiton of SCs based on core-shell NW arrays will be discussed in length in Chapter 5.

1.5 Organization of Dissertation

The objective of this dissertation is to demonstrate epitaxy of III-V NWs on foreign substrates via two different catalyst-free growth mechanisms for photovoltaic applicaitons. This document is organized into seven chapters.

Chapter 1 introduces motivation and background for photovoltaic solar cell devices based on III-V semiconductor nanowires. This includes motivation for harvesting solar energy as a clean energy-conversion solution. This chapter reviews theoretical background information of solar cell device operation and nanowire based solar cell devices.

Chapter 2 details information related to experimentals methodologies used in this study. This includes various material characterizations methods utilized to evaluate nanowires morphology and composition, such as scanning electron microscopy and X-ray diffraction spectroscopy.

Chapter 3 focuses on exploring the growth parameter space for self-assembly of InAs, $InAs_yP_{1-y}$ and $In_xAl_{1-x}As$ NWs arrays on graphene via van der Waals epitaxy. In this chapter, change in NWs diameter, length and number density are studied as a function of growth parameters.

Chapter 4 reports the first demonstration of selective-area van der Waals epitaxy of vertically aligned III-V nanowires on 2D molybdenum disulfide (MoS_2) micro-plates.

Chapter 5 presents selective-area epitaxy of GaAsP nanowire arrays on silicon

for tandem junction photovoltaic solar cells. In this chapter, integration of nanowire arrays via three different patterning methods and composition study of $GaAs_yP_{1-y}$ nanowires are reported.

Chapter 6 summarizes the conclusions made from the presented research projects in Chapter 3 through 5.

Chapter 7 provides future works towards fabrication of a III-V-on-Si tandem solar cell.

Chapter 8 presents a list of research products including peer-reviewed publications.

Chapter 2

Methodology

2.1 Metal Organic Chemical Vapor Deposition

To date, metal organic chemical vapor deposition (MOCVD), offering high throughput III-V epitaxy, has become one of the major epitaxial growth techniques in industry. In MOCVD, precursors in gas phase flow over the hot growth surface where pyrolyis takes place and the growth species deposit on the substrate. Other techniques such as liquid-phase epitaxy (LPE), chloride vapor-phase epitaxy (CIVPE), and molecular beam epitaxy (MBE) are used for growth of semiconductor crystals of semiconductor materials. The superiority of an epitaxy growth technique is defined by its capability in realizing uniform structures with abrupt interfaces, high growth rate, ability to grow a variety of different alloys, in situ monitoring, and scalability for industrial production [93].

In academic material research labs, MBE has been the standard technique for epitaxy of semiconductor alloys. Through MBE, heteroepitaxy of highly pure structures with atomically abrupt hetero-interfaces is achievable. The main challenge with MBE is in scalability for industrial manufacturing. Since MBE operates under ultra-high vacuum (UHV), this lower base pressure often time needs to be broken for refill of the source or performing maintenance. This leads to high cost of downtimes.

In contrast, MOCVD standard operating pressure is on the order of 75 torr (100 mbar), and precursors are maintained in separate cabinets using bubblers or pressurized

gas reservoirs. The main limitations of MOCVD stems from the cost and challenges in using and storing of hazardous precursors. Metal organic sources are expensive, as they are very reactive and therefore difficult to purify. Precursors with low oxygen content are essential for epitaxy of highly efficient semiconductor base devices. It is shown that photoluminescence intensity of AlGaAs structure was increased by a factor of 3-10 by upgrading the quality of trimethylaluminum (TMAl) precursors, with lower oxygen content [94]. In addition, metal organic precursors are volatile liquids and hence involve precise pressure controller systems.

In this work, all epitaxial growths experiments were done using an Aixtron 3×2" close coupled showerhead (CCS) MOCVD reactor similar to the one shown in Figure 2.1. The fundamentals of MOCVD operation are discussed in this section. The reactor is situated inside a nitrogen glovebox. This arrangement allows isolation of dangerous precursors and their byproducts from the operator, as well as a protection for the reactor itself from oxygen, water and other source of contaminations. A carrier gas, hydrogen (H_2) or nitrogen (N_2), delivers metal organic (MO) and hydrides (Hyd) precursors into the reactor through MO and Hyd lines (Figure 2.2).

Figure 2.1: An Aixtron 3×2" CCS MOCVD reactor

There are various configurations of MOCVD reactors based on both lateral and vertical gas flow. In the specific case of Aixtron 3×2" CCS MOCVD design, the reactants enter the reactor from a quartz shower head, containing nearly 100 millimeter-sized inlets, sitting 2" above the susceptor. The susceptor is a rotating disc, which is heated to the growth temperature by a resistance heater. Growth temperature is usually in the range of 500-1000°C. The temperature profile of the susceptor surface, and therefore the growth substrates, can be controlled by separate heating zones. This allows a uniform and constant temperature profile on the entire surface of the susceptor. In contrast the high temperature susceptor, the shower head and the reactor wall are water-cooled ∼55°C. This leads to a large temperature gradient inside the chamber. The desired combination of MO, Hyd and carrier gases flow down the shower head toward the growth surface. The reactants then undergo pyrolyis on the heated growth surface and, based on the selected reactor parameters, the desired growth mode can takes place. can take place. The remainder of the growth species that do not adsorb on the growth surface or the reactor walls are vented out through the exhaust line.

As for precursors for growth of III-V semiconductor compounds, organic group-V element hydrides such as arsine (AsH_3) and phosphine (PH_3) are used. Except for Sb

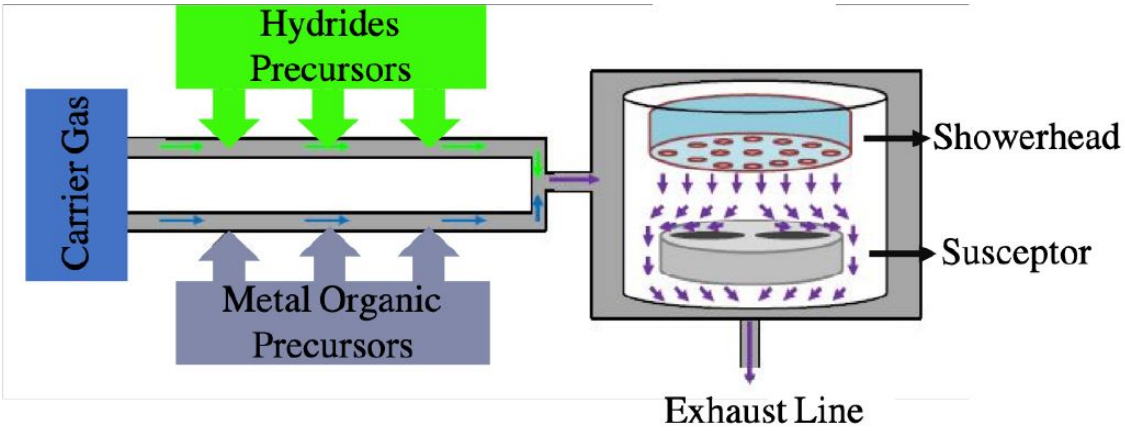

Figure 2.2: Schematic diagram of gas delivery system in MOCVD reactor. Carrier gas supply, Hyd and MO lines, shower head, susceptor and the exhaust line is depitcted.

which is common to be in form of trimethylantimony, other group V and Si precursors are hydrides and are kept in pressurized bottles at room temperature. Regarding metal organic precursors, trimethyl and triethyl alkyls, such as trimethylindium (TMIn) and triethylgallium (TEGa), are the two most common sources. The trimethyl compounds are preferred due to their superior stability and higher vapor pressure. These precursors are in liquid phase and are stored at temperatures around 4-22°C in bubbler vessels, where the liquid and vapor phases are in equilibrium. Through the gas delivery system and mass flow controllers (MFCs), the carrier gas is injected in the bubbler in a controllable fashion, resulting in a desired mixture of carrier gas and precursor in vapor phase. The vapor pressure of the precursor in a bubbler is always kept constant. This can be achieved by submerging the bubbler in a bath of water that is held at a constant and stable temperature. In some cases, the growth conditions are conducive for group V, III or both to have flowrates below the reliable range of MFCs. In these cases, a double dilution system can be used. In double dilution arrangement, mixture of carrier gas and precursors leaving the bubbler are diluted with carrier gas in a separate line before injecting into the MO or Hyd lines. In the reactor, the delivered precursors undergo pyrolyis and are cracked to group-III and group-V constituents. These reactants interact on the growth surface and form III-V compounds. For example, in case of a binary semiconductor compound of AB, the chemical reaction equation can be written as follow

$$R_{\mathrm{n}}A + BH_{\mathrm{n}} \rightarrow AB + nRH \tag{2.1}$$

$$R_{\mathrm{n}}A + R'_{\mathrm{n}}B \rightarrow AB + nRH + nR'H \tag{2.2}$$

Where R and R' stands for unspecified organic radicals.

2.2 Nanowire Growth Mechanisms

2.2.1 Vapor-Liquid-Solid Epitaxy

In VLS, catalyst particles are placed on the substrate. Next, the substrate is heated to a substantially high temperature for removing the native oxide. To prevent substrate degradation, a flow of group-V precursors is supplied to the chamber. Next, the temperature is set to the NW growth temperature, and flow of group-III precursors is initiated. Growth species form a liquid-phase alloy with the particle, either by diffusing on the substrate surface or by direct impingement on the particle. This process continues to the point that the catalyst particle reaches a supersaturation state, and solid-phase nucleation takes place at the interface of the liquid alloy and the underlying substrate. A continuous supply of vapor-phase precursors guarantees a steady-state regime, and the nucleation process is continued under the catalyst. Therefore, with formation of each atomic layer, the catalyst particle is lifted further from the substrate and NW growth is maintained.

2.2.2 Selective Area Epitaxy

Selective area epitaxy (SAE) is an important crystal growth technique for applications across electronic, optoelectronic, and photovoltaic device fabrications. SAE is a templated epitaxy technique, meaning a patterned film is used to limit the crystal growth to the exposed substrate surface. It has been shown that high quality III-V compound films can be achieved using MOCVD. This allows for high degree of control on the thickness, composition, and doping. Achieving selectivity is straightforward for growth techniques,such as liquid phase epitaxy, where the crystal growth takes place close to the equilibrium. For MOCVD process, however, the crystal growth takes place far from the equilibrium. In this case, to realize selectivity the growth condition should have certain criteria, e. g. lower reactor pressure and elevated growth temperature.

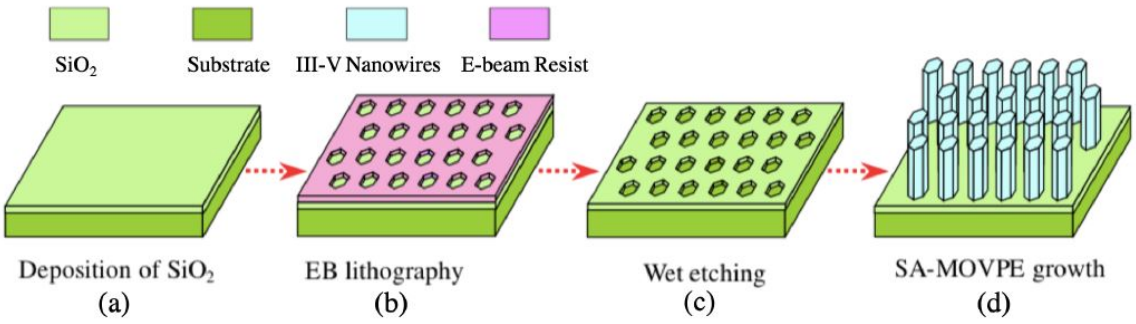

Figure 2.3: The growth template for SAE of III-V NWs is prepared by (a) deposition of SiO_2 film on the substrate, (b) patterning by electron beam lithography, (c) transfering the pattern in the SiO_2 template by wet etch, (d) epitaxy of NWs using MOCVD. Modified from [95].

The right MOCVD conditions allow for three different types of diffusion mechanisms. Firstly, vapor phase diffusion takes place across the gaseous boundary layer in the chamber. Secondly, precursors impinging on the masked regions of the sample cannot absorb on the template film and diffuse on the surface toward the exposed substrate surface. Lastly, this spatial selectivity in the absorption and desorption of precursors forms a local gradient in partial pressure of precursors. This is due to excess of gas phase precursors on the masked regions and lower availability of precursors on openings (exposed substrate regions). This allows for a third diffusion mechanism which is in form of a lateral vapor phase diffusion. As a result of these diffusion mechanisms, the crystal growth enhances in the pattern openings. For the specific case of NWs growth, a right selection of growth conditions can result in an enhanced vertical growth rate to the point that high aspect ratio NWs can be achieved via SAE. The most common choice of substrate orientation for SAE of NWs is a (111) substrate. This results in 110 sidewall facets and high axial growth rate in (111) direction.

The sample preparation for SAE of NWs is illustrated in Figure 2.3. In this process, first an amorphous mask is used to cover the substrate. Common materials used as mask are silicon oxides (SiO_x) or silicon nitrides (SiN_x). These films have high durability at an elevated temperature that is typical for SAE via MOCVD or

MBE. In the current research, SiO_x is deposited with plasma-enhanced chemical vapor deposition (PECVD). Next, desired patterns are defined in the mask through different lithography methods, such as electron beam lithography (EBL) and photolithography. While compared to conventional photolithography, much smaller features can be defined by EBL, this technique is more expensive and time-consuming, especially for samples with a large surface area. Dry or wet etch techniques can be used to transfer the pattern to the SiO_x film. It should be noted that as crystal growth takes place on Si surface only, it is a common practice to add a step to remove the Si native oxide. This is usually done by a buffered oxide etch (BOE) before loading the sample into the MOCVD glovebox.

2.3 Electron Microscopy

2.3.1 Introduction

Electron microscopy is one of the most important characterization techniques for understanding of nanomaterials beyond the spatial resolutions of optical microscopes. The minimum resolution limit of an optical microscope can be calculated by

$$(\Delta l)_{\min} = \frac{0.61\lambda}{n \sin \beta} \tag{2.3}$$

where n is reflection index of the viewing medium, β is the semi-collection angle of the lens, and λ is the wavelength of the incident light. In the specific case of visible light, the resolution limit of optical microscopy is on the order of hundreds of nanometers. In electron microscopy, however, highly accelerated electrons are used to achieve tunable resolutions to several orders of magnitude lower that optically achievable. To gain a better understanding of current electron microscopes range of resolution, one can use the equation 2.4 to calculate the electron wavelength as a function of the acceleration voltage:

$$\lambda = \frac{h}{\sqrt{2m_0 qV(1 + \frac{qV}{2m_0 C^2})}} \tag{2.4}$$

where m_0 is the electron rest mass, q is fundamental electron charge, V is the potential difference delivered for electron acceleration and c is the speed of light. For a transmission electron microscope (TEM) with acceleratio voltage of 200 kV, the electrons wavelength is calculated as approximately 2.5 pm. However, the practical resolution of an electron microscope is typically lower than pico-meteres. This is because after electrons are generated, an anode cylinder is used to accelerate the electrons through a series of magnetic lenses which are used to control focussing and magnification. The abberrations introduced by these magnetic lenses limits the image

resolution on the order of angstroms.

2.3.2 Electron Beam/Sample Interactions

When an electron beam interacts with a specimen, various types of signals are generated, as depicted in the Figure 2.4. If the electrons transmit through the specimen without any interaction, they are denoted as direct beam or unscattered electrons. Whereas, if the electrons interact with the sample atoms without any energy loss, they are referred to elastically scattered electrons. In case of energy loss, electrons are inelastically scattered. In particular, backscattered and secondary electrons are

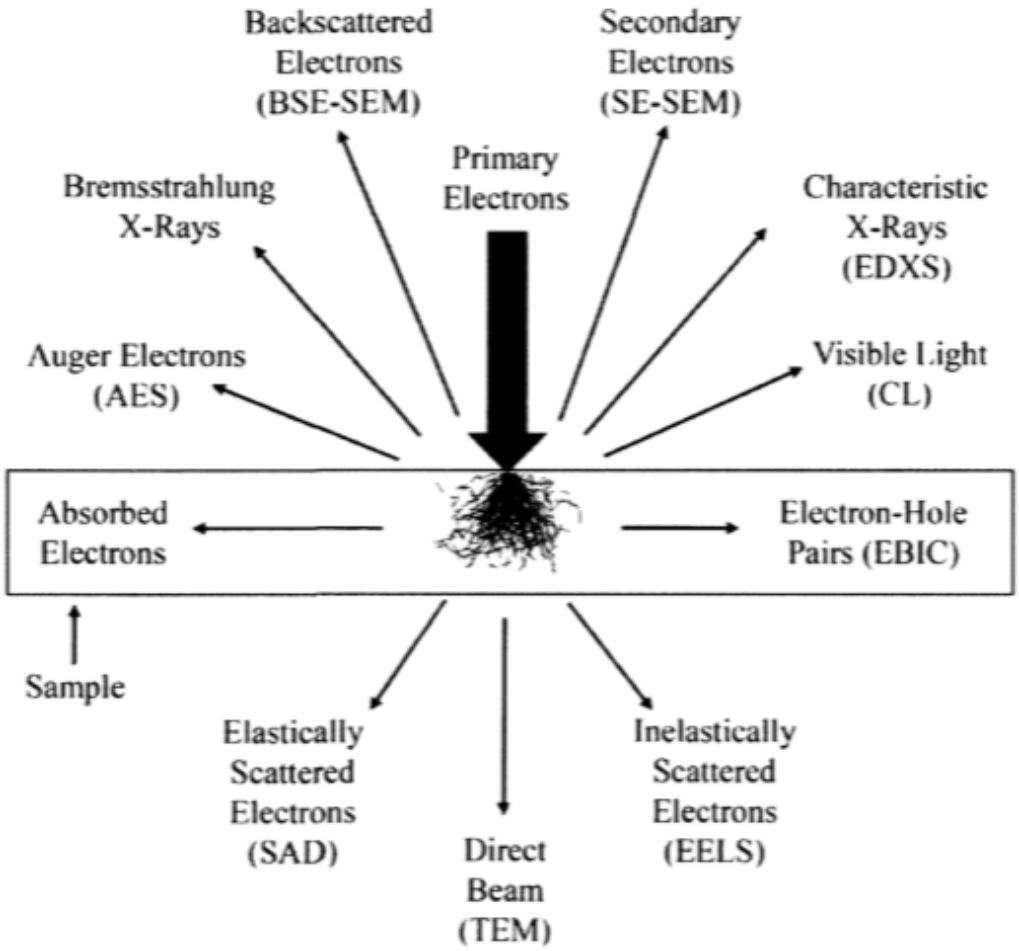

Figure 2.4: The various signals originated from interaction of a high energy electron beam with a thin sample.

used in scanning electron microscopy (SEM), which will be explained in the next section. The characteristic X-rays signals originate from the change in energy level of an electron moving from a higher to a lower energy level. The characteristic X-rays can be used for composition analysis since the differences in energy states are specific to each element in the periodic table. Instead of generating an X-ray, an electron relaxing from a higher to a lower level can give the release energy to another electron and make it escape the sample. The escaped electron is called Auger electron (AE). Finally, Bremsstrahlung X-ray originates from electrons interaction with the Coulumb fields of the atomic nuclei.

2.3.3 Scanning Electron Microscopy

For the presented research in this work, SEM is used to characterize the morphology of III-V nanostructures. Two SEM systems, the Hitachi S-4000 and Tescan MIRA3 instruments, are used for sample imaging. A simplified schematic of SEM is shown in Figure 2.5. Typically in SEM systems, the electron gun filament is kept at a large negative potential with respect to a grounded anode plate. Thus, an electron beam, consisting of primary electrons (PEs) is accelerated toward the sample surface and penetrates the sample in a pear-shaped region called the interaction volume (Figure 2.6).

To control the beam spot size, before electrons pass the objective lens and reach the sample, the electron beam is shaped by a series of condenser lenses. Using scanning coils, the beam can be deflected and scanned along various X-Y coordinates on the sample surface. Detected signals from each point are then registered by a computer system. These signals are generate through elastic or inelastic scattering processes from the interaction of PEs with sample atoms within the interaction volume. Backscattered electrons (BSEs) are electrons that undergo elastic scattering interactions with the atomic nuclei in a given sample, and can escape the sample through Rutherford

backscattering. The ratio of BSEs to PEs, called backscattering coefficient, gives information about atomic number (Z) of the sample. Albeit, the higher energy of these electrons (close to PEs energy), and therefore larger interaction volume, reduces the resolution in the BSE imaging mode. Secondary electrons (SEs), generate from an inelastic interaction, are lower in energy (10-50 eV) and have an escape depth of around 10 nm. Compared to BSEs, SEs are more abundant and they are generated from all locations in the interaction volume, but they only escape from areas closer to the surface. Hence SEs carry information about the surface structure and topology.

For all experiments presented in this dissertation, all SEM images are generated using SEs. The relative angle of sample and PEs can be set to different values, which leads to different SE yield and shows various views of the sample. By tilting the sample toward the detector, greater SE yield can be achieved. Except for top-view

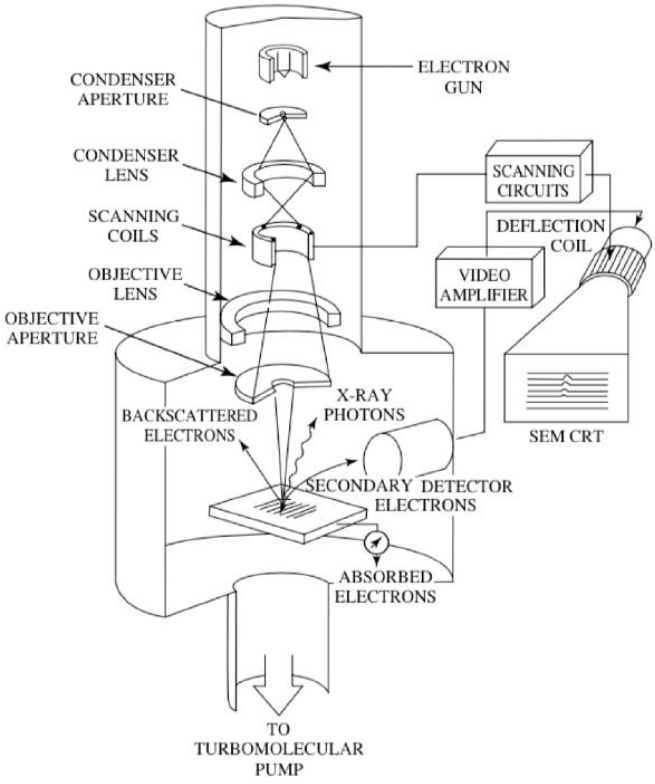

Figure 2.5: Schematic of a SEM system illustrating different parts of a typical SEM system [96].

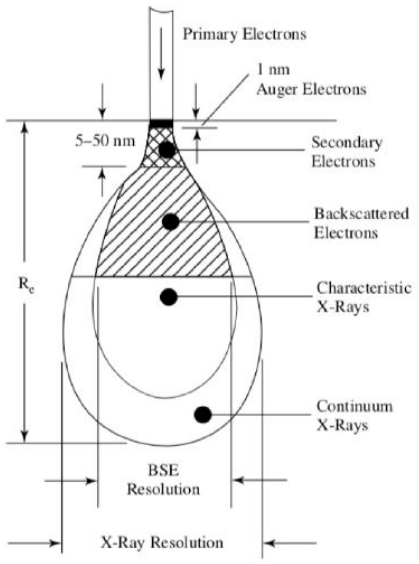

Figure 2.6: The interaction volume of primary electron beam with sample [96].

images, all images presented in this work are collected at a stage tilt angle of 45°. Planar and tilted-view SEM images mainly provide information about NW morphology, length and diameter, orientation and areal density. Lastly, samples were mounted on an aluminum based mounting stub with double sided copper tape. This allows a conductive pathway for electrons and minimize accumulation of static charges in a sample. For samples with less conductive characteristics, liquid silver paste was used to draw a path from sample to the stub.

2.3.4 Focused Ion Beam

The focused ion beam (FIB) microscope is similar to SEM in basics of operation. Unlike SEM, SEs are generated by an ion beam instead of an electron beam. These SEs can be used for high spatial resolution imaging. There are FIB systems with both electron and ion beam sources. In most FIB systems, the ion source type is a liquid metal ion source (LMIS) with advantages of high degree of brightness and focused beam. Ga-based LMIS is preferred among different types of LMIS such as In, Bi, Sn, and Au. This is due to low melting point (30°C), low volatility, and

low vapor pressureof Ga. These characteristics makes Ga LMIS to be prepared at low temperature and flow from a reservoir to a tungsten (W) needle. While liquid Ga wets the tapered shape tip of the needle, a large electric field on the order of 1010 V/m forms a single Taylor cone (a point source) of Ga. For typical emission current of around 2 μA, this process results in an ion beam with diameter around 5 nm. In addition to imaging, FIB enables site-specific sputtering and deposition. For deposition, a gas-phase metal organic precursor is injected and delivered in vicinity of samples by a nozzle. By rastering an ion beam or an electron beam on a specific user defined location, desired deposition takes place. Many materials are available for deposition such as W, Pt, and C. A simple schematic of a FIB system is shown in [97].

In the presented research, the Strata 400 Dual Beam FIB system was used to prepare site-specific lamella from as-grown samples for TEM analysis. Figure 2.8 shows steps toward preparation of a TEM lamella. In this sample preparation technique, before loading the sample in FIB chamber, ∼10 nm carbon as a protective layer is deposited on the sample via a standard sputter coater tool. Once the sample is loaded and the desired region is located, the sample is covered with two additional protective layers via (1) electron beam induced deposition (EBID), and (2) ion beam induced deposition (IBID). The reason behind this selection is that IBID has high deposition

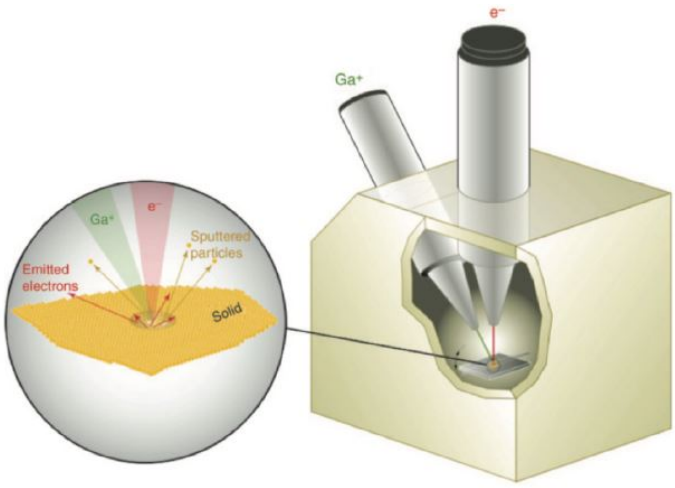

Figure 2.7: A simple illustration of FIB tool [97].

rate but can cause surface damage and undesired sputtering on the features, whereas the EBID-layer can protect the nanostructure surface and reduce the risk of the surface damage during IBID.

The next step is to place markers at strategically important locations. The suggested locations are: (1) at the two ends of a desired foil. For ease of actions for future steps, it is important to measure the distance between markers and the desired nanostructures at this step, and (2) at regions adjacent to the nanostructures of interest. These mark features can be produced by milling a diamond shape and filling it with Pt deposition. At this point the region of interest should be covered by

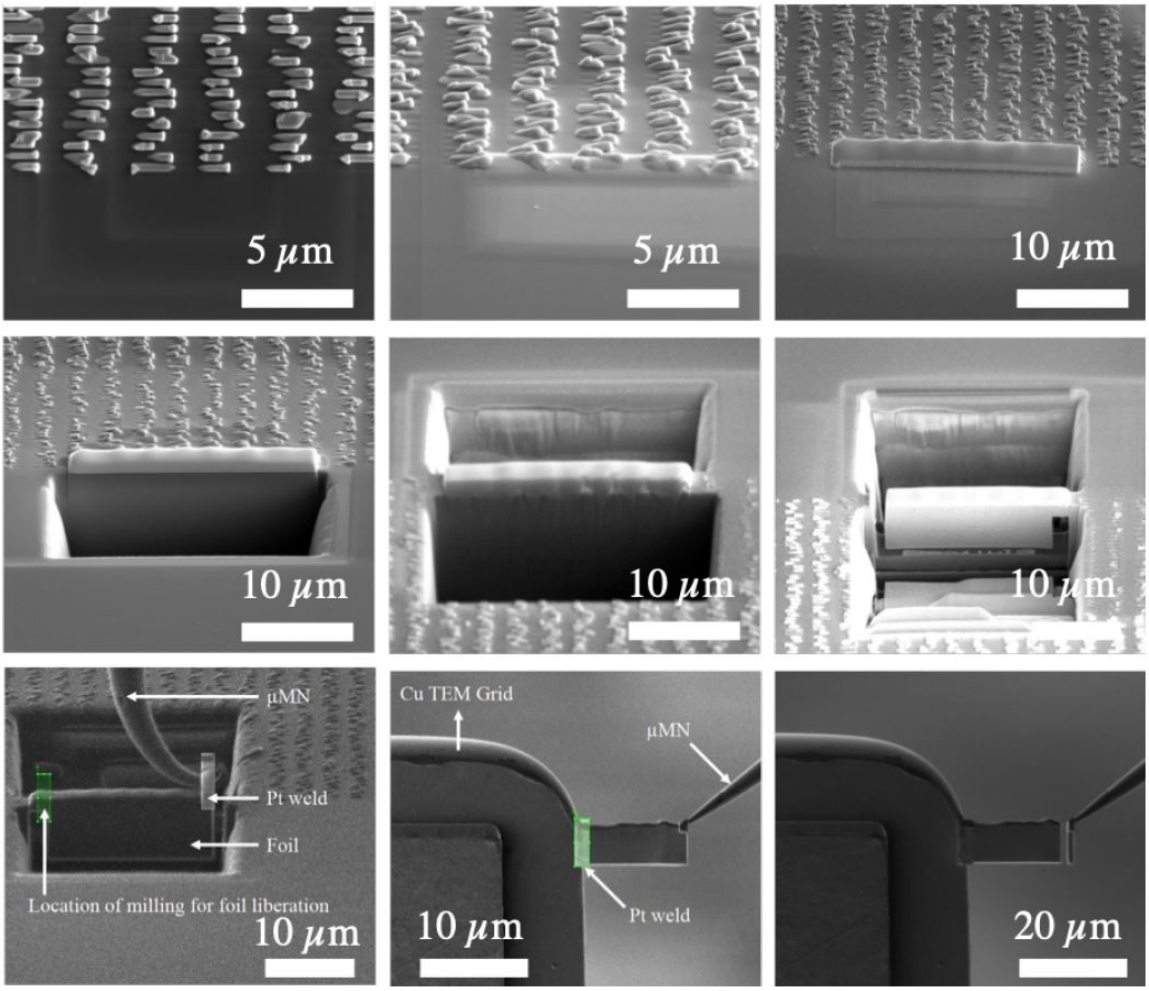

Figure 2.8: TEM lamella preparation steps using FIB. Perfomed at CCMR facilty, using the Strata 400 Dual Beam FIB system.

a final protective layer via IBID Pt deposition. This defines the area of a foil that contains the region of interest. Next, it is necessary to separate this foil from the bulk sample by milling two trenches and form a J-shaped milled feature below the substrate surface along the region of interest. A micro needle is inserted in the FIB chamber to carry the foil from sample location to a TEM grid location. By welding one side of the foil to the tip of the needle, the opposite side of the grid can be released. The last step is to align and weld the foil to a TEM grid and separate the needle from the foil, followed by ion milling to thin the foil such that it is electron-transparent.

2.3.5 Transmission Electron Microscopy

Transmission electron microscopy (TEM) technique is based on the interaction of an atomically-thin specimen (< 250 nm) and electrons with high acceleration energy of larger than 100 keV. Due to the high acceleration voltage of the electron beam and the sufficiently thin sample, the primary electron (PE) can transmit through the sample. There are two main mechanisms for formation of contrast, mass-thickness contrast and diffraction contrast.

In a TEM image, the variation in intensity can be linked to the mass or thickness of a specific region within the specimen. Meaning, thicker parts of the sample show lower penetration depth and absorb more PEs, and segments with higher-Z elements cause elastic scattering events with larger angles relative to the optical axis. In both cases, these electrons can not be detected which lead to corresponding regions with dark contrast on the TEM image. This type of imaging is known as bright-field imaging, where only the direct PEs are detected, while diffracted or scattered electrons at higher angles are filtered out by an aperture. In this dissertation, bright-field imaging is used for qualitative study of the morphology and variation in elemental composition of nanowires.

Furthermore, in high-resolution TEM (HR-TEM), the information about the phase

contrast can be collected. In this scenario, a wide objective aperture is inserted such that both diffracted and transmitted beams with different amplitudes and phases can be collected. This way, a Fourier sum of these signals leads to a very precise and highly detailed image. Using this technique, lattice resolved imaging of NWs is achieved in this study. Throughout this work, two different methods for sample preparation are used. First sample preparation technique is FIB, which is described in Section 2.3.4. FIB is beneficial for thinning the samples and make them electron transparent, especially when the heterointerface of NW and substrate is the region of interest. Another way to prepare a TEM grid is to break off the NWs using a controlled mechanical agitation. In this method, NWs can be removed from the substrate by submerging the sample in a small volume of a solvent (e.g. 2 mL of methanol) and use of ultra-sonication bath to apply agitation. Next, the solution containing suspended NWs can be dispersed using a micro-pipet on a standard carbon holey copper TEM grid.

2.3.6 Scanning Transmission Electron Microscopy

The scanning transmission electron microscopy (STEM) uses scan coils for raster scanning of an electron probe. This permits for registering the detection of transmitted or diffracted electrons in reference to the scanning address of the incident beam. In STEM mode, annular dark field (ADF) or high angle annular dark field (HAADF) images can be obtained. Electrons scattered with a certain angles can contribute to acquiring of these type of images. In ADF imaging mode, only electrons scattered within 10-50 mrad can contribute to imaging. Whereas for HAADF, electrons scattered at an angle larger than 50 mrad can be detected. In this way, the image is mainly formed by Z-contrast. Therefore, more electrons that are scattered from higher-Z sample regions can be detected by ADF or HAADF detectors.

2.4 X-Ray Diffraction

X-ray diffraction (XRD) is a technique to investigate the quality, composition and strain in crystal structures. In this research, high resolution XRD characterization was used to study the composition of InAsP NWs arrays on graphene. This characterization was done using a Bruker D8 system with Cu Kα X-ray source. In XRD, an X-ray beam incident on the surface of the sample at a specific angle (θ) reflects from the individual crystalline planes of atoms. Here, we neglect the inelastic scattering meaning the energy of reflected beam is equal to energy of the incident beam. Diffraction takes place for beams reflected from crystal planes that interfere constructively. For a material with interplanar spacing of d, this happens when the Bragg condition is satisfied, meaning the path length difference (2dsinθ) should be equal to an integer multiple of the X-ray wavelengths (nλ), as shown in Equation 2.5.

$$2d \times sin(\theta) = n\lambda \tag{2.5}$$

In the XRD set up illustrated in Figure 2.9, the tilting stage sweeps the angle θ to

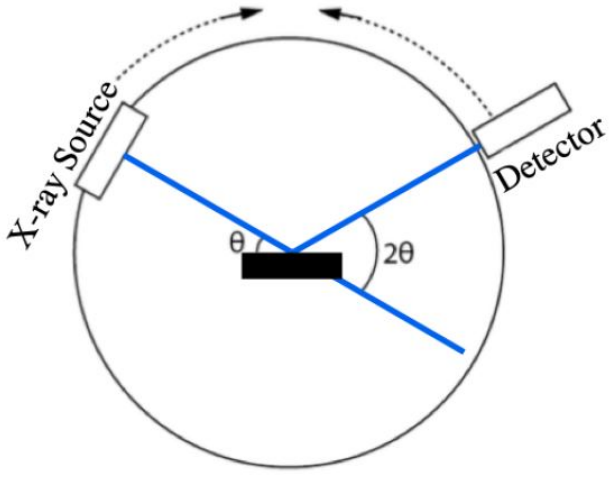

Figure 2.9: A simple diagram of a XRD set up showing an X-ray source hitting the sample at Bragg angle, the detector collects the reflected beam at the same angle.

satisfy the Bragg condition. In this way, the beam coming from the X-ray tube hits the sample at θ angle, and the detector collects the beam at the same angle.

Chapter 3

Pseudo-van der Waals Epitaxy of III-V Nanowire Arrays on 2D Nanosheets

Project Title: Improving pseudo-van der Waals epitaxy of self-assembled InAs nanowires on graphene via MOCVD parameter space mapping

Citation: M. A. Baboli, M. A. Slocum, H. Kum, T. S. Wilhelm, S. J. Polly, S. M. Hubbard, and P. K. Mohseni, CrystEngComm, vol. 21, no. 4, pp. 602–15, 2019.

3.1 Introduction

In recent years, the integration of III-V NWs with inert graphitic surfaces and functional two-dimensional (2-D) graphene nanosheets has been explored [99], [100–109]. Monolayer nanomaterials including single layer graphene (SLG), hexagonal boron nitride (h-BN), and transition metal dichalcogenides such as molybdenum

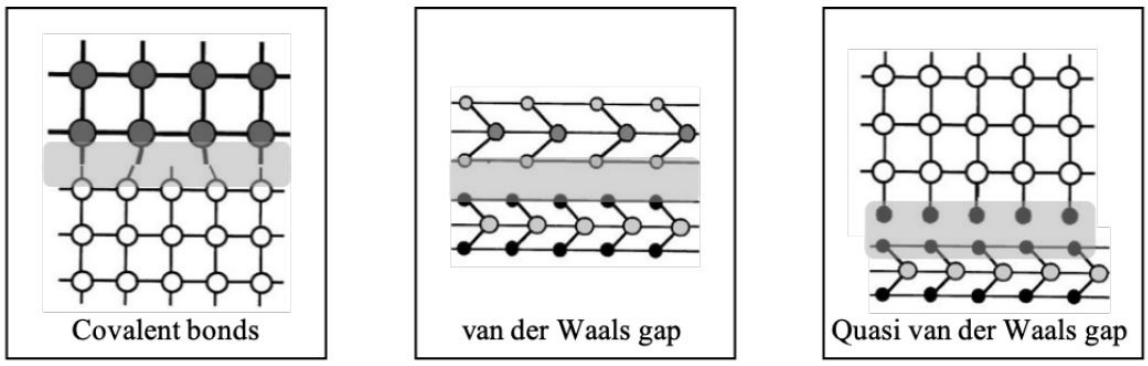

Figure 3.1: A schematic comparing different forms of epitaxy techniques. In the conventional epitaxy, the two layers share covalent bonds at their interface vs. in the vdW and quasi-vdW epitaxy the 2D layer surface provides no dangling bonds for covalent strain sharing [98].

disulfide (MoS_2) and tungsten diselenide (WSe_2) have shown promising performance in electronics [110], optoelectronics [111], photovoltaics [112], [113], and photonics [114] applications. Through integration of III-V semiconductor NWs with 2-D nanomaterials, the unique properties of both nanostructure groups can be simultaneously exploited in the form of nano-hybrid materials system [99], [100, 101]. Additionally, transfer and re-distribution of interfacial charge states in such integrated nanomaterials can enable unique optical and electronic properties that are distinct from those of the constituent materials [115, 116]. Integration of this kind may be realized through the pseudo-van der Waals epitaxy (vdWE) approach, whereby an epi-layer is formed on an inert 2-D surface that provides no surface dangling bonds for covalent strain sharing [98] (Figure 3.1). Weak vdW forces between a monolayer substrate and III-V epilayer can accommodate nucleation and subsequent growth such that interfacial lattice distortion is mitigated and dislocation-free crystal assembly can take place.

Unlike semiconductor substrates with reactive dangling bonds, the growth surface of 2-D nanosheets offers limited positions for adatom adsorption and subsequent extension of the III-V lattice. In the case of graphene, the carbon honeycomb lattice allows three residence sites: (i) above a carbon site (T-site), (ii) above the bridge between a C-C bond (B-site), (iii) above the center of a hexagonal carbon lattice (H-site) [100]. As a result, and based on the lattice constant of a given III-V compound, there are limited possibilities for arrangement of atoms at the growth interface. Munshi et al. summarized possible atomic arrangement for binary III-V compounds with different lattice constants [100]. From a thermodynamic perspective, not all of these possible arrangements are achievable. This is due to the difference in binding energy between carbon atoms in the honeycomb lattice and atomic growth species that reside on T-, B-, or H-sites [117]. It has been shown that In adatoms may reside on energetically favorable H sites with bond energy of 1.29 eV [118]. This allows InAs to adopt its native lattice constant on SLG [119].

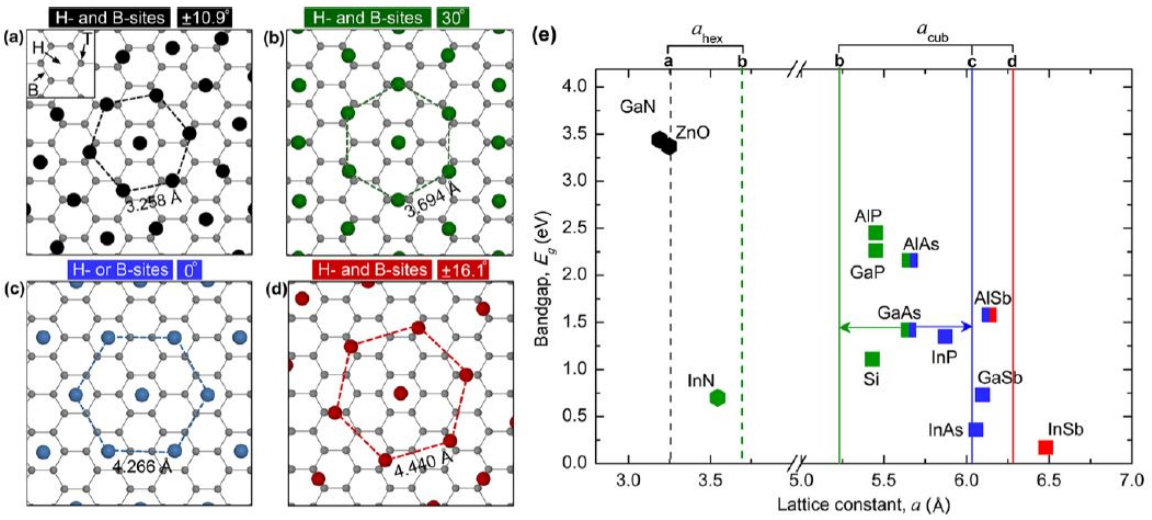

Figure 3.2: Different orientations of III-V compounds lattice on graphene surface [100].

The simplicity of the MOCVD-based InAs NW vdWE approach, which requires no pre-growth surface pattering or pre-deposition of catalyst droplets, is highlighted as a key advantage. Nevertheless, precise tuning of growth conditions are needed and realization of optimal growth is non-trivial. The term optimal is used here to define the maximal aspect ratio of individual NWs comprising an array of maximal number density. Additionally, the term optimal is intended to describe a parameter space in which supplied growth species contribute predominantly to the formation of NW structures, such that parasitic growth of polycrystalline nano-islands is minimized. Although several studies on vdWE of InAs NWs on SLG have been presented in the current literature, and optoelectronic and photovoltaic devices have been demonstrated based on this nano-hybrid system [99], [120], extensive evaluation of the growth window has only been carried out for the case of In-seeded NWs by MBE. Systematic mapping of the extended parameter space and a self-consistent correlation of growth conditions to NW morphology, NW number density, and areal coverage of parasitic islands during self-assembly of InAs NWs on SLG is needed for the MOCVD approach.

Here, a comprehensive exploration of the growth parameter space for self-assembly of InAs NWs on SLG by MOCVD vdWE is presented. In particular, the length,

diameter, and number density of NWs, as well as the areal coverage of parasitic island growth is quantified as a function of MOCVD conditions including V/III ratio, growth temperature, and total flow rate of precursors. Growth trends are discussed in terms of underlying kinetic factors. By mapping a wide parameter space, growth conditions are simultaneously tuned for the formation of arrays with maximum NW aspect ratio, maximum NW number density, and minimum areal coverage of parasitic three-dimensional (3-D) nano-islands. The crystal structure of NWs grown under largely disparate conditions is analyzed to reveal a characteristically invariant polytypic NW lattice that is formed throughout the entire growth window. The evolution of NW morphologies over time is described with respect to axial and radial growth rates. The influence of a pre-growth arsine surface treatment is studied as an additional operational control that permits manipulation of NW densities. Finally, a two-step flow-modulated growth procedure is introduced for further optimization of NW aspect ratio and number density. Having a complete understanding of the MOCVD parameter space for seed-free and pattern-free growth of InAs NWs on SLG can be extended toward: (a) self-assembly of In-based ternary semiconductor compound NW structures such as $InAs_yP_{1-y}$ and $In_xAl_{1-x}As$ on 2-D surfaces [121], and (b) development of more accurate theoretical models for pseudo-vdWE based on verified experimental growth conditions. Such tuning of InAs NW growth conditions on 2-D nanomaterials is expected to inform the vdWE of a wide-ranging set of III-V semiconductor compounds and impact future device designs with applications in nanoelectronics, optoelectronics, and photovoltaics.

3.2 Self-Assembly of InAs Nanowire Arrays on Graphene

3.2.1 Experimental Details

Continuous CVD-grown monolayer graphene films transferred to 90 nm SiO_2-coated Si (100) substrates were commercially obtained from Graphene Supermarket Inc. and used as the growth surface in all vdWE experiments. The quality of as received graphene nanosheets was inspected by scanning electron microscopy (SEM), performed using a Hitachi S-4000 instrument. Low defect densities and monolayer thickness was confirmed via Raman spectroscopy using a multi-wavelength Jobin Yvon Horiba LabRAM HR Raman microscope. No graphene surface treatment or oxidation steps were carried out prior to loading in the MOCVD reactor, with the exception of a degreasing with a standard solvents. Growth of NWs was performed in an Aixtron 3×2" close coupled showerhead MOCVD reactor. Trimethyl-indium [TMIn, $(CH_3)_3In$] and arsine (AsH_3) were used as precursors for supply of In and As growth species, respectively. The growth parameter space investigated in the present work consisted of the following ranges: (i) growth temperature (T_G) was varied between 550 °C to 700°C; (ii) V/III ratio was varied between 5 to 250 by changing AsH_3 flow rates at a constant TMIn flow rate; and (iii) TMIn flow rates (χ_{TMIn}) were varied between 8 to 32 μmol/min. During all growths, hydrogen (H_2) was used as the carrier gas with total flow of 7 L/min, and the reactor pressure was kept constant at 100 mbar. Unless otherwise specified, all samples were heated to the desired T_G under a constant AsH_3 flow before initiation of growth, which was marked by the introduction of TMIn flow. For all vdWE parameter space mapping trials, the total growth time (t_G) was kept constant at 300 seconds (shorter t_G values are specified for the growth evolution study), and growth of InAs NWs was terminated by stopping TMIn flow while samples cooled under a constant AsH_3 flow. For comparison, additional trials were also performed wherein samples were cooled after growth termination under no AsH_3 flow.

As-grown NW samples were imaged for morphology and density measurements using a Hitachi S-4000 SEM and a TESCAN MIRA 3 SEM, equipped with energy dispersive x-ray spectrometry (EDXS) capabilities. The crystal structure of NWs grown under various conditions was observed using a FEI F20 high-resolution transmission electron microscopy (HR-TEM) system. Selected-area electron diffraction (SAED) patterns were obtained using the same instrument.

3.2.2 Results and Discussions

The main objective of this study is to investigate the vdWE parameter space and to correlate growth conditions to NW length, diameter, and density trends, as well as to changes in the areal coverage of parasitic islands. For systematic evaluation of growth parameter dependences, a series of growth trials are carried out wherein one of three individual variables (i.e., V/III ratio, T_G, and χ_{TMIn}) are altered in the ranges specified above, while the other two variables are kept constant. In the following discussion, all trends presented for NW length, diameter, and aspect ratio consist of multiple data points, each of which quantifies the mean value measured from a set of 50 NWs per growth condition; error bars represent ± 1 standard deviation from the mean. Values for NW density are measured from plan-view SEM images, and each data point represents the mean value based on 5 different sample locations consisting of >250 NWs; error bars represent the range of values measured at different locations. Values for areal coverage of parasitic islands are also measured from 5 different locations on the same sample based on plan-view SEM images, and each data point represents the mean percentage of total InAs-covered area minus the percentage of total area occupied by NWs; error bars indicate the range of measured values. Island and NW structures are distinguished based on size and contrast variances.

3.2.2.1 Mapping the V/III Ratio Parameter Space

Firstly, V/III ratio dependences are considered for InAs NWs grown at constant T_G = 650°C and χ_{TMIn}) = 16 μmol/min. The V/III ratio is varied between 5 and 250. Since NW growth is carried out here under a high T_G regime in comparison to InAs film growth, near-unity pyrolysis efficiency of TMIn is expected [125] such that metal organic decomposition is not further increased in the presence of AsH_3 [122], and modification of the hydride supply alone will alter the true V/III ratio. Also, due the absence of pre-deposited metallic droplets, variances in local effective V/III ratio stemming from catalyst-mediated hydride decomposition are avoided [127]. Similar to

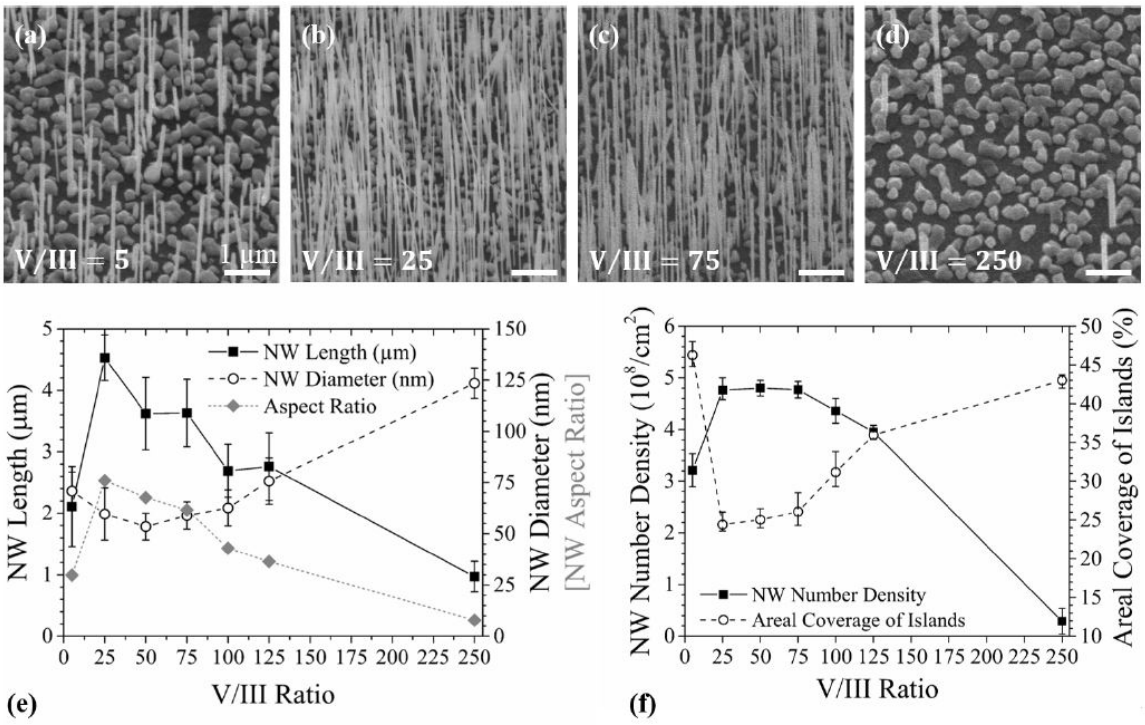

Figure 3.3: V/III ratio dependence: 45° tilted-view SEM images of as-grown InAs NWs on SLG at V/III ratio of (a) 5, (b) 25, (c) 125, and (d) 250, under constant T_G = 650°C and χ_{TMIn} = 16 μmol/min. All scale bars represent 1 μm. (e) Measured values for NW length (black square data points with solid black line), diameter (white circle data point with dashed black line), and aspect ratio (grey diamond data points with dotted grey line), and (f) NW number density (black square data point with solid black line) and areal coverage of polycrystalline islands (white circle data points with dashed black line), plotted as functions of V/III ratio.

the case of InAs NWs grown on Si by chemical beam epitaxy [123, 124], V/III ratios above unity enable catalyst-free NW formation in the current study.

Shown in Figures 3.3(a)–(d) are 45° tilted-view SEM images of as-grown NW arrays at V/III ratio of 5, 25, 125 and 250. Figure 3.3(e) quantifies values for mean NW length (black square data points with solid trend line), mean NW diameter (white circle data points with dashed trend line), and mean NW aspect ratio (gray diamond data points with dotted trend line) as a function of V/III ratio. Consistent with Figure 3.3(a) and (b) SEM images, it is noted that raising V/III ratio from 5 to 25 results in over 2-fold increase in NW length. Below this range, insufficient AsH_3 supply results in sub-optimal NW axial growth rates. At V/III of 25, a maximum NW length of $\sim$4.5 μm is observed within t_G = 300 s. As the V/III ratio is further increased from 25 to 250, a gradual degradation in NW length is observed such that $\sim$1 μm tall NWs are formed at V/III = 250. An opposite trend is found for NW diameter, which is minimized at $\sim$50 nm in the V/III = 25 to 75 range, and increases monotonically beyond this range. Aspect ratio variances with V/III ratio follow the same trend as NW length, marked by a maximum aspect ratio of $\sim$75 found at V/III = 25. In general, moderate V/III ratios in the range of 25 to 75 favor high aspect ratio NW growth.

While similar NW length and aspect ratio trends were observed within a comparable V/III ratio range in the case of In-seeded InAs NWs on graphite by MBE [105], NW diameters follow opposite variation tendencies. In the MBE study, increase in V/III ratio beyond $\sim$50 brought about a nearly 2-fold decrease in NW diameters. This may be a result of catalyst droplet volume reduction via enhanced precipitation of In into the NW lattice under As-rich conditions [125]. In the current MOCVD study, the NW length and diameter trends may be understood simply in terms of surface mobility of In adatoms. Use of higher V/III ratios promotes vapor-solid growth on the NW sidewalls and thereby limits the supply of diffusive species toward the NW top facet

[126]. The result of both effects is the acceleration of radial growth at the expense of axial growth and, thus, the formation of thicker but shorter NWs. The surface migration decay of growth species at elevated V/III ratios also results in reduced NW areal densities and greater coverage of 3-D islands. Figure 3.3(f) quantifies the number density of NWs per area (black square data points with solid trend line) and percentage of total surface area occupied by parasitic 3-D islands (white circle data points with dashed trend line). An inverse relationship between NW density and parasitic island coverage is noted with increasing V/III ratio, which can likely be attributed to a simple conservation of total supply of growth species. At V/III = 5, NW densities of $\sim$3.21 $\times$ 10^8 cm^2 are calculated in comparison to densities of $\sim$4.75 $\times$ 10^8 cm^2 at V/III = 25. Importantly, raising V/III ratio from 5 to 25 is accompanied with a dramatic reduction in areal coverage of islands (from $\sim$46% to $\sim$24%). Further increase in V/III ratio to 75 results in negligible change in NW density and moderate rise in island coverage (to $\sim$26%), followed by a rapid decline in NW density and preferential formation of parasitic growth beyond V/III = 100. Use of V/III ratios above the optimal range of 25 to 75 results in the mitigation of In surface migration such that diffusive growth species are more effectively incorporated into parasitic islands of larger volume. While high V/III ratios favor island formation over NW growth, the lower number density NWs that are formed under such conditions experience enhanced radial growth rates over axial growth rates. Thus, elevated V/III ratio growth conditions are less conducive to fabrication of NW array-based devices, but may be exploited in applications where positioning of widely spaced NWs is required over extended 2-D nanosheet areas. To summarize, an extended V/III ratio space was investigated here (i.e. 5 – 250) and has resulted in growth of NWs with roughly twice the aspect ratio reported previously for seed-free InAs NWs grown on graphene by MOCVD [109], and roughly 7 times greater than the aspect ratio reported for In-seeded InAs NWs grown on graphitic substrates by MBE [105].

3.2.2.2 Mapping the Growth Temperature Parameter Space

Growth temperature dependences are considered for InAs NWs formed at constant V/III = 25 and χ_{TMIn} = 16 μmol/min. Under otherwise constant growth conditions, $\mathrm{T_G}$ is varied between 550 °C and 700 °C in increments of 50 °C. Figures 3.4(a)–(d) show 45° tilted-view SEM images of as-grown samples formed in this temperature range. As shown in Figure 3.4(a), NW self-assembly is entirely quenched at growth temperatures of 550 °C and below. In this low-T_G range, a contiguous polycrystalline InAs film is formed through the merger of adjacent islands. Thus, lower growth temperatures may be exploited for pseudo-vdWE of III-V thin films on 2-D nanomaterials. At $\mathrm{T_G}$ ~600 °C and above, vertically-oriented InAs NWs are self-assembled in large-area arrays with aspect ratios and number densities that are strongly dependent upon temperature.

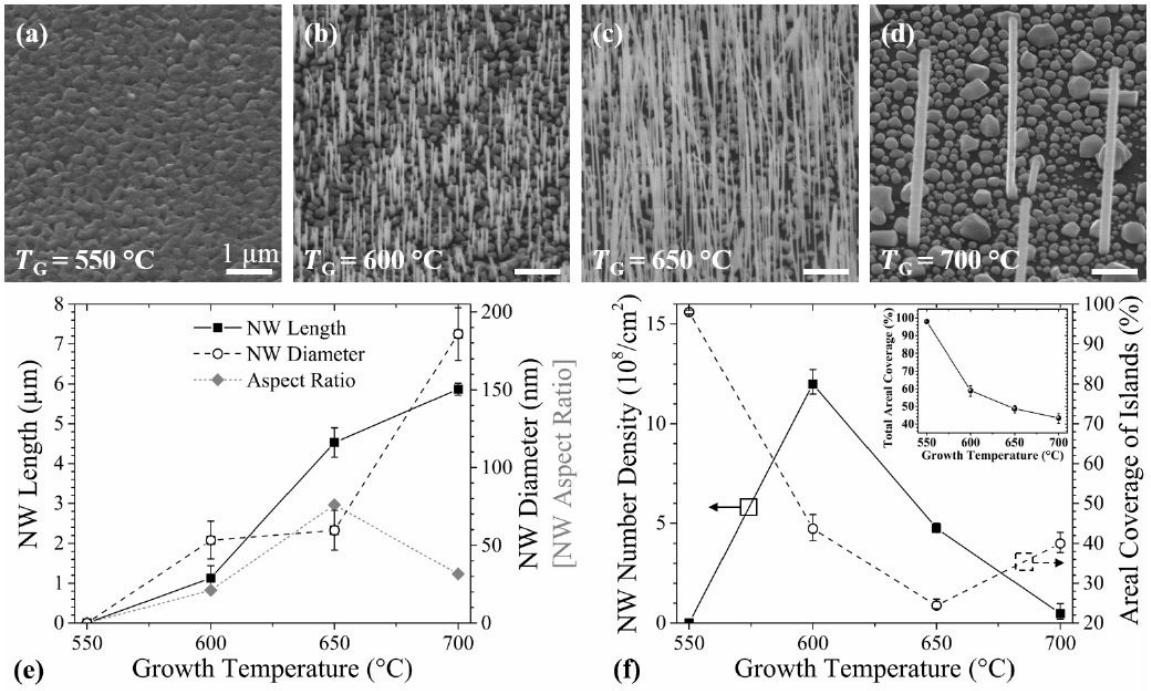

Figure 3.4: Temperature dependence: 45° tilted-view SEM images of as-grown InAs NWs on SLG at T_G of (a) 550 °C, (b) 600 °C, (c) 650 °C, and (d) 700 °C, under constant V/III = 25, and χ_{TMIn} = 16 μmol/min. All scale bars represent 1 μm. Measured value for (e) NW height, diameter, and aspect ratio and (f) NW number density and parasitic island areal coverage are plotted as functions of T_G. Inset of (f) shows total areal coverage of both NWs and parasitic islands as a function of T_G.

In Figure 3.4(e), measured mean values for NW length (black square data points with solid trend line), NW diameter (white circle data points with dashed trend line), and NW aspect ratio (gray diamond data points with dotted trend line) are plotted with respect to growth temperature. Similar to the observations by Anyebe et al. for InAs NWs grown on graphitic surfaces by MBE [108], a maximum NW aspect ratio is found at intermediate temperatures within the suitable T_G range. In the current study, while mean values of NW length and diameter are observed to monotonically increase with T_G in the 600 °C to 700 °C range, a relative enhancement of axial growth rate over radial growth rate at the intermediate of $T_G = 650$ °C results in a maximum aspect ratio of ∼75 after a 300 s growth period.

The above trends can be understood in terms of a balance between temperature-dependent surface mobility of group-III species and desorption of group-V species at the optimal growth temperature. As T_G is raised from 600 °C to 650 °C, a corresponding increase in the thermally-activated surface mobility of group-III growth species enhances a supply of adatoms at the axial NW growth front, leading to a ∼4-fold increase of mean NW length. Such a temperature change does not result in a significant variation of the mean NW diameter (i.e., nominal diameter increase between $T_G = 600$ °C and $T_G = 650$ °C is within measured statistical error). As T_G is further raised from 650 °C to 700 °C, mean NW length is marginally influenced, quantified by an increase of ∼30%. In contrast, radial growth is more dramatically impacted, resulting in over 3-fold enlargement of mean NW diameters. This can likely be attributed to thermal decomposition and enhanced desorption of group-V species at $T_G = 700$ °C. A reduction in supply of diffusive growth species at the axial growth front can lead to accelerated rates of sidewall nucleation and, therefore, diameter expansion. A similar increase in radial NW growth at the expense of axial growth under elevated temperatures has been reported for various seed-free InAs NW systems [123], [127]. Moreover, the trends for NW length and diameter variation as a function

temperature observed here are also representative of temperature-dependent growth trends reported for the diffusion-limited NW growth regime [128–133].

The number density and areal coverage of parasitic islands is also dramatically affected by growth temperature. Figure 3.4(f) plots the measured number density of NWs per area (black square data points with solid trend line) and surface area coverage percentage of parasitic 3-D islands (white circle data points with dashed trend line) with increasing T_G. As previously noted, low-temperature growth conditions favor the formation of low aspect ratio island structures leading to the deposition of contiguous films, quantified by nearly 100% areal coverage of parasitic growth at T_G = 550 °C. Above this temperature range, parasitic island coverage rapidly reduces, coincident with the initiation of NW growth in high number densities at 600 °C. The optimal T_G range for high density NW array self-assembly is between 600 °C to 650 °C. However, as indicated in Figure 3.4(f), both the number density of NWs and areal coverage of parasitic island decrease with increasing temperature in the optimal T_G range.

These observations may be explained based on the low adsorption energy of both In and As growth species on graphene, which itself possesses a low surface energy. While direct nucleation is enhanced on an As-terminated graphene surface in comparison to an unmodified and inert graphene surface [107], increasing T_G results in preferential desorption of group-V species and, therefore, leads to a reduction in InAs nucleation rate. Consequently, the nucleation of both $(\overline{111})$-oriented InAs structures, which lead to NW formation, and otherwise oriented InAs nuclei, which contribute to parasitic growth, is quenched with increasing temperature. This is supported by the observation that the total areal coverage of InAs on the graphene surface, stemming from contributions from both NW and parasitic structures, rapidly decreases with rising T_G, as shown in the inset of Figure 3.4(f).

From a kinetic perspective, the notable distinction between growth at 600 °C and

650 °C is that, under a constant supply of group-III species (i.e., given near-unity decomposition efficiency of TMIn at all tested values of T_G [134]), the diffusivity of adsorbed In atoms on both SLG and InAs surfaces is enhanced with temperature. Thus, surface migration toward the $(\overline{111})$-oriented NW top facet increases at 650 °C, leading to taller NWs that comprise an array of lower number density. With further increase of T_G to 700 °C, the number density of NWs decays dramatically by ∼96 % in comparison 600 °C. Above the optimal temperature range only few NWs form, likely due to prohibitively high group-V desorption. Parasitic structures with smooth surfaces are also observed at 700 °C, in contrast to the 3-D islands with well-defined crystalline facets found at lower temperatures; the former may result from preferential In clustering on the SLG surface. Given that the current parameter space is not tuned for self-catalyzed VLS growth, In droplets formed under the elevated temperatures fail to accommodate seed-mediated NW assembly. The small collection of NWs that are formed at 700 °C do so through a non-catalytic self-assembly mechanism, similar to those NWs formed at lower temperatures (as evidenced by the absence of In seeds at their tips via TEM inspection even under AsH_3-free post-growth cooling; not shown). Growth under such elevated temperatures may be exploited for applications that require more sparsely positioned vertical NWs on SLG. In summary, the effect of growth temperature on morphology and number density of InAs NWs, as well as areal coverage of parasitic island, for the case of seed-free InAs NWs on graphene via MOCVD has been investigated in a self-consistent approach. We highlight the highest reported axial growth rate of 1174 nm/min at an elevated temperature of 700 °C (in comparison to ∼900 nm/min at an optimal temperature of 650 °C). The maximum growth rate found here is roughly 27 times faster than the reported growth rate of MBE-grown InAs NWs on graphitic substrates [105], and roughly 3.4 times faster than the growth rate of InAs NWs on SLG by MOCVD [109].

3.2.2.3 Mapping the Total Molar Flow Rate Parameter Space

The final growth parameter variation investigated here is the total molar flow rate of precursors. At constant $T_G = 650$ °C, the total flow rate of precursors (i.e., $\chi_{Total} = \chi_{AsH_3} + \chi_{TMIn}$), which can be considered as equivalent to a metric that tracks growth rate, was modified while maintaining a constant V/III ratio of 25. For simplicity, the results are reported and discussed with respect to the molar flow rate of TMIn, χ_{TMIn}, as a single variable. However, it should be noted that the total flow of both metal organics and hydrides was varied in sequential growth trials, while keeping V/III ratio constant.

Figures 3.5(a)–(d) show as-grown NW arrays formed under increasing TMIn flow rates, in the $\chi_{TMIn} = 8$ to 32 μmol/min range. Figure 3.5(e) plots values of mean NW length (black square data points with solid trend line), diameter (white circle

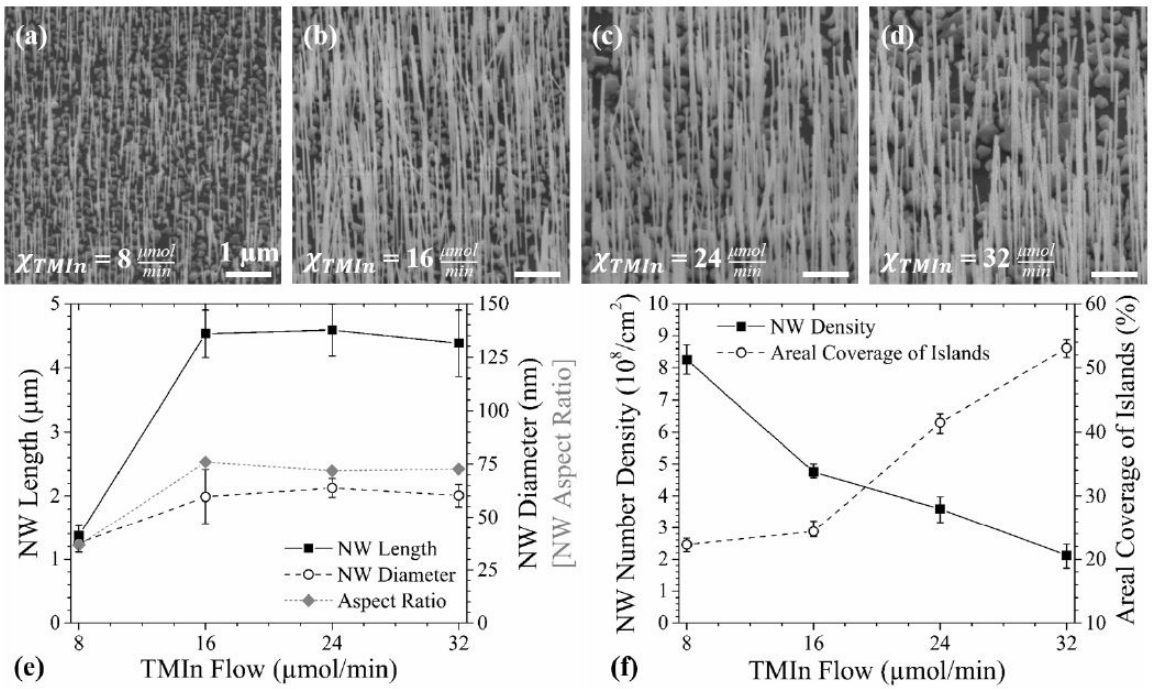

Figure 3.5: Flow rate dependence: 45° tilted-view SEM images of as-grown InAs NWs on SLG at χ_{TMIn} of (a) 8 μmol/min, (b) 16 μmol/min, (c) 24 μmol/min, and (d) 32 μmol/min, under constant $T_G = 650$ °C and V/III = 25. All scale bars represent 1 μm. Measured value for (e) NW height, diameter, and aspect ratio and (f) NW number density and parasitic island areal coverage are plotted as a function of χ_{TMIn}.

data points with dashed trend line), and aspect ratio (gray diamond data points with dotted trend line) measured from samples grown at TMIn flow rates specified in panels (a)–(d). For the same set of growth trials, measured values of mean NW number density (black square data points with solid trend line) and surface area coverage percentage of parasitic 3-D islands (white circle data points with dashed trend line) are quantified in Figure 3.5(f). Under low-flow conditions of χ_{TMIn} = 8 μmol/min, NWs with mean lengths and diameters of ∼1.4 μm and ∼40 nm are formed, respectively, after a growth period of 300 s. Doubling the flow rate to χ_{TMIn} = 16 μmol/min induces a rapid enhancement of axial growth with only moderate increase in radial growth, such that NW lengths and diameters increase to ∼4.5 μm and ∼60 nm, respectively. The result is an approximate doubling of aspect ratio to a value of ∼75 at 16 μmol/min. Under elevated precursor flow rate conditions, both NW length and diameter show little deviation from mean values observed at χ_{TMIn} = 16 μmol/min (i.e., within the measured error range), resulting in a saturation of aspect ratio.

This seemingly counterintuitive trend, whereby a continual increase of precursor supply fails to accommodate a corresponding increase in NW volume, can be understood with respect to a reduction of In atom diffusivity under higher χ_{TMIn} conditions and the role of parasitic islands as additional atomic sinks. As shown in Figure 3.5(f), NW number densities experience a monotonically decreasing trend while the areal coverage of parasitic islands continually grows with additional precursor supply. Nearly a four-fold reduction of NW number densities and over two-fold expansion of parasitic island coverage results from increasing TMIn flow rates from 8 to 32 μmol/min under a constant V/III ratio. As surface migration of In atoms is obstructed under higher flow rate conditions, preferential nucleation on 3-D islands causes rapid expansion of parasitic structures, while diffusion along NW sidewalls toward the low energy sink at the NW tips is quenched. Thus, excess supply of growth

species under high χ_{TMIn} conditions contributes disproportionately to parasitic island growth over NW growth. The reduction in NW number density may stem from the coalescence of existing NW structures and laterally expanding parasitic structures during higher precursor supply conditions. The observed growth trends indicate that for simultaneous realization of NW arrays containing maximal number density and aspect ratio, a two-step flow-modulated growth procedure involving a nucleation step at low-χ_{TMIn} and a subsequent axial extension step at higher-χ_{TMIn} may be utilized.

Based on the above growth trends, a suitable parameter set has been selected that represents a compromise between conditions that permit the formation of high aspect ratio NWs in high number density arrays and minimal surface coverage of parasitic 3-D islands. This parameter set, defined by V/III = 25, T_G = 650 °C, and χ_{TMIn} = 16 μmol/min, is used as a basis or comparison point for additional experiments with the purpose of: (1) characterizing NW crystal structure; (2) tracking growth evolution; and (3) tuning NW number densities via pre-growth in situ surface treatment and use of a two-step flow-modulated growth procedure.

3.2.2.4 Crystal Phase Analysis

The influence of growth conditions on NW crystal structure is explored via HR-TEM imaging and SAED pattern analysis. Figure 3.6 shows representative TEM images of NWs obtained along the $<\bar{1}10>_{ZB}$ zone axis of the cubic phase from two different growths at T_G = 650 °C. Images in panels (a)-(c) were obtained from a NW grown under a high V/III ratio of 250 and at the optimal precursor flow rate (i.e., χ_{TMIn} = 16 μmol/min). The black border in (a) highlights the approximate location of the image shown in (b), while the white border in (b) indicates the approximate location of the high-magnification and lattice-resolved micrograph displayed in (c). An SAED pattern recorded at the corresponding location is shown in (d). For comparison, images in panels (e)-(g) were collected from a NW grown at the optimal V/III ratio of 25, but

under high precursor flow conditions (i.e., $\chi_{TMIn} = 32$ μmol/min). The black and white boxes in (e) and (f) mark the locations of higher-magnification micrographs in subsequent panels, while (h) shows an SAED pattern recorded along the corresponding location.

Firstly, it is noted that NW morphologies shown in Figure 3.6 are consistent with dimensions described in the above discussion for the specified conditions. The NWs preferentially assemble along the $<\overline{111}>_{ZB}$ direction and are free of threading dislocations due to in-plane pseudo-coherency between InAs and SLG lattices [101], [103], [119]. Even in the absence of lattice-registry, strain relaxation via misfit dislocation generation is not expected in the pseudo-vdWE regime, due to lack of hetero-interfacial covalency and strain sharing [98], [109]. The NWs shown in Figure 3.6, as well as samples grown under all other conditions within the extended parameter space, exhibit a disordered crystal structure consisting of zinc-blende (ZB), wurtzite (WZ), and 4H polytype phases with a high density of stacking faults and rotational

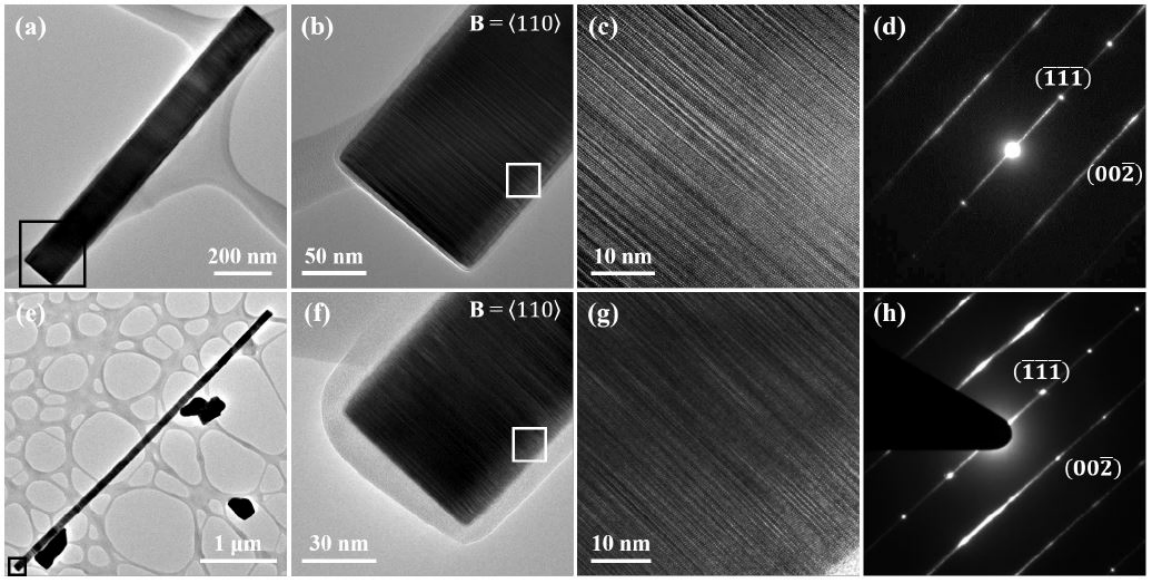

Figure 3.6: TEM images (a-c, e-g) and corresponding SAD patterns (d, h) obtained from two different NWs both grown at $T_G = 650$ °C. The NW captured in (a-d) was formed at high V/III ratio of 250, but at the optimal $\chi_{TMIn} = 16$ μmol/min. The NW shown in (e-h) was formed at the optimal V/III ratio of 25, but at high $\chi_{TMIn} = 32$ μmol/min. The highlighted regions in (a, b, e, f) are shown at higher magnification in subsequent panels.

twin planes. Phase disorder and high planar defect density, visible as lateral striations in the micrographs, are also translated by prominent streaking along the $<\overline{111}>_{ZB}$ axis in the SAED patterns. The crystal structures observed here are consistent with prior reports on vdWE-synthesized InAs and InGaAs on SLG [99], [101], [105], [109], [119]. The representative NWs shown in Figure 3.6, which are either grown under moderate precursor flow and high V/III ratio [i.e., panels (a)-(d)] or moderate V/III ratio and high precursor flow conditions [i.e., panels (e)-(h)], exhibit no single phase WZ segments beyond 10 monolayers, regardless of position along the NW body. Extended ZB segments beyond 10 monolayers can be found, but such segments are not free of rotational twin planes. The same characteristic polytypic crystal structure was also observed for NWs grown under other conditions. Thus, crystal structure is observed to be independent of growth kinetics in the explored parameter space. Notably, the disordered structure extends throughout the tip region of all NWs inspected, regardless of whether or not samples are cooled from the growth temperature under AsH_3 flow. Neither a transition to a single crystal phase nor distinguishable variation in planar defect density is found along tip segments. This is in contrast to the commonly observed "cooling neck" effect in the case of In-catalyzed and Au-seeded InAs NWs, whereby a ZB/WZ phase transition occurs near the catalyst/NW interface under reduced supersaturation conditions stemming from seed depletion in the absence of group-III supply at the end of growth [126], [129], [135].

The subject of phase mixing and polytypism between ZB and WZ structures in VLS-grown III-V semiconductor NWs has been extensively modelled on the basis of fundamental thermodynamics, and crystal phase control has been reliably demonstrated to be a function of growth kinetics [135–137]. The difference in bulk cohesive energy between ZB and WZ phases (i.e., 10.6 meV/octet pair for InAs [136]) is compensated in VLS-grown NW structures by a reduction in surface energy associated with WZ nucleus formation at a triple phase line [135]. This can enable crystal phase

modulation by controlling the supersaturation of the metallic droplet (i.e., chemical potential difference between liquid and solid phases), which is realized by tuning of growth conditions for a given III-V material system [135–138]. Thus, by kinetically engineering the energy barrier to nucleation, the crystal structure of seed-based InAs NWs can be precisely transformed from ZB to WZ to 4H polytype during growth, as comprehensively demonstrated via both MBE and MOCVD [135], [133, 139–142]. In fact, it has been shown that even planar WZ InAs films can be formed through lateral extension from the base of WZ InAs NWs on ZB substrates [143]. However, for InAs NW self-assembly in the absence of a seed-mediated growth regime, control over phase purity is very challenging.

For the three most commonly employed seed-free InAs NW growth modes, which include selective- area epitaxy (SAE) of InAs NWs on various substrates [144–147], direct epitaxy (DE) of InAsP, InGaAs, and InAs NW on Si (111) substrates [28], [148], [149], and template-assisted epitaxy (TAS) of InAs NWs on Si (110) substrates [150], a disordered lattice consisting of a high density of planar defects is routinely found. While polytypism has been shown to be independent of Si dopant concentration [151–153], some notable alternative strategies have been applied during growth of catalyst-free In-based NWs to induce phase purity. Ji et al. have shown that the introduction of trimethyl-antimony during SAE growth results in the formation of purely ZB phase $InAs_{1-x}Sb_x$ NWs for x = 9.4 % [154]. Soo et al. realized catalyst-free growth of purely WZ InAs NWs on Si (111) through a nano-porous Ni masking layer by MOCVD [155]. While comparable χ_{TMIn} values were employed, the authors carried out growth at a lower V/III ratio (i.e., V/III = 2.9) and a prohibitively lower growth temperature (i.e., T_G = 550 °C) than the current study. As described above, V/III $<$ 25 renders low NW aspect ratio and number densities, while T_G = 550 °C is not conducive to NW formation during vdWE of InAs on SLG. Lastly, Liu et al. have recently carried out comprehensive analysis of phase mixing during SAE of InAs on Si

(111) by MOCVD [156]. The authors successfully realized growth of over 90% WZ phase, and concluded that high T_G, low absolute precursor flow rate, and low V/III ratio conditions are required to preferentially induce an InAs (111)B "unreconstructed" (1 × 1) surface, which favors hexagonal phase nucleation, as opposed to the (2 × 2) reconstructed surface, which favors ZB phase nucleation. While comparable V/III ratios and sufficiently high T_G values were employed by Liu et al. as those in the current work, substantially lower precursor flow rates (i.e., $\chi_{TMIn} = 1$ μmol/min) were required for phase purity. We conclude that, although modification of growth kinetics beyond the parameter window explored here may permit appreciable phase purity as realized by Soo et al. and Liu et al., our observations indicate that such conditions provide critical limitations with respect to template-free self-assembly of high aspect ratio InAs NW structures in arrays of high number density on SLG.

3.2.2.5 Time Evolution Study

Next, NW growth progression is tracked under the preferred parameter space defined by V/III = 25, $T_G = 650$ °C, and $\chi_{TMIn} = 16$ μmol/min. The time evolution of axial and radial growth is monitored over a series of seven runs toward the final growth duration of $t_G = 300$ s. Figure 3.7(a)–(d) shows images from as-grown NW arrays that were formed under the above noted, constant growth conditions after growth periods of $t_G = 60$ – 240 s, respectively (an array formed under the same conditions but after $t_G = 300$ s is shown in Figure 3.7(b)). In Figure 3.7(e), the mean axial growth rates (black square data points and solid guide line) and mean radial growth rates (white circle data points and dashed guide line) are plotted for the 7 growth periods. While axial growth rates appear invariant within the measured error values in Figure 3.7(e), the inset plot showing NW length as a function of growth time clearly highlights a tendency toward reduced axial growth after $t_G = 180$ s, as indicated by the solid portion of the gray fitted data line. Extrapolation of the same fitted curve toward the

starting growth time, indicated by the dashed line segment, shows an absence of an extended incubation period and is contrary to what has been observed in the case of In-seeded InAs NW growth by Grap et al. [125]. Hertenberger et al. emphasized a similarly absent nucleation phase prior to the onset selective-area MBE growth of InAs NWs in support of a seed-free growth mode [156]. It is noted that sidewall nucleation-mediated radial growth leads to continual expansion of the NW diameter over the entire growth period. However, as shown in Figure 3.7(e), the radial growth rate is observed to decline and saturate rapidly within this timeframe. The tendency toward a reduction in axial and radial growth rates is attributed to an increasing competition from additional surfaces for a limited material supply. As growth ensues, a constant supply of growth species is competitively distributed over an expanding collection of parasitic 3-D islands. Such a supply-limited competitive regime is exaggerated over

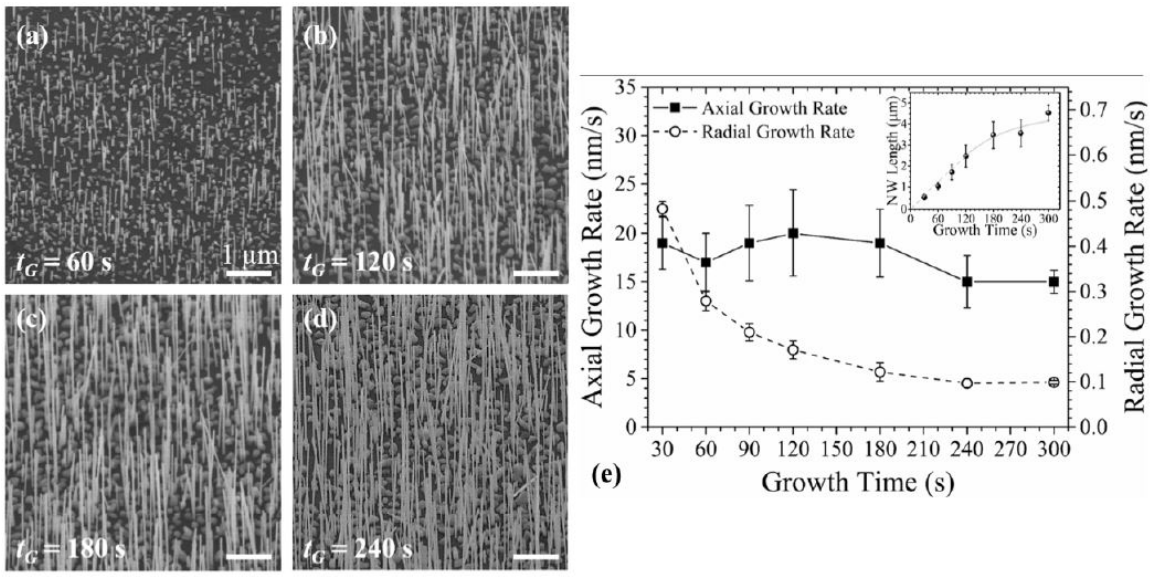

Figure 3.7: Growth evolution of NWs under the selected optimal conditions of V/III = 25, T_G = 650 °C, and χ_{TMIn} = 16 μmol/min. (a-d) show 45° tilted-view images after growth durations of 60 s, 120 s, 180 s, and 240 s, respectively. All scale bars represent 1 μm. (e) NW axial growth rates (black square data points with solid black line) and NW radial growth rates (white circle data points with dashed black line) are plotted for various total growth times between 30 s and 300 s. The inset in (e) shows a plot of measured mean NW length versus growth time to demonstrate the growth rate saturation effect; a linear trend near the origin (i.e., dashed grey line for $t_G \leq 120$ s) is used to demonstrate the absence of a significant incubation phase prior to NW formation.

time as island volumes grow and provide additional surfaces for nucleation, as visible in Figure 3.7(a)–(d). Thus, NW volume expansion declines over time. While growth rates are expected to saturate for longer growth times [157], the selected optimal conditions permit rapid axial growth rates of approximately 900 nm/min within the tested growth period. Compared to the reported growth rate of 43 nm/min for the case of In-seeded [105] and 340 nm/min for seed-free [109] InAs NWs on graphene, 11 nm/min for catalyst-free InAs on Si (111) [157], and 275 nm/min for InAs SAE on Si (111) [158], the optimized growth conditions in the current study enable maximum NW volume yield which holds promise for low-cost manufacturing of InAs NW arrays for applications in optoelectronics (i.e., photodetectors) and nanoelectronics (i.e., wrap-gated field–effect transistors).

3.2.2.6 Growth Optimization for High NW Number Density Arrays

Two additional optimization experiments are conducted with the intention of further reducing the areal coverage of parasitic islands and/or improving the NW number

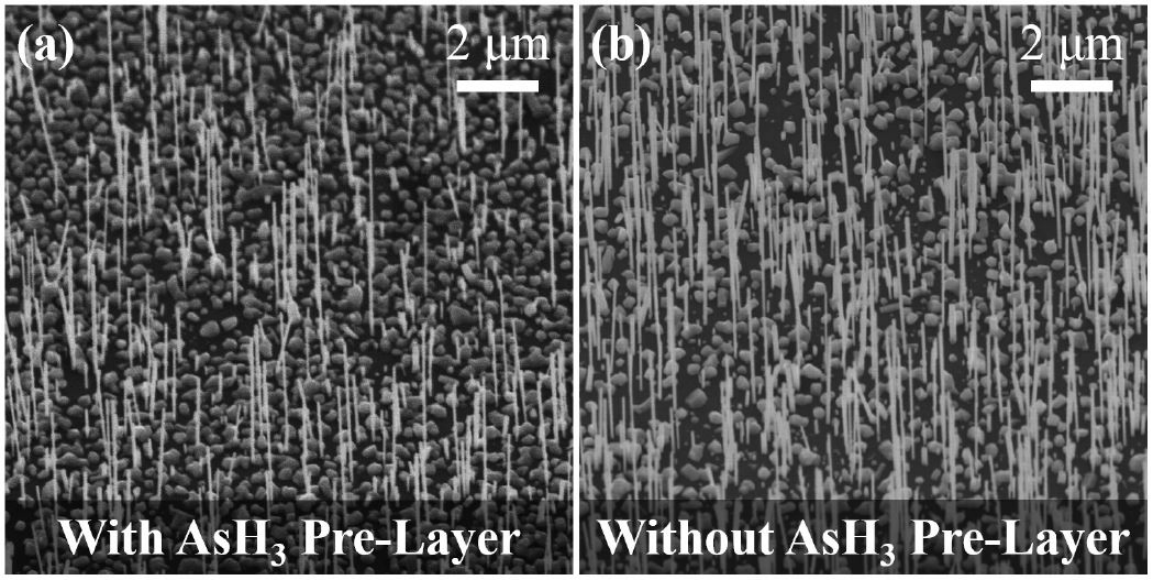

Figure 3.8: 45° tilted-view SEM images of as-grown InAs NWs formed under otherwise constant conditions, but (a) with and (b) without the use of a pre-growth AsH_3 surface treatment.

density under otherwise non-ideal conditions. In the first experiment, the purpose is to test the influence of a pre-growth in situ AsH_3 treatment on the formation of parasitic islands. Here, a low V/III ratio growth condition (i.e., V/III = 5, T_G = 650 °C, χ_{TMIn} = 16 μmol/min) is selected as the starting point, which was shown earlier to produce relatively low NW number densities and high areal coverage percentage of parasitic islands. As demonstrated by Alaskar et al. [107], and noted earlier, the generation of an As-terminated graphene layer greatly enhances the surface energy and promotes further group-III adsorption. Thus, due to its chemically inert surface in the absence of an As pre-layer, an enhancement of surface migration of growth species is expected, leading to fewer nucleation sites and a reduction of parasitic island coverage. Tilted-view SEM images of as-grown NW arrays formed with and without a 300 second pre-growth AsH_3 treatment at T_G = 650 °C are shown in Figures 3.8(a) and (b), respectively. For growth without an AsH_3 pre-layer, the run was initiated at T_G by simultaneously introducing TMIn and AsH_3 flows. In this case, a significant reduction (i.e., by a factor of ∼0.62) in areal coverage of parasitic islands is

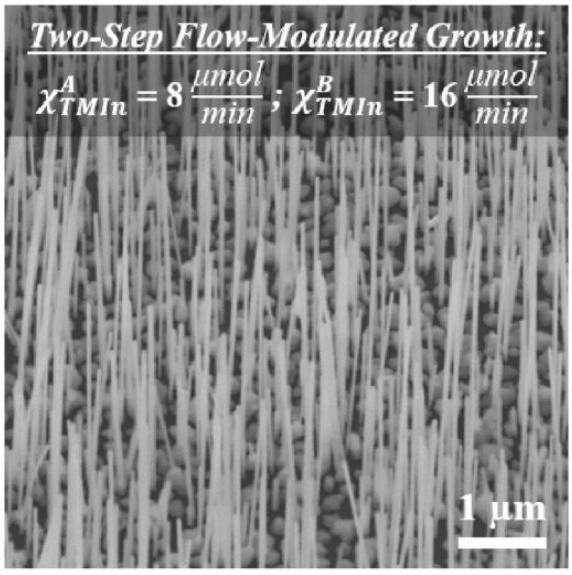

Figure 3.9: 45° tilted-view SEM image of high aspect ratio and high number density InAs NWs grown using a two-step flow-modulated sequence.

Table 3.1: Metrics for NW growths at V/III = 5 with and without AsH_3 pre-flow, compared to V/III = 25 with AsH_3 pre-flow.

Growth Condition	Mean NW Length (μm)	Mean NW Diameter (nm)	NW Number Density (cm^{-2})	Island Areal Coverage (%)
With AsH_3 Pre-Flow V/III = 5	2.1	70.8	3.2×10^8	46.3
Without AsH_3 Pre-flow V/III = 5	3.9	90.5	4.6×10^8	28.5
With AsH_3 Pre-Flow V/III = 25	4.5	59.6	4.8×10^8	24.4

observed. Correspondingly, a notable increase in NW number densities also occurs such that NWs are on average ∼182% taller and ∼128% larger in diameter than those NWs formed after pre-growth AsH_3 treatment. Therefore, the absence of an AsH_3 pre-layer not only results in the suppression of parasitic growth through a reduction (enhancement) of growth species adsorption (surface migration), but also leads to the formation of higher aspect ratio NWs in number densities under low V/III conditions that are comparable to those formed under optimal V/III conditions. The quantitative results from this growth are summarized in Table 1 and compared to results from samples grown with AsH_3 pre-layer under non-ideal and optimal V/III ratios of 5 and 25, respectively.

In the second optimization experiment, we return to the notion of a two-step flow-modulated growth procedure. As noted above, reduced precursor flow rates permit formation of high number density arrays of low aspect ratio NWs. Conversely, as precursor flow rates increase, NW aspect ratio is enhanced at the cost of number density and expansion of parasitic growth. In order to overcome this tradeoff, growth

Table 3.2: Metrics for NW growth under fixed-flow and two-step flow-modulated conditions.

Growth Condition	Mean NW Length (µm)	Mean NW Diameter (nm)	NW Number Density (cm^{-2})	Island Areal Coverage (%)
Fixed-Flow χ_{TMIn} = 8 µmol/min for t_G = 300 s	1.4	37.7	8.6×10^8	22.3
Fixed-Flow χ_{TMIn} = 16 µmol/min for t_G = 300 s	4.5	59.6	4.8×10^8	24.4
Two-Step Flow-Modulated χ_{TMIn} = 8 µmol/min for t_G = 60 s χ_{TMIn} = 16 µmol/min for t_G = 240 s	4.2	51.7	8.3×10^8	54.3

is first conducted at a low flow rate of $\chi_{TMIn} = 8$ μmol/min for a period of 60 s as an initial "NW nucleation stage" so as to force the formation of high number density NW growth sites. Next, flow rates are increased such that $\chi_{TMIn} = 16$ μmol/min for an additional 240 s growth period. Both growth steps are conducted at $T_G = 650$ °C, and under constant V/III ratio (i.e., AsH_3 flow is also doubled during the second growth step).

A representative tilted-view SEM image of a sample formed under the two-step flow-modulated growth mode is shown in Figure 3.9, which can be compared to Figures 3.5(a) and (b) for the cases of fixed-flow growth at $\chi_{TMIn} = 8$ μmol/min and $\chi_{TMIn} = 16$ μmol/min, respectively. The corresponding growth metrics are summarized in Table 2 for these three trials. Through use of the flow-modulated growth mode, NW number densities are improved to comparable values that are realized under low flow rate conditions (i.e., > 8 μmol/min), without sacrificing NW aspect ratio or significantly influencing the axial growth rate (i.e., 840 nm/min). Thus, this optimized mode permits simultaneous realization of dense of NW arrays and formation of structures

with aspect ratios greater than 80. However, under the two-step growth mode, the areal coverage of parasitic islands is observed to increase by more than a factor of two in comparison to alternative fixed-flow conditions. This can likely be attributed to rapid volume expansion during the second growth stage of a higher number density of parasitic islands that were initially formed during the first growth stage.

3.3 Self-Assembly of In-based Ternary III-V Nanowire Arrays on Graphene

Project Title: Self-Assembled InAsP and lnAlAs Nanowires on Graphene Via Pseudo-van der Waals Epitaxy

Citation: M. A. Baboli, M. A. Slocum, A. Giussani, T. S. Wilhelm, S. J. Polly, S. M. Hubbard, and P. K. Mohseni, IEEE 18th International Conference on Nanotechnology (IEEE-NANO), pp. 1–5, 2018.

3.3.1 Introduction

In recent years, nano-hybrid materials systems consisting of GaAs, InAs, InGaAs, and InAsSb NWs on graphene have been demonstrated through the vdWE approach [104], [109], [159]. Growth of III-V NWs on graphene has been realized through various mechanisms, such as self-catalyzed or Au-assisted vapor-liquid-solid (VLS) growth using molecular beam epitaxy (MBE) and MOCVD [100], [102]. Additionally, vertically oriented InAs and InGaAs can also be formed on inert graphitic surfaces through a self-assembly mechanism, which unlike other methods requires no pre-growth lithography step or deposition of metallic seeding agents [101], [109], [159]. However, to our knowledge, no studies have been reported on seed-free heterogeneous integration of InAsP and InAlAs NW arrays on single layer graphene (SLG) via the vdWE approach.

The objective of this study is to reach an InAsP composition of around 20% phosphorous content, to use this composition as the low bandgap sub-cell at 0.5 eV in a multi-junction solar cell. As shown in previous section, self-assembly of InAs NWs on graphene was throughly studies. However, regardless of the growth conditions, self-assembly of binary InP on graphene was not conducive to NW growth as shown in Figure 3.10. Thus, to realize InAsP NW arrays with the target composition, solid

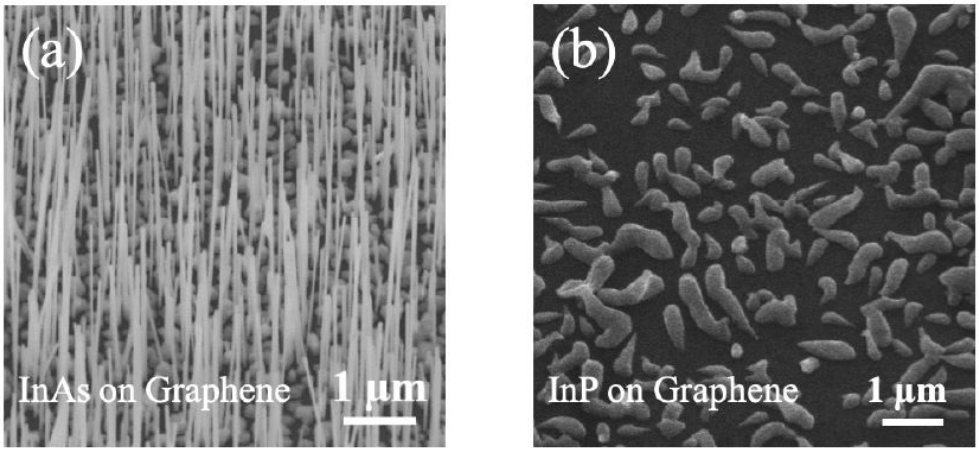

Figure 3.10: 45° tilted SEM image showing (a) integraiton of a dense array of high spect ratio InAs NWs on graphene via self-aasembly approach, (b) Failing self-assembly of binary InP on graphene regardless of growh conditions.

phase P-incorporation was increased via three approaches:

(1) Increasing hydride molar ratio,

(2) Enhancing PH_3 pyrolysis efficiency

(3) Introducing two-temperature heterostructure (TTHS) growth mode

Details of each approach along with the associated results are explained in 3.3.3.1. In addition, compositional and morphological tuning of ternary InAlAs NWs on graphene enabled by NWs self-assembly using MOCVD was studied and presented in 3.3.3.2. In this study, variations in NW morphology and number density are considered with respect to compositionally-dependent atomic configuration and adatom binding energy factors. In this section, the experimental details for self-assembly of $InAs_yP1\text{-}y$ and $In_xAl_{1\text{-}x}As$ NWs is explained in the subsection 3.3.2, followed by results and discussions for each material systems.

3.3.2 Experimental Details

Growth of NWs on SLG nanosheets was performed in an Aixtron 3×2" close coupled shower- head MOCVD reactor. Trimethyl-indium [TMIn, $(CH_3)_3In$] and trimethyl-aluminum [TMAl, $(CH_3)_6Al_2$] were used as group-III precursors; arsine (AsH_3) and

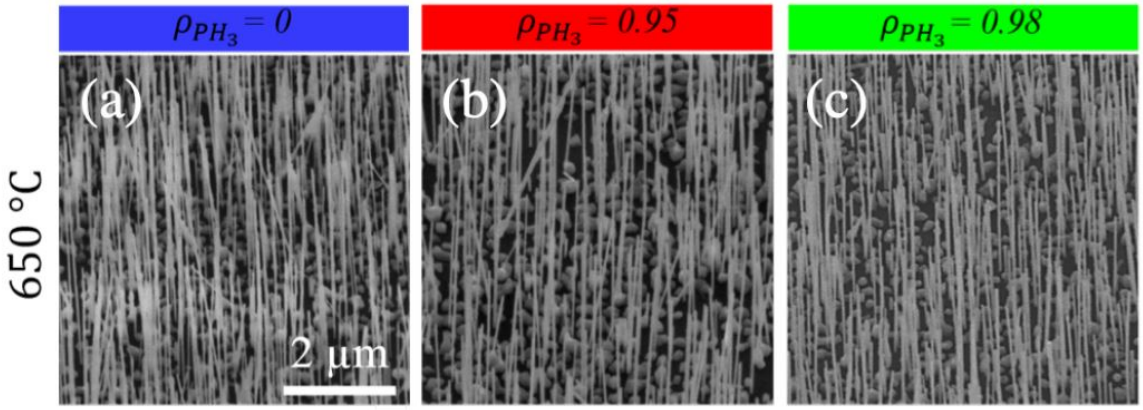

Figure 3.11: 45°-tilted SEM image of $InAs_yP_{1-y}$ NWs grown at $T_G = 650$ °C for ρ_{PH_3} of (a) 0, (b) 0.95, (c) 0.98. All scale bars indicate 2 μm.

phosphine (PH_3) were used for supply of group-V growth species. In the present work, $InAs_yP_{1-y}$ NWs were grown using various hydride precursor molar flow ratios, defined by

$$\rho_{PH_3} = \frac{\chi_{PH_3}}{\chi_{PH_3} + \chi_{AsH_3}} \tag{3.1}$$

χ_{AsH_3} and χ_{PH_3} represent the molar flowrate of AsH_3 and PH_3, respectively. Similarly, $In_xAl_{1-x}As$ NW compositions were modified by varying the molar flow ratio of metal organic precursors, defined by

$$\rho_{TMAl} = \frac{\chi_{TMAl}}{\chi_{TMAl} + \chi_{TMIn}} \tag{3.2}$$

χ_{TMIn} and χ_{TMAl} represent the molar flow rate of TMIn and TMAl, respectively. Growth temperatures (T_G) in the 600 °C to 750 °C range were investigated. In all cases, samples were heated to the desired growth temperature under a constant AsH_3 flow prior to growth initiation. The onset of crystal growth was marked by the introduction of group-III precursor(s). After a growth duration of 300 s, samples where cooled under constant supply of group-V precursors. For all samples, hydrogen (H_2) was used as the carrier gas with total flow of 7 L/min, and the reactor pressure

was maintained at 100 mBar.

Samples were imaged with Hitachi S-4000 and TESCAN MIRA3 scanning electron microscopes (SEM). X-ray diffraction (XRD) measurements were made using a Bruker D8 high-resolution X-ray diffractometer.

3.3.3 Results and Discussions

3.3.3.1 Self-Assembly of $InAs_yP_{1-y}$ Nanowire Arrays on Graphene

The focus of this study is to investigate self-assembly of InAsP and InAlAs NWs on SLG through the vdWE approach, and to explore the influence of key growth parameters on the composition and morphology of resulting NWs. Growth of these two ternary III-V compounds is then compared with the well-studied case of binary InAs NWs on SLG. Firstly, vertically oriented ternary $InAs_yP_{1-y}$ NWs (i.e., for $1 \leq y \leq 0.8$) were grown on SLG through vdWE. Three sets of experiments were carried out to study the incorporation of solid phase phosphorous in InAsP NWs. In the first experiment, T_G was set to 650 °C while ρ_{PH_3} was varied from 0 to 0.98. In Figure 3.11, InAs NWs ($\rho_{PH_3} = 0$, Figure 3.11(a)) are compared to InAsP NWs grown under (b) $\rho_{PH_3} = 0.95$ (Figure 3.11(b)) and (c) $\rho_{PH_3} = 0.98$ (Figure 3.11(c)). Since nucleation

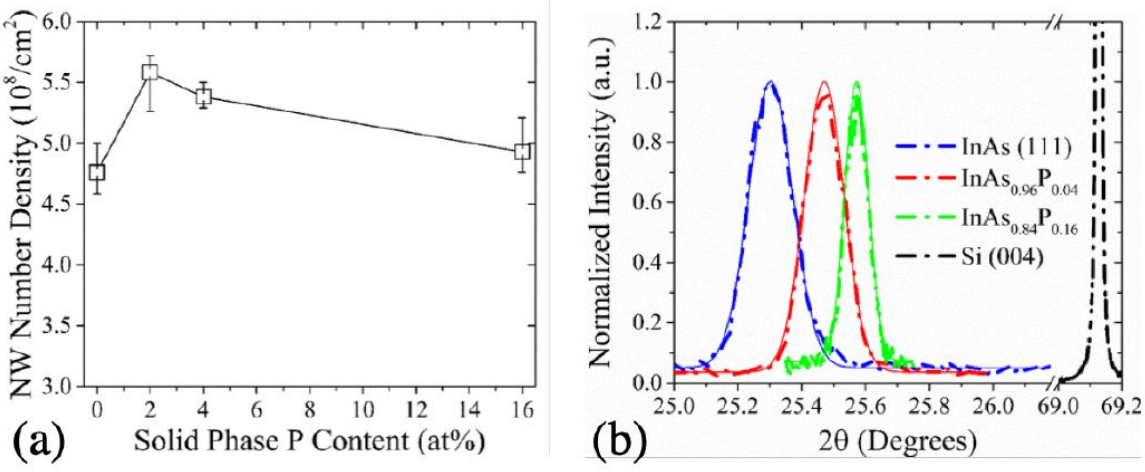

Figure 3.12: (a) NW number density versus percentage of solid phase P-content, (b) XRD specular 2θ-ω scans used to quantify the InAsP solid phase P-content.

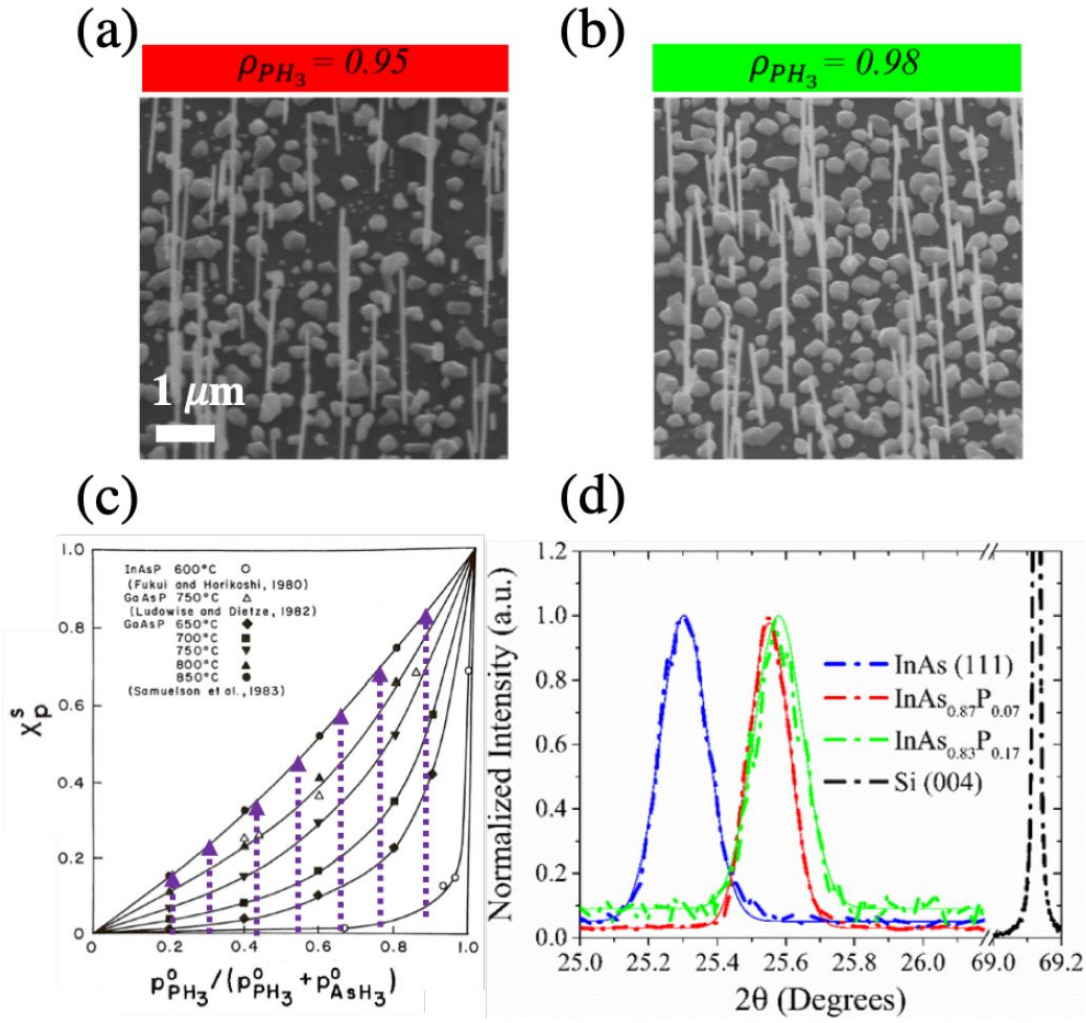

Figure 3.13: 45°-tilted SEM image of $InAs_yP_{1-y}$ NWs grown at T_G = 700 °C for ρ_{PH_3} of (a) 0.95, (b) 0.98. (c) Solid phase P-content in bulk GaAsP and InAsP as a function of hydride molar flow ratio and temperature [93], (d) XRD specular 2θ-ω scans used to quantify the InAsP solid phase P-content.

sites are not limited to any patterned openings or catalyst seeds, self-assembly by vdWE results in growth of NWs as well as parasitic islands. NW lengths, diameters and number density, as well as areal density of parasitic islands are independent of ρ_{PH_3} (Figure 3.12(a)). Figure 3.12(b) shows XRD measurements from as-grown InAsP NWs used to quantify solid phase phosphorous content for ρ_{PH_3} = 0.95 (red plot) and ρ_{PH_3} = 0.98 (green plot). Compositional analysis of this sample set indicates P-incorporation increases from 4 at% to 16 at% by increasing ρ_{PH_3} from 0.95 to 0.98.

It is worth noting here that furthur increased in ρ_{PH_3} leads to higher P-incorporation, however PH_3 flows beyond this level are MFC-limited for our MOCVD reactor.

In order to achieve higher incorporation of solid phase P-content, this experiment was also repeated at $T_G = 700$ °C for the same molar flow ratios. Shown in Figures 3.13 (a) and (b) are 45 °C tilted SEM images of self-assmled InAsP NWs grown at $T_G = 700$ °C with ρ_{PH_3} of 0.95 and 0.98, respectively. The idea here is to increase the pyrolysis efficiency of PH_3 by increasing the T_G. This concept is studied on similar material systems (i. g. GaAsP and InAsP) for film growth, as demonstrated in Figure 3.13(c) [93]. As arrows in Figure 3.13(a) are showing, for the same hydride molar flow ratio, increasing the temperature changes the solid phase P-incorporation. This is due to strong dependance of solid composition to the growth temperature when AsH_3 and PH_3 are used as group V precursors [93]. As before, NW morphology and number density, as well as parasitic island coverage were observed to be independent of ρ_{PH_3}.

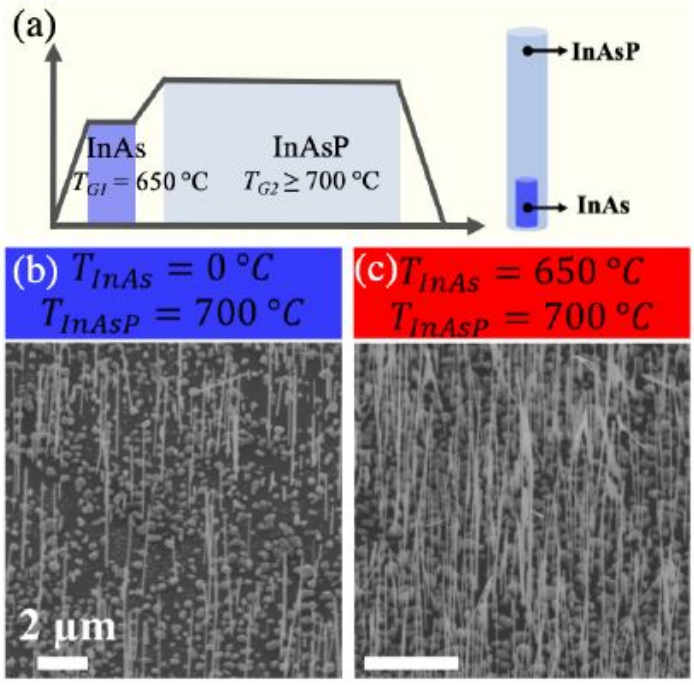

Figure 3.14: (a) Growth sequence and resulted heterostructured NW from TTHS growth mode, (b) One-temperature InAsP NWs at $T_G = 700$ °C. InAs - $InAs_yP_{1-y}$ NWs grown under two-temperature regimes: (c) $T_{G1} = 650$ °C, T_{G2} =700 °C.

However, comparing Figure 3.11 with Figure 3.13 (a) abd (b) clearly shows increasing T_G adversely affects the NW number density. The same trend was also observed for case of InAs NWs on graphene [159]. Figure 3.13(d) demostrated the XRD results for the case of $T_G = 700$ °C, for $\rho_{PH_3} = 0.95$ (red plot) and for $\rho_{PH_3} = 0.95$ (green plot). For $\rho_{PH_3} = 0.95$, inchearsing T_G from 650 °C to 700 °C resulted in a composition change from $InAs_{0.96}P_{0.04}$ to $InAs_{0.93}P_{0.07}$. In the same way, for $\rho_{PH_3} = 0.98$, 50 °C change in T_G leade to $InAs_{0.83}P_{0.17}$.

To overcome the challenge with NW number density dependence at elevated temperature, two-temperature heterostructure (TTHS) growths were performed in a third experiment. A simple schematic of TTHS growth mode can be seen in Figure 3.14(a). InAs growth was first initiated at a low T_{G1} of 650 °C for 60 s to establish a high number density of NWs acting as seeding or pedestal layer. Then T_G was ramped up to 700 °C and 750 °C, in different runs, while ρ_{PH_3} was raised to 0.95 in order to incorporate a higher P-content in the solid phase over a period of 240 s. Figure 3.14(b) shows $InAs_{0.93}P_{0.07}$ NWs grown with $\rho_{PH_3} = 0.95$ at $T_{G1} = 700$ °C in a one-temperature regime, where a low NW number density is observed. However, Figure 3.14(c) shows that by using a two-temperature growth sequence (i.e., $T_{G1} =$ 650 °C; $T_{G2} = 700$ °C at $\rho_{PH_3} = 0.95$), a high density array of InAsP NWs with the same P-content (i.e., 7 at%) can be achieved (red plot in 3.15(a)). As expected, increasing T_{G2} to 750 °C results in NW number density reduction, but enables P-content enhancement for growth of $InAs_{0.83}P_{0.17}$ NWs (green plot in 3.15(a)). Similar temperature-dependent density trends were observed for InAs NWs on SLG [159].

Figure 3.15(b) summarizes results of XRD measurements for all three experiments, where solid phase phosphorus content is plotted as a function of ρ_{PH_3}. A direct comparison between growths of InAsP NWs under the above set of conditions indicates a non-linear P-incorporation trend for different growth temperatures, which is in agreement with bulk InAsP growth trends by MOCVD shown in 3.13 (c) [93].

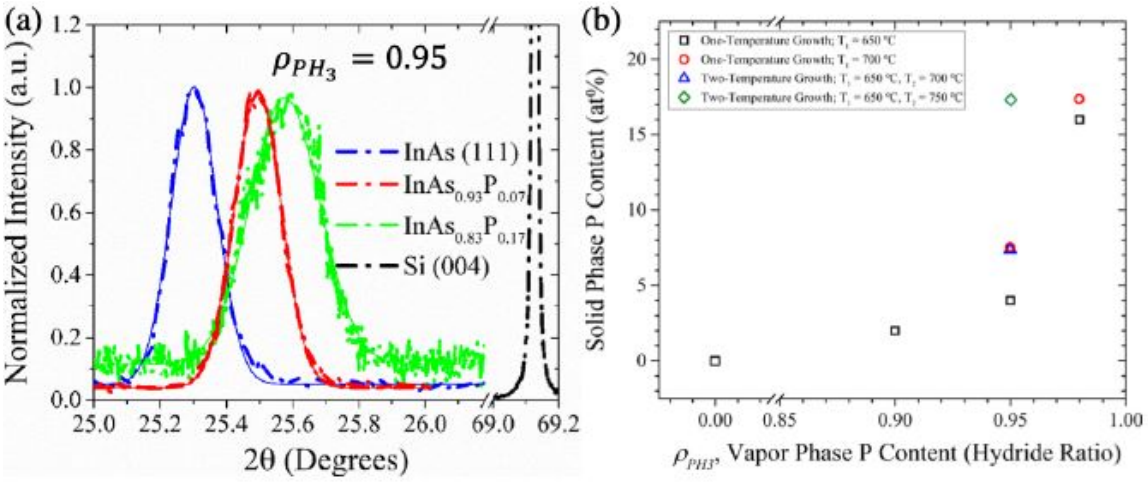

Figure 3.15: (a) XRD specular 2θ-ω scans used to quantify the InAsP solid phase P-content (Unpublished work by Mohadeseh A. Baboli et al.). (b) Summary of solid phase P-content as a function of ρ_{PH_3} for all one- and two- temperature InAsP growths.

Importantly, XRD measurements show no evidence of compositional phase segregation for InAsP NWs investigated here, which is in contrast to the case of InGaAs NWs on SLG where the ternary phase is formed by group-III alloying [109]. Our results indicate that vdWE of high P-content $InAs_yP_{1-y}$ for $y < 0.8$ on SLG is difficult to achieve via direct self-assembly within the explored growth parameter space. However, higher P-content InAsP and even binary InP shell segments can be formed on existing InAsP NW core segments grown on SLG.

3.3.3.2 Self-Assembly of $In_xAl_{1-x}As$ Nanowire Arrays on Graphene

In a separate study, vdWE of $In_xAl_{1-x}As$ NWs on SLG was explored in two sets of experiments. Firstly, at constant $T_G = 600$ °C, $In_xAl_{1-x}As$ NWs are grown with ρ_{TMAl} between 0 and 0.50 at a constant V/III ratio of 25. Figure 3.16 shows 45° tilted-view SEM images of InAlAs grown on SLG, at (a) ρ_{TMAl} of 0, (b) ρ_{TMAl} of 0.25, and (c) ρ_{TMAl} of 0.50. For ρ_{TMAl} of 0, a dense array of InAs NWs is observed. Introduction of Al results in a dramatic change in NW morphology, number density, and directionality. Unlike the case of InGaAs NWs on SLG [109], we find that reduction in In-content, associated with incorporation of higher Al-content, does not induce NW bending.

Figure 3.16 quantifies the length and diameter of InAlAs NWs grown at $T_G = 600$ °C under ρ_{TMAl} values between 0 and 0.5; data points represent mean values measured from >20 NWs. Compared to binary InAs NWs (i.e., $\rho_{TMAl} = 0$) grown at the same temperature, the introduction of TMAl causes a dramatic reduction of NW length and enhancement of NW diameter. This can likely be attributed to limited surface migration of Al atoms during epitaxy. Tapered NW morphologies are only observed under high ρ_{TMAl} conditions and at $T_G = 600$ °C, also likely due to low Al surface migration compared to In. Moreover, NW verticality suffers with increasing Al-content, such that mostly tilted NWs are found at $\rho_{TMAl} = 0.5$.

A growth temperature dependence study is performed for InAlAs NWs grown at constant V/III = 25 and $\rho_{TMAl} = 0.50$. Shown in Figure 3.17 are 45° tilted-view SEM

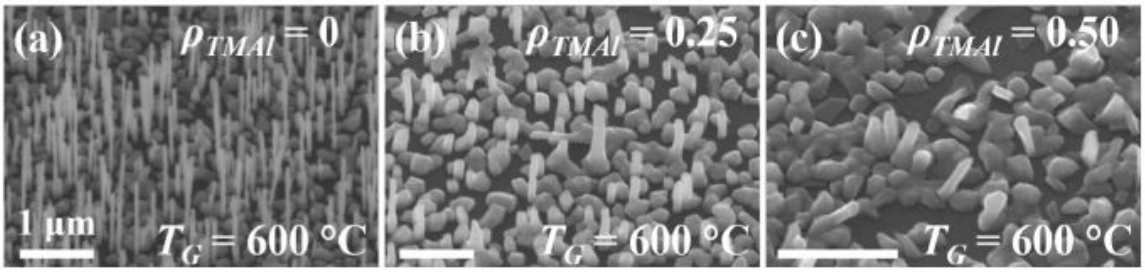

Figure 3.16: 45°-tilted-view SEM images of as-grown $In_xAl_{1-x}As$ NWs on SLG at ρ_{TMAl} (a) of 0, (b) of 0.25, and (c) of 0.50. All scale bars represent 1 μm.

images of InAlAs NWs formed on SLG at T_G of (a) 600 °C, (b) 650 °C and (c) 700 °C. Growth at $T_G = 600$ °C results in formation of very few vertically oriented NWs on SLG and favors formation of parasitic islands, from which NW structures may extend. However, a 50 °C increase in T_G modifies the growth kinetics such that the density of vertically-oriented NWs increases, while areal coverage of parasitic islands reduces. As T_G is raised further from 650 °C to 700 °C, growth of InAlAs NWs is quenched, leading to formation of a contiguous III-V film.

This trend can be explained in terms of a balance between decomposition efficiencies of TMIn and TMAl and temperature-dependent surface mobility of In and Al atoms at these temperatures. Since TMIn shows near-unity decomposition efficiency in this T_G range [134], the change in surface diffusion and availability of Al atoms (i.e., decomposition percentage of TMAl) plays the predominant role. Thus, the abundance of available In atoms is less sensitive to T_G in the explored temperature range than the abundance of Al atoms, while In atoms experience enhanced surface migration compared to Al atoms at all temperatures [160, 161]. As a result, the limiting factor at 600 °C is likely the low thermally-promoted surface diffusion of both group-III species, leading to high polycrystalline island growth. Instead, at 700 °C, the limiting factor for surface diffusion is the abundance of Al atoms due to greater TMAl

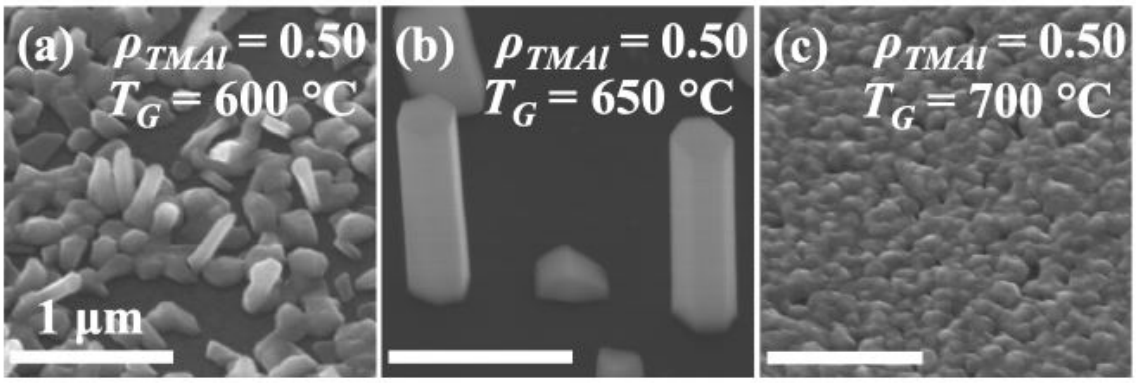

Figure 3.17: 45°-tilted-view SEM images of as-grown $In_xAl_{1-x}As$ NWs on SLG at T_G of (a) 600 °C, (b) 650 °C and (c) 700 °C. All scale bars represent 1 μm.

decomposition. This influence quenches NW growth and forces lateral extension of a high-density collection of polycrystalline islands, thereby leading to film formation. At intermediate temperatures, a balance point is reached between these competing factors. Thus, $T_G = 650$ °C may likely represent a tradeoff temperature at which sufficient thermally-promoted surface migration of less abundant Al atoms occurs, such that both group-III species can reach the top facets of <111> oriented nuclei and, consequently, accommodate vertical InAlAs NW formation.

As a final point of discussion, the results of vdWE for InAsP and InAlAs NW groups are compared. As briefly noted in the Introduction, due to the absence of covalent bond formation, strain sharing is inhibited at the III-V epilayer/graphene interface. Thus, the III-V lattice formed in the vdWE mode may not pseudomorphically adopt a lattice constant other than its inherent one.

Additionally, for In-based structures grown in the vdWE regime on SLG, it has been shown that the lower-most flatly reconstructed III-V monolayer possesses a polar orientation such that group-III species are directly interfaced with C [119]. In the case of InAs on SLG, the native InAs lattice allows for residence of In atoms above graphene H-sites; the same may also be expected for $InAs_{0.8}P_{0.2}$ [100]. While

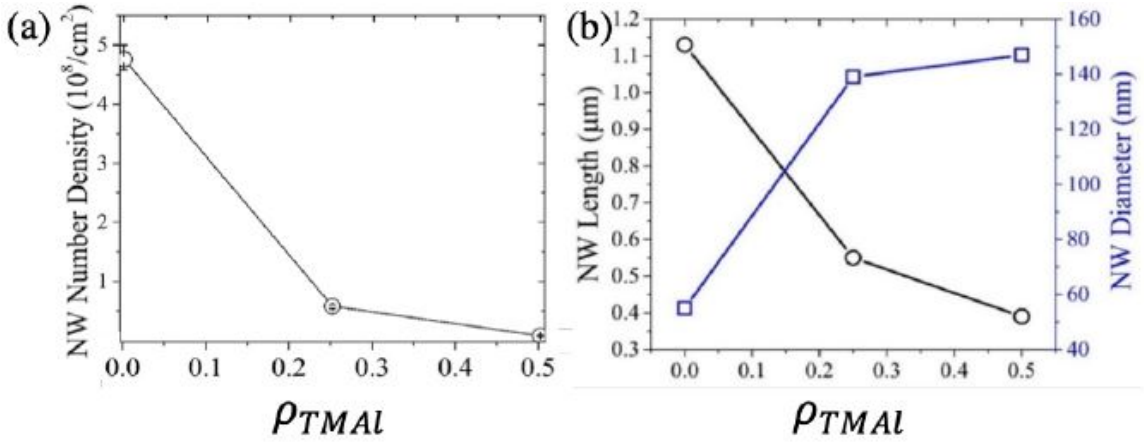

Figure 3.18: $In_xAl_{1-x}As$ NW number density versus percentage of solid phase Al-content, (b) Mean $In_xAl_{1-x}As$ NW length (black data points) and diamter (blue data points) vs. at $T_G = 600$ °C.

B-site residence is most energetically stable for both As and P atoms according to calculations by Nakada and Ishii [118], the residency competition between group-V species in the case of InAsP is not expected to change the position of In atoms from H-site to B-site. Therefore, formation of ternary $InAs_{0.8}P_{0.2}$ (i.e., in comparison to binary InAs) is not expected to shift In atom positions to B-sites. Correspondingly, little variation in the number density of NWs is observed comparing vdWE of InAs and InAsP on SLG. Figure 3.12(a) quantifies the change in NW number density for $InAs_yP_{1-y}$ NWs grown under otherwise constant growth conditions while ρ_{PH_3} is varied between 0 and 0.98 (i.e., $1 \leq y \leq 0.84$). However, introducing Al as a group-III species, which can reside at the interface, into the InAs lattice significantly changes NW morphology and number density. As shown in Figure 3.18(b), a ∼60-fold reduction in NW number density results by increasing ρ_{TMAl} from 0 to 0.50. Chan et al. reported calculations of binding energy for various group-III metallic atoms on graphene [117]. For $In_xAl_{1-x}As$ with low Al content, both In and Al adatoms were shown to reside on the energetically favorable H-site [117, 118]. However, by increasing Al-content, a reduction in the $In_xAl_{1-x}As$ lattice constant forces an altered atomic configuration at the growth interface such that Al resides on the B-site [117, 118]. Since Al has a higher binding energy when situated above the B-site, formation of InAlAs NW structures (i.e., versus polycrystalline islands) on SLG likely becomes less favorable and NW growth becomes quenched (i.e., Figure 3.16). In conclusion, formation of InAsP, InAlAs, and InP/InAsP NWs via pseudo-vdWE on SLG is reported for the first time. Self-assembly of $InAs_yP_{1-y}$ NWs on SLG is achieved for $1 \leq y \leq 0.8$. Solid phase P-content and number density of NWs are strongly dependent on growth temperature. Higher P-content NWs have been realized via a two-temperature growth regime. The dependence of $In_xAl_{1-x}As$ NW composition and morphology on growth temperature and ρ_{TMAl} have been investigated for $1 \leq x \leq 0.5$. Although NW number density was shown to have an inverse dependence upon Al-content, well-defined vertical

NWs were realized at $T_G = 650$ °C and $\rho_{\mathrm{TMAl}} = 0.5$. A general trend for vdWE of InAsP and InAlAs NWs has been discussed to relate NW number densities to lattice coordination and binding energy of growth species on SLG. We anticipate the use of such hybrid nanosystems in low-cost optoelectronics and high-efficiency tandem-junction photovoltaics.

3.4 Conclusion

In the first part of this chapter, the exploration of an extended growth parameter space for self-assembly of InAs NWs on graphene by MOCVD has been presented. The dependences of NW length, diameter, and number density of as-grown arrays, as well as the areal coverage of unintentionally deposited parasitic islands, have been quantified as a function of critical epitaxy parameters including growth temperature, V/III ratio, and absolute flow rate of metalorganic and hydride precursors. A compromise between maximal NW aspect ratio, maximal NW number density, and minimal parasitic growth coverage is reached for the set of growth conditions defined by $T_G = 650$ °C, V/III = 25, and $\chi_{\mathrm{TMIn}} = 16$ μmol/min. While strategies for realization of the crystal phase purity during seed-free InAs NW growth have been discussed, it is noted that the NW crystal phase remains invariantly polytypic and comprised of disordered phases of ZB and WZ layers under all currently explored sets of growth conditions. Tracking the NW growth evolution under optimal conditions indicated that both axial and radial growth rates reduce and saturate over time, likely stemming from a growth regime wherein a constant precursor supply is competitively distributed amongst expanding NW and parasitic island volumes. It has been shown that growth results can be further optimized by two additional approaches. Elimination of a pre-growth in situ AsH_3 treatment causes reduction of growth species surface adsorption during the vdWE of InAs on SLG, which results in minimization of undesired parasitic growth. Moreover, use of a two-step flow-modulated growth mode has enabled further NW aspect ratio

enhancement (i.e., to values > 80) as well as substantial increase in NW number densities (i.e. to values of $\sim 8.3 \times 10^8$ cm^{-2}). Gaining an understanding of the current parameter space provides a basis for the growth of additional InAs-based ternary alloys through the incorporation of P and/or Al for extended bandgap engineering.

In the second part of this chapter, formation of InAsP, InAlAs, and InP/InAsP NWs via pseudo-vdWE on SLG is reported for the first time. Self- assembly of $InAs_yP_{1-y}$ NWs on SLG is achieved for $1 \leq y \leq 0.8$. Solid phase P-content and number density of NWs are strongly dependent on growth temperature. Higher P-content NWs have been realized via a two-temperature growth regime. The dependence of $In_xAl_{1-x}As$ NW composition and morphology on growth temperature and ρ have been investigated for $1 \leq x \leq 0.5$. Although NW number density was shown to have an inverse dependence upon Al-content, well-defined vertical NWs were realized at $T_G = 650$ °C and $\rho = 0.5$. A general trend for vdWE of InAsP and InAlAs NWs has been discussed to relate NW number densities to lattice coordination and binding energy of growth species on SLG.

This work is intended to serve as a guide for control over desired NW morphologies and number densities during vdWE growth of III-V NWs on inert substrates. While this materials system enables a series of nano-hybrid flexible nanoelectronics and optoelectronics device applications, it is also envisioned that III-V/SLG integrated nano-composites can be coupled to existing device architectures as supplementary components of hierarchical systems. Self-assembled arrays of In-based III-V NWs on SLG are also considered for use in tandem-junction solar cell designs as low bandgap sub-cells, such that SLG serves as a transparent and high-conductivity (i.e., n++) component of a tunnel junction when coupled to intermediate (e.g., Si) or high (e.g., GaAsP) bandgap sub-cells.

Chapter 4

Mixed-dimensional InAs Nanowires on Layered Molybdenum Disulfide Heterostructures via Selective Area-van der Waals Epitaxy

4.1 Introduction

The emergence of 2-D atomically thin materials with novel and tunable physical properties has opened up new opportunities for design of new-generation nanoscale electronic devices [162]. Since the isolation of single layer graphene in 2004, significant effort has been dedicated to integration of novel nanostructures based on alternative 2-D materials. Among several classes of layered materials such as metal chalcogenides, boron nitride, oxides and oxychlorides, only a few have been successfully isolated in the format of 2-D mono- or multi-layers with high-crystal quality. Transition metal dichalcogenides (TMDCs) such as molybdenum disulfide (MoS_2), molybdenum diselenide ($MoSe_2$), tungsten disulfide (WS_2) are among the most studied vdW-bonded layered compounds. Based on the number of transition metal d-electrons, the TMDCs demonstrate metallic [163, 164], half-metallic magnetism [165], semiconducting [166] or superconducting characteristics [167]. For example, semiconductor compounds based on Mo and W, with their band gaps ranging from the visible to the near-infrared, have been widely studied and employed in many applications [168–170].

In particular, MoS_2 is one of the most studied 2-D TMDC materials owing to its many outstanding properties such as large carrier mobility (10 cm^2/V.s) [171]. Similar to other TMDC compounds, MoS_2 exhibits layered atomic structure with weak vdW

interaction between layers and strong intra-layer bonding. Each monolayer of MoS_2 is a tri-layer sandwich structure, which consists of hexagonal S and Mo atomic layers wherein each Mo atom resides at the center of six S atoms creating a trigonal prism. Interestingly, in its bulk form, MoS_2 displays an indirect bandgap (Eg = 1.2 eV), whereas mono-layer MoS_2 has a direct bandgap (Eg = 1.8 eV). The transition from indirect to direct bandgap from bulk to monolayer MoS_2, was predicted theoretically by Li et al. in 2007 [22]. In 2010, Splendiani et al. investigated this bandgap transition by photoluminescence (PL) of ultrathin MoS_2 layers and found that PL enhances by decreasing the number of layers. In particular, they observed that the monolayer MoS_2 shows strong peaks between 627 nm and 677 nm [172]. With these properties, MoS_2 is a great candidate for integration in devices such as field-effect transistors (FETs) [173, 174], light-emitting diodes (LEDs) [175], photodetectors [176], and photovoltaics [177].

Heterostructures and superlattices are essential building blocks of electronic and optoelectronic devices. Among the current material integration techniques, chemical epitaxy approaches such as molecular beam epitaxy (MBE) and metal organic chemical vapor deposition (MOCVD) have offered the highest-quality implementation of more complex heterostructure designs. Chemical epitaxy of two covalently bonded material systems is based on one-to-one chemical bond formation at the heterointerface. For materials with significantly dissimilar lattice structures, the heterointerface is susceptible to misfit dislocations, which could propagate and evolve into extensive threading dislocations, resulting substantial decay in intrinsic properties of the heterostructure. Thus, successful integration of heterostructures via conventional heteroepitaxy is generally reduced to materials with comparable lattice parameters (i.e., lattice constants, symmetry, thermal expansion coefficient, and polarity). The class of 2-D materials with dangling-bond-free inert surfaces provides an alternative pathway for integration of heterostructures via van der Waals epitaxy (vdWE), wherein two or more dissimilar

2-D materials can be assembled together via weak interplanar vdW interactions. Unlike conventional epitaxy, covalent strain sharing is not permitted at the heterointerface during vdWE. Thus, vdW heterostructures can be formed using a wide range of 2-D materials with dissimilar crystal structures. For example, high performance photodetectors based on various vdW heterostructures such as MoS_2/tin diselenide ($SnSe_2$) [178], MoS_2/graphene/tungsten diselenide (WSe_2)[179], and MoS_2/black phosphorus [180] have been reported. Additionally, such an integration technique is not limited to 2-D layered materials and can be applied to materials of dissimilar dimensionality to form mixed-dimensional heterostructures of radically different crystal structures. Recent research and development on mixed-dimensional vdW heterostructures as well as challenges and opportunities have been reviewed in [181, 182].

Semiconductor nanowire (NW) nanostructures provide an excellent platform for formation of complex 3-D heterostructures of dissimilar compounds in both radial and axial directions [183]. This flexibility in design of active nanostructures can provides promising solutions for design of high-performance electronic [184], optoelectronic [183], and photonic [13] devices. In additions, owning to their large surface area-to-volume ratio and small foot print on the substrate, NWs exhibit excellent strain tolerance. Therefore, III-V NWs offer outstanding potential for integration with variety of different foreign substrates such as silicon [27–29], germanium, glass [30], indium tin oxide [185], and 2-D vdW surfaces like graphene [99, 101, 103, 121, 159, 186].

In this chapter, we present for the first time lithography-free selective-area vdWE (SA-vdWE) of InAs NWs on MoS_2 micro-plates by MOCVD. The growth parameter space is mapped by altering V/III ratio, growth temperature and total flow rate of precursors. The influence of these parameters on self-assembly of vertically-aligned InAs NWs as well as growth of parasitic islands on 2-D MoS_2 surfaces is explored; growth trends are discussed independently for each set of growth trial. The impact of pre-growth surface treatment on MoS_2 is investigated toward selective-area vdWE

of a single InAs NW on each MoS_2 micro-plate. The crystal structure of InAs NWs grown under the optimal growth condition conducive to the formation single NW per MoS_2 micro-plate is analyzed. Finally, the common sub-lattice registry between vertical InAs NWs and MoS_2 flakes is discussed using a super-cell model based on the coincident alignment of NW sidewall facets and MoS_2 micro-island plate-edges. The result of this study is expected to be a basis for future investigations on integration of III-V NWs on 2-D layered materials and realization of novel mixed-dimensional vdW heterostructures with application in nano-scale optoelectronic and electronic devices.

4.2 Experimental Details

Discrete MoS_2 nanosheets were grown on 90 nm SiO_2-coated Si (100) substrate using chemical vapor deposition (CVD). Molybdenum trioxide (MoO_3) and sulfur (S) were used as precursors at furnace temperature of 700 °C. The isolated MoS_2 triangular micro-plates with side lengths ranging between ∼3 μm and 5 μm act as the growth surface in all InAs crystal growth experiments. For growth of InAs NWs, trimethyl-indium [TMIn, $(CH_3)_3In$] and arsine (AsH_3) were used as precursors for supply of group-III and group-V growth species, respectively, in an Aixtron 3×2" close-coupled showerhead metal organic chemical vapor deposition (MOCVD) reactor. For all growth runs, substrates were heated to the targeted growth temperature under a constant AsH_3 flow. Growth of NWs was initiated by introduction of TMIn flow into the chamber. After a growth duration of 300 seconds, NW growth was terminated by turning off TMIn flow. All samples were cooled under a constant AsH_3 flow.

The optimal SA-vdWE conditions were established by investigating the growth parameter space in three sets of experiments. The three sets of growth runs explored the MOCVD parameter space in the following ranges; (i) the V/III ratio was varied in the range of 5 to 250, (ii) TMIn flow rate (χ_{TMIn}) was varied between 8 to 32 μmol/min for a constant V/III ratio, (iii) the growth temperature (T_G) was varied

between 600 °C to 750 °C. For all trials, hydrogen (H_2) was used as the carrier gas with total flow of 7 L/min, and the reactor pressure was kept constant at 100 mbar. During the initial series of parameter space optimization experiments, no surface treatment was performed on MoS_2 surfaces prior to loading in the MOCVD reactor. Next, to achieve selective-area single NW synthesis per MoS_2 micro-plate, a surface treatment step was performed prior to loading, which involved dipping MoS_2 samples in a poly-l-lysine (PLL) solution for a duration of 120 seconds, followed by rinsing in deionized water for 5 seconds.

The morphology of of as-grown samples was evaluated using a Hitachi S-4000 SEM. The surface roughness of pre-treated and PLL-treated MoS_2 nano-sheets was measured using a Bruker DI-3000 atomic force microscope (AFM). The crystal structure of NWs was characterized using a FEI F20 high-resolution transmission electron microscope (HR-TEM). The TEM lamella was prepared using FEI Strata 400 STEM focused ion beam (FIB). Selected-area electron diffraction (SAED) patterns were obtained using the same instrument. Compositional analysis at the InAs/MoS_2 interface was performed through electron energy loss spectroscopy (EELS) using a Nion ultraSTEM 100 TEM.

4.3 Results and Discussions

The main objective of this study is to investigate epitaxy of a covalently bonded III-V compound system upon a 2-D vdW layered TMDC film. Here, CVD-grown discrete MoS_2 micro-plates are used as the growth surface for pseudo-vdWE of InAs NWs. A top-view optical image from a representative surface of a MoS_2 sample used for SA-vdWE experiments is shown in Figure 4.1. In the first part of this study, the MOCVD growth parameter space is mapped (i.e., V/III ratio, TG, and χ_{TMIn}) to find suitable conditions for vdWE of vertical InAs NWs on MoS_2 micro-plates. To investigate the influence of each parameter independently, one parameter is varied

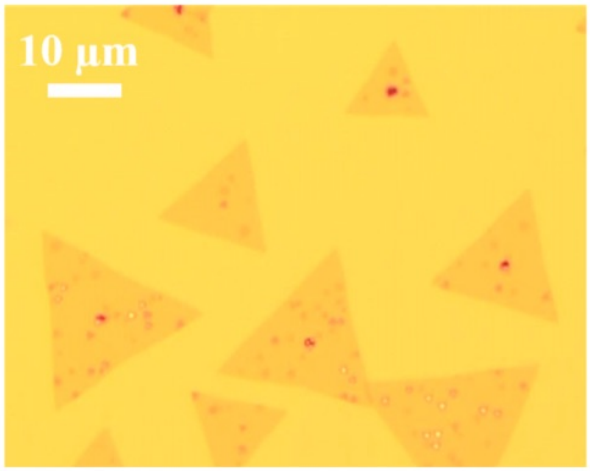

Figure 4.1: Optical image of discrete MoS_2 micro-flakes grown by CVD on SiO2/Si substrate.

in the ranges stated above while the other two parameters are kept constant. In these growth trials, similar to previously reported studies on integration of III-V NWs on vdW-surfaces, poly-crystalline parasitic islands are formed on the growth surface along with vertically-oriented NWs [99, 101, 121, 159]. To evaluate each trial run, tilted-view SEM images of 20 MoS_2 micro-plates are used to measure the mean values of NW lengths and diameters. In the second part of this study, the focus is on limiting the crystal growth to formation of a single and isolated NW per MoS_2 micro-plate, and to eliminating the formation of parasitic islands. This was achieved by focusing on the surface and plate-edge characteristics of MoS_2 micro-plates as well as further tuning of growth conditions.

In the first set of experiments, the influence of V/III ratio on formation of InAs NWs on 2D MoS_2 micro-plates is investigated. Here, the V/III ratio is changed in the range of 5 to 250 at a growth temperature of 650 °C. The V/III is modified by altering the molar flow rate of AsH_3 under a constant molar flow rate of TMIn ($\chi_{TMIn} = 16$ μmol/min). Shown in Figure 4.2(a)-(d) are 45° tilted-view SEM images of as-grown samples. For V/III = 5 [Figure 4.2(a)], the MoS_2 micro-plates are fully covered with polycrystalline InAs islands. Increasing the V/III ratio to the 25 to 125 range results

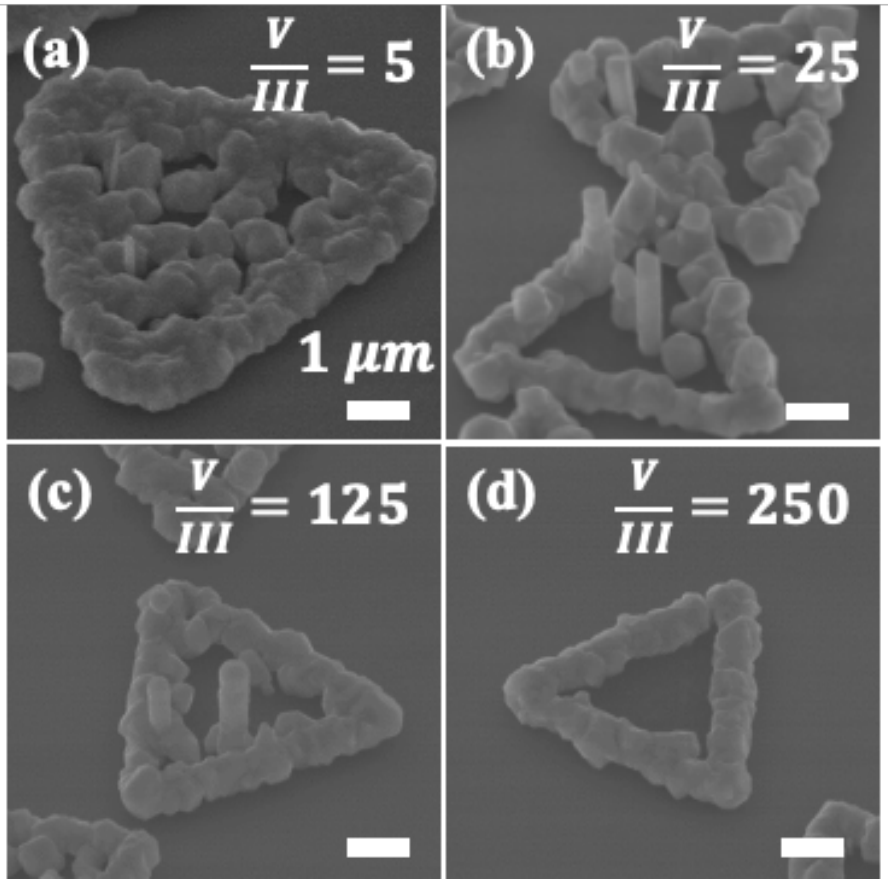

Figure 4.2: Influence of V/III ratio on pseudo-vdWE of InAs NWs on MoS_2 micro-plates. 45° tilted-view SEM images of as-grown samples at V/III ratio of (a) 5, (b) 25, (c) 125, and (d) 250, with $\chi_{TMIn} = 16$ μmol/min and $T_G = 650$ °C. All scale bars represent 1 μm.

in the formation of NWs near the center of MoS_2 flakes as well as parasitic islands around the plate-edges. For V/III ratio of 250, InAs crystal formation is limited to the edges of MoS_2 and no growth takes place along the interior area of the micro-plates.

To understand these results, it should be noted that the sticking coefficient of MoS_2 micro-plates is not homogenous throughout its surface. When adatoms impinge upon a surface, there are three possibilities: (i) to adsorb on an impingement site, (ii) to migrate on the surface and adsorb on a secondary surface site, or (c) to desorb from the surface. The sticking coefficient is defined as the ratio of the number of adsorbed atoms to the number of atoms that either migrate or desorb [187]. Here, for instance, the SiO_x surface exposed between neighboring MoS_2 microplates has a very

low sticking coefficient and no crystal growth can be observed on the oxide surface. As for the MoS_2 micro-plates, due to an abundance of available dangling bonds at the plate-edges, the sticking coefficient is greater at the plate-edge sites compared to the interior microplate surface. Under low V/III ratio growth conditions (i.e., V/III = 5), high surface migration of growth species allows for adatoms to diffuse to the central part of MoS_2 micro-plates and overcome the diffusion barrier along the plate-edges. In contrast, under high V/III ratio growth conditions (i.e., V/III = 250), crystal growth is limited to formation of parasitic islands around the edges of MoS_2 micro-plates due to low surface migration and high local sticking coefficient at the edges. For the intermediate values of V/III ratio of 25 and 125, those growth species that are able to reach the interior segment of MoS_2 micro-plates form vertical NWs. The difference in dimensions of NWs grown under V/III of 25 and 125 is negligible. While for V/III = 25, the mean NWs lengths is 1.92 μm and the mean NWs diameters is 0.40 μm, for the case of V/III = 125, the mean NWs lengths and diameters are 1.78 μm and 0.44 μm, respectively. The observed trend with respect to the influence of V/III ratio on pseudo-vdWE of InAs on 2-D MoS_2 micro-plates can be understood in terms of the fraction of growth species that can migrate across the plate-edges, where the sticking coefficient is high, and adsorb on the interior region of MoS_2 plate. Here, the surface migration of adatoms is tuned by changing the V/III ratio, and intermediate values of V/III ratio in the range of 25 to 125 represent favorable growth condition for self-assembly of vertical InAs NWs on MoS_2 surface under pseudo-vdWE regime.

Next, the effect of growth rate was studied by altering the total molar flow rate of both metal organic and hydride precursors (i.e., $\chi_{Total} = \chi_{AsH_3} + \chi_{TMIn}$) under the constant V/III ratio of 25 and growth temperature of 650 °C. To avoid any confusion, here the results are discussed with references to the molar flow rate of TMIn, χ_{TMIn}. Figure 4.3(a)–(d) illustrates the results of SA-vdWE of InAs NWs for χ_{TMIn} values in the range of 8 to 32 μmol/min. For $\chi_{TMIn} = 8$ μmol/min, the growth is limited to the

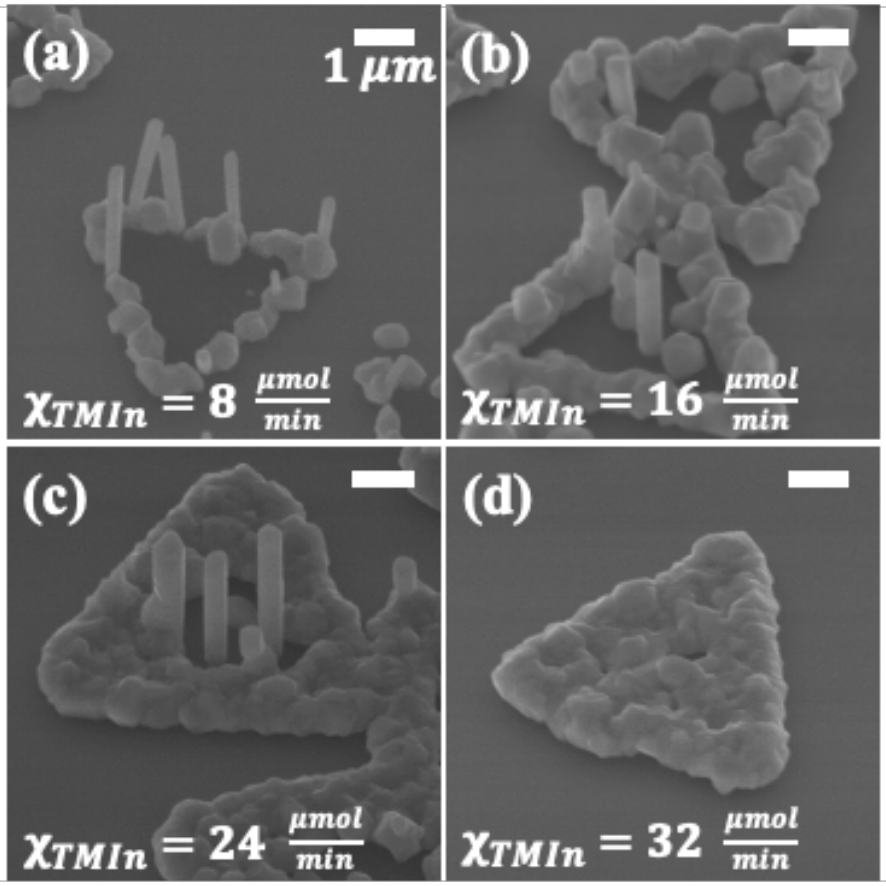

Figure 4.3: Effect of total flow rate on growth of InAs NWs on MoS_2 micro-plates via pseudo-vdWE. 45° tilted-view SEM images of as-grown samples at χ_{TMIn} of (a) 8 μmol/min, (b) 16 μmol/min, (c) 24 μmol/min, and (d) 32 μmol/min, with V/III = 25 and T_G = 650 °C. All scale bars represent 1 μm.

edges of MoS_2 micro-plates resulting in formation of NWs as well as parasitic islands, and no growth is observed along the interior region of the 2-D MoS_2. By increasing the total flow of precursors, the growth front is no longer localized to the MoS_2 edges and nucleation proceeds toward the center of the micro-plates. Under the intermediate total flow rate range (i.e., χ_{TMIn} = 16 μmol/min to 24 μmol/min), the formation of NWs is predominantly observed at the central area of the MoS_2 micro-plates, while parasitic islands are observed to form around the plate-edges. In the case of χ_{TMIn} = 32 μmol/min, the MoS_2 surface is fully coated with a continuous poly-crystalline film of InAs formed by coalescence of parasitic islands.

In the specific case of χ_{TMIn} = 8 μmol/min, NWs with mean lengths and diameters

of ∼2.30 μm and ∼0.26 μm, respectively, are formed around the edge of MoS_2 micro-plates. Increasing the flow rates to χ_{TMIn} = 16 μmol/min leads to growth of NWs with mean lengths of ∼1.92 μm and the mean diameter of ∼0.40 μm. While under high-flow condition of χ_{TMIn} = 24 μmol/min, the coverage of parasitic islands on MoS_2 micro-plates increases, the mean length of NWs reduces to ∼1.64 μm and the mean of NWs diameter increases to ∼0.54 μm. The trend in influence of total flow rate on pseudo-vdWE of InAs NWs on 2-D MoS_2 suggests that by increasing precursors supply, the growth front moves from edge of MoS_2 micro-plates toward the central region. Meanwhile, the aspect ratio of NWs reduces due to role of parasitic islands as the predominant atomic sink.

Next, the effect of growth temperature on the formation of InAs NWs on MoS_2 micro-plates under pseudo-vdWE regime is investigated. In this trial, T_G values of 600 °C, 650 °C, and 700 °C are tested under constant V/III ratio of 25 and χ_{TMIn} = 16 μmol/min. The result of this trial is summarized in Figure 4.43(a)-(c) via tilted-view SEM images labeled with the corresponding growth temperature. As it can be seen in Figure 4.4(a), at T_G = 600 °C, the formation of NWs is fully quenched. As seen in Figure 4.4(b) and 3(c), at the elevated growth temperature (T_G = 650 °C and T_G = 700 °C), vertical InAs NWs are self-assembled on MoS_2 micro-plates along with

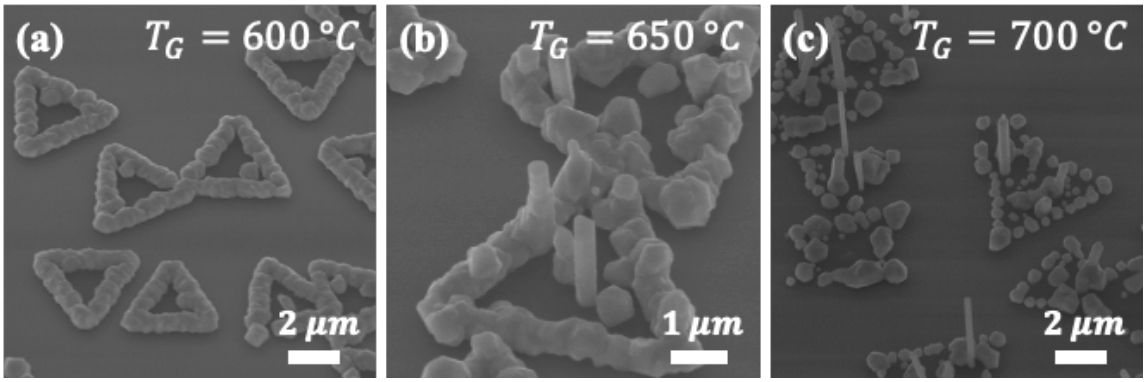

Figure 4.4: Influence of growth temperature on self-assembly of InAs NWs on MoS_2 micro-plates via pseudo-vdWE. 45° tilted-view SEM images of as-grown samples at T_G of (a) 600 °C, (b) 650 °C, and (c) 700 °C, with V/III = 25 and χ_{TMIn} = 16 μmol/min.

parasitic islands forming on the center and edges of the micro-plates. For the case of TG = 650 °C, the mean NW height and diameter are measured to be 2 μm and 0.35 μm, respectively. By increasing the growth temperature to T_G = 700 °C, the mean NW length and diameter are increased to 2.35 μm and 0.43 μm, respectively.

In the low temperature range (i.e., T_G = 650 °C and below), parasitic islands are mainly formed around the edges of MoS_2 micro-plates and few islands are seen beyond the edges. This observation can be understood in terms of temperature-dependent surface mobility of group-III species and the abundance in availability of dangling bonds at the edges of MoS_2 micro-plates. The edges of MoS_2 micro-plates act as favorable nucleation sites for growth species with low surface mobility, where adjacent parasitic islands merge and form a ring-shape contiguous film around the MoS_2 micro-plates. By increasing T_G, and as a result of enhancement in the surface mobility of adatoms, the growth species have overcome the barrier at the edges and travel onto the interior region of the MoS_2 micro-plates. It is noted that the density of parasitic islands changes dramatically by further increase in T_G to 700 °C. This can be attributed to preferential incorporation of diffusive growth species into NWs instead of parasitic islands.

The above trend in influence of growth condition on formation of NWs and areal density of parasitic islands is used as a survey in realization of SA-vdWE of vertical InAs NWs on MoS_2 micro-plates. In summary, V/III = 25, χ_{TMIn} = 16 μmol/min and T_G = 650 °C allows for formation of NWs along the interior surface of MoS_2 micro-plates and, simultaneously, extensive growth of parasitic islands around the edges of MoS_2 micro-plates. On the other hand, keeping the V/III ratio and T_G constant and reducing χ_{TMIn} to 8 μmol/min results in further reduction in formation of parasitic islands due to decrease in availability of precursors at the low group-III precursor flow rate. The results of T_G-dependent growth experiment suggests that elevated temperatures are conducive to the formation of NWs and minimum coverage

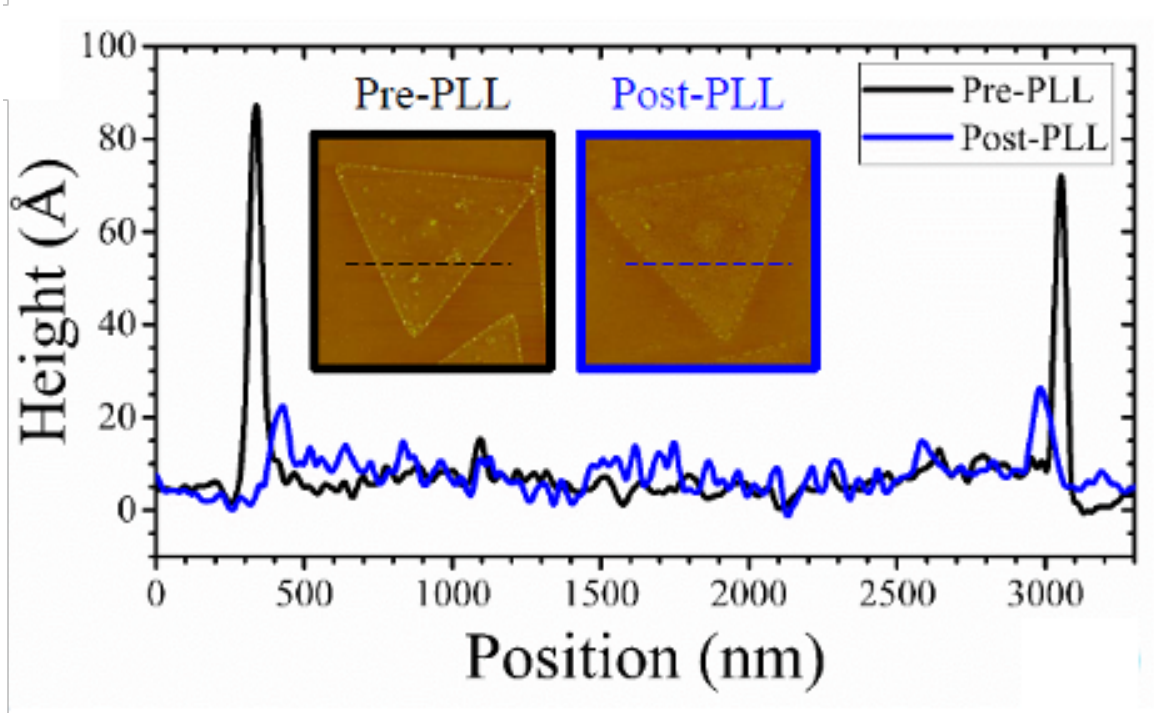

Figure 4.5: Comparison of height profile on MoS_2 micro-plates surfaces pre- and post-PLL treatment. The height profile was measured via AFM.

of parasitic islands at the edges of MoS_2, which is a necessary criterion for realization of single NW per MoS_2 micro-plate. Thus, the growth conditions of V/III = 25, χ_{TMIn} = 8 μmol/min and T_G = 750 °C were selected as optimal SA-vdWE condition for InAs NWs on MoS_2 micro-plates.

Next, the influence of a pre-growth PPL surface treatment is investigated. The effect of PLL as a coating reagent for changing the surface charge was reported by Umehara et al. [188]. Here, PLL is used for charge compensation of dangling bonds at the edges of MoS_2 micro-plates. Accordingly, the diffusion barrier at the MoS_2 plate-edges is expected to be affected by passivating the available dangling bonds at those regions. Furthermore, the surface roughness of individual micro-plates is investigated via AFM measurements of pre- and post-PLL treated MoS_2 samples. Figure 4.5 shows the height profile of a MoS_2 micro-plate before and after the PLL treatment, where a pre-PLL treatment height profile is shown in a solid black line and a post-PLL treatment height profile is plotted in a solid blue line. This comparison

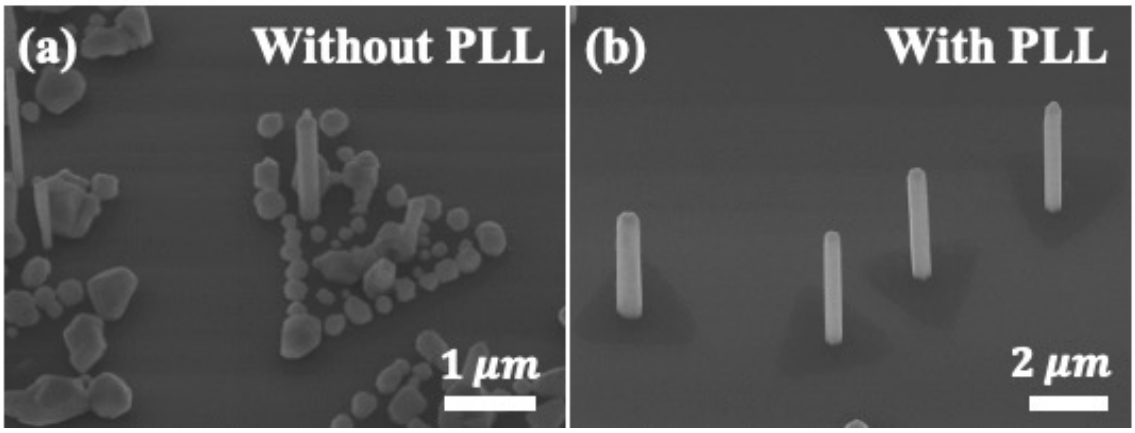

Figure 4.6: Pseudo-vdWE of InAs NWs on MoS_2 micro-plates under V/III = 25, χ_{TMIn} = 8 μmol/min and T_G = 750 °C. As-grown samples using MoS_2 micro-plates (a) without, (b) with PLL treatment.

indicates that the PLL surface treatment reduces the step height at the MoS_2 plate-edge from ∼90 Å(pre-PLL treatment) to ∼25 Å(post-PLL treatment). This height difference can likely be due to dissolution of MoO_3 during the surface treatment (i.e., due to PLL treatment and DI water rinse). Representative AFM images of the sample pre- and post-PLL treatment samples are shown as insets in Figure 4.5, highlighted with black and blue borders, respectively. The particles seen on the surface and edges of MoS_2 micro-plates are significantly reduced after the PLL-treatment. Presence of these particles are reported in various studies and is likely to be un-reacted MoO_3 [174] [189].

In the second part of this study, the results of optimized growth parameter space and influence of PLL surface treatment are used for integration of single InAs NW on individual isolated MoS_2 micro-plates. To this end, samples with and without PLL treatment were loaded for growth under the previously determined optimal SA-vdWE conditions (i.e., V/III = 25, χ_{TMIn} = 8 μmol/min, and T_G = 750 °C). Tilted-view SEM images of as-grown samples on MoS_2 micro-plates without and with PLL treatment are shown in Figure 4.6(a) and (b), respectively. As expected, using untreated MoS_2 as growth surface under the stated MOCVD conditions results in formation of NWs

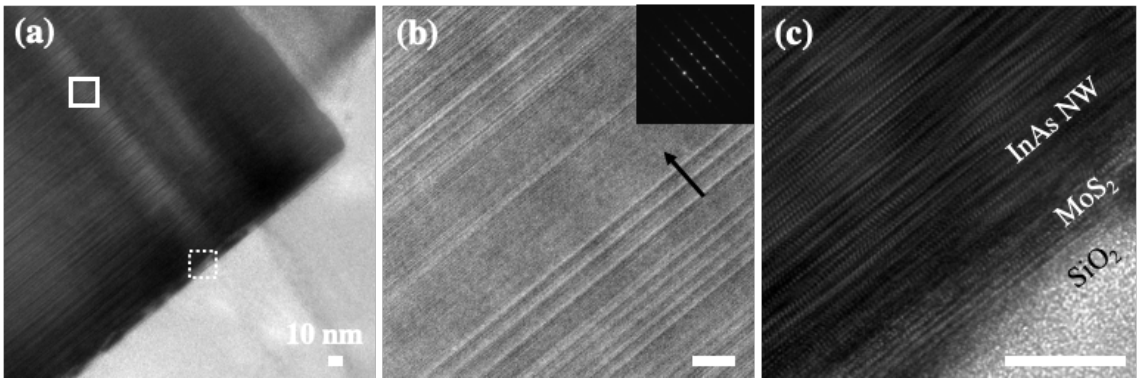

Figure 4.7: (a-c) HR-TEM images of InAs NW grown under V/III = 25, χ_{TMIn} = 8 μmol/min and T_G = 750 °C. Panel (b) and (c) show higher magnification of highlighted region in white border and black border in panel (a), respectively. SAED pattern shown as an inset of panel (b) confirms the polytypic crystal phases in the InAs NW.

as well as parasitic islands. Since this growth is performed under elevated growth temperature, high surface mobility of growth-III species as well as high desorption of group-V species lead to formation of discrete parasitic islands (unlike continuous poly-crystalline film of InAs formed under lower T_G of 700 °C). Under the same growth conditions, SA-vdWE of InAs NWs is achieved on the PLL-treated MoS_2 surface. As noted earlier, PLL likely changes the MoS_2 surface in two ways: (i) it allows charge compensation of dangling bonds available at the edges of MoS_2 micro-plates, thereby quenching sites for the formation of parasitic islands; and (ii) it allows for the dissolution of the residual particles and consequent smoothening of the MoS_2 surface, which minimizes the availability of atomic sinks for nucleation and formation of more than one NW or parasitic islands per MoS_2 micro-plate.

To investigate the crystal structure of NWs and to probe the InAs/MoS_2 interface, a TEM lamella is prepared from a NW grown under SA-vdWE condition using FIB. Figure 4.7 shows HR-TEM images of the NW acquired along the $<\bar{1}10>_{ZB}$ zone axis of the cubic phase. The base of the NW is shown in Figure 4.7(a), the NW growth direction along $<\overline{111}>_{ZB}$ is indicated with black arrow in Figure 4.7(b). The approximate locations of the HR-TEM images shown in Figure 4.7(b) and (c) is illustrated on Figure 4.7(a) using solid white and dotted white borders. Firstly, it is

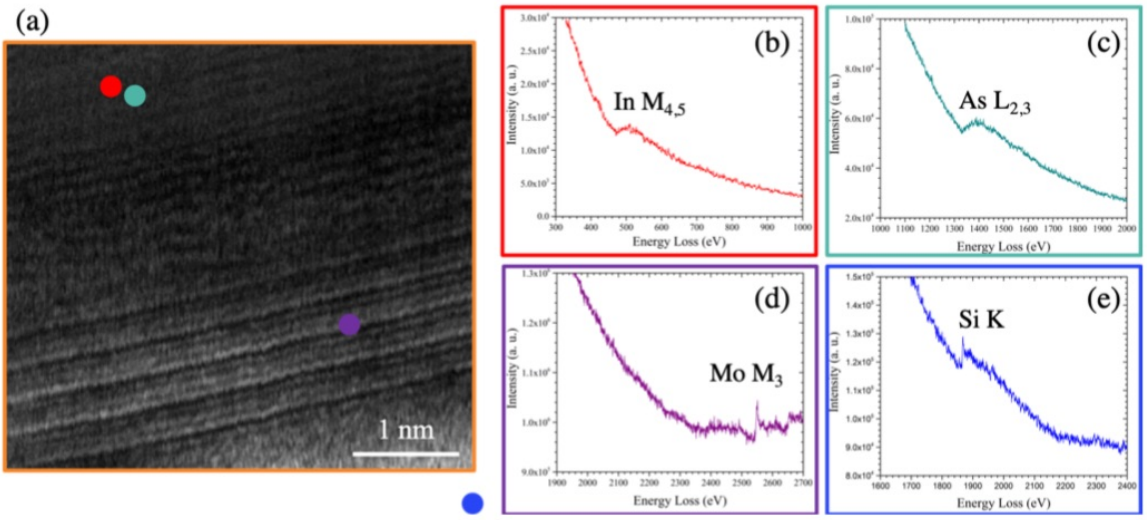

Figure 4.8: (a) HR-TEM from the hetero-interface of InAs and MoS_2, EELS spectrum for (b) In, (c) As, (d) Mo, and (e) Si detected on the locations shown on the panel (a).

noted that under the SA-vdWE conditions (i.e., V/III = 25, $\chi_{TMIn} = 8$ μmol/min and $T_G = 750$ °C), the crystal structure through the length of the NW consist of zinc-blend (ZB), wurtzite (WZ), and 4H polytype phases. This characteristic disordered crystal structure along with high density of stacking faults and rotational twin planes was also observed for InAs NWs grown on graphene under vdWE mode [103], [101] as well as for InAs NWs grown via SAE mode on Si substrates [127, 145, 158]. The SAED pattern, shown as the inset of Figure 4.7(b), exhibits streaking along the $<\overline{111}>_{ZB}$ axis, which confirms the polytypical crystal phase of the InAs lattice. Next, the interface of InAs NW and MoS_2 micro-plate is shown in high-magnification micrograph (figure 4.7(c)). Here, at the location of NW growth, a total of five vdW-bonded layers of MoS_2 are observed in the micro-plate. Despite the large NW diameter (i.e., >300 nm), misfit dislocations are not found at the InAs/MoS_2 hetero-interface and the NW lattice is free of threading dislocations, likely due to the absence of strain sharing between the dissimilar lattices.

Using the same TEM grid, the hetero-interface of the MoS_2 and InAs was explored using the NION ultraSTEM 100 with electron energy loss spectroscopy (EELS)

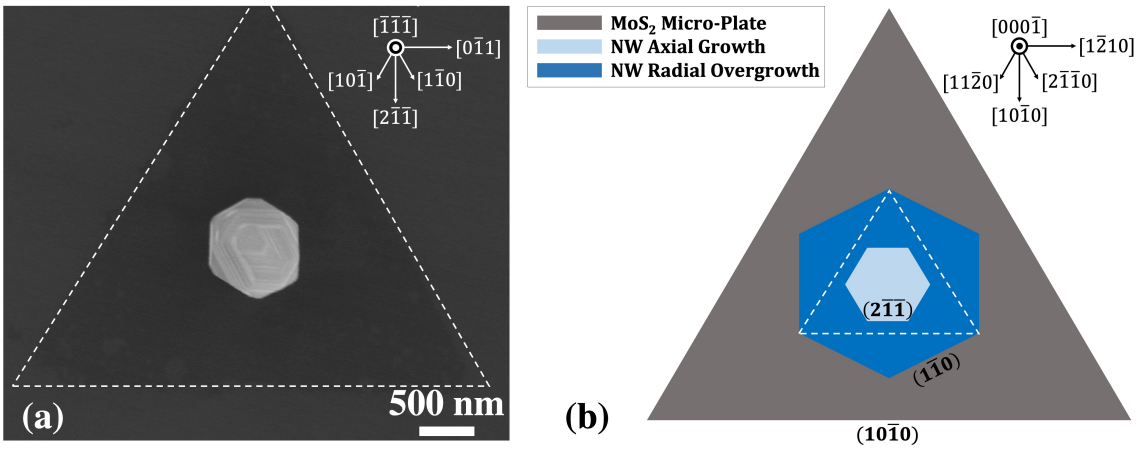

Figure 4.9: (a) Top view SEM image of single InAs NW on a MoS_2 micro-plate, (b) the schematic of NW core-segment and radial over-growth, and orientation of their sidewall facets relative to MoS_2 plate-edges.

capability at CCMR facility. Shown in Figure 4.8(a) is the HR-TEM image of multilayer MoS_2 and InAs NW base. The locations of scans to obtain EELS signals are shown on the this figure with dots. Figure 4.8(b), (c), (d), and (e) shows EELS spectra and peaks for In, As, Mo and Si, respectively. Here, five layers of MoS_2 can be counted. In the process of synthesis of MoS_2 flakes via CVD, the high concentration of MoO_{3-x} and S vapor precursors motivates the self-seeding nucleation mechanism, resulting in formation of a central particle-type feature with a multilayer MoS_2 structure [190]. In contrast, by lowering the concentration of reactants in the CVD chamber, the 2-D planar nucleation mechanism leads to production of monolayer or bilayer MoS_2 [190].

Next, the lattice alignment and in-plane orientation of InAs NWs relative to MoS_2 micro-plates are considered. Figure 4.9(a) shows a plan-view SEM image of a representative InAs NW grown under the optimized SA-vdWE conditions on a triangular MoS_2 micro-plate, where the sides of the latter are outlined by white dashed lines. The hexagonally cross-sectioned NW is situated near the center of the micro-plate. From the plan-view SEM image, two separate sets of NW sidewall facets (i.e., two families of sidewall planes) can be observed. The sidewall planes can be indexed with reference to SAED pattern analysis from TEM characterization. The

interior facets of the NW are principally $\{2\bar{1}\bar{1}\}$-oriented, and three of six visible interior facets are aligned with parallel orientation relative to the three $\{10\bar{1}0\}$-oriented sides of the MoS_2 micro-plate. The exterior NW sidewall facets, however, appear to be rotated 30° relative to the interior facets. Therefore, the exterior facets of the NW are principally $\{1\bar{1}0\}$-oriented. Accordingly, the legend at the top-right corner of Figure 4.9(a) indicates the corresponding directions along the cubic InAs lattice. The apparent rotation of the planar sidewall structure can likely be attributed to the evolution of radially-overgrown shell layers upon an axially-grown NW core segment. This stems from preferential adatom nucleation along NW sidewalls, initiated at the low-energy vertices of hexagonal core segment, primarily due the relative lack of nucleation sites on the vdW-surface. Preferential nucleation of adatoms on NW sidewalls leading to modulation of the faceting structure from the $\{2\bar{1}\bar{1}\}$-orientation (i.e., central core segement) to the $\{1\bar{1}0\}$-orientation (i.e., external shell segment) has been previously reported for III-V NWs synthesized under different growth modes.

A plan-view diagrammatical representation of the in-plane orientation of the axially-grown NW core segment (light blue, interior hexagon) and radially-overgrown NW shell segment (dark blue, exterior hexagon) relative to the triangular MoS_2 micro-flake (gray triangle) is shown in Figure 4.9(b). The legend at the top-right corner of Figure 4.9(b) indicates crystallographic directions corresponding to the hexagonal MoS_2 lattice. The representative planar indices of the interior and exterior NW sidewall facets and the exterior MoS_2 plate-edge facets are labelled. As a guide to the eye, the white dashed triangular border depicts the coincident sidewall orientations of the NW core segment and the MoS_2 micro-flake. Since the NW core segment with $\{2\bar{1}\bar{1}\}$-orientated sidewall facets is formed directly on the MoS_2 surface, the epitaxial relationship, which guides the formation of vertically-oriented freestanding NWs during SA-vdWE, can be understood in terms of their coincident in-plane alignment of these two components.

Based on the above observed symmetrical orientation and coherent alignment

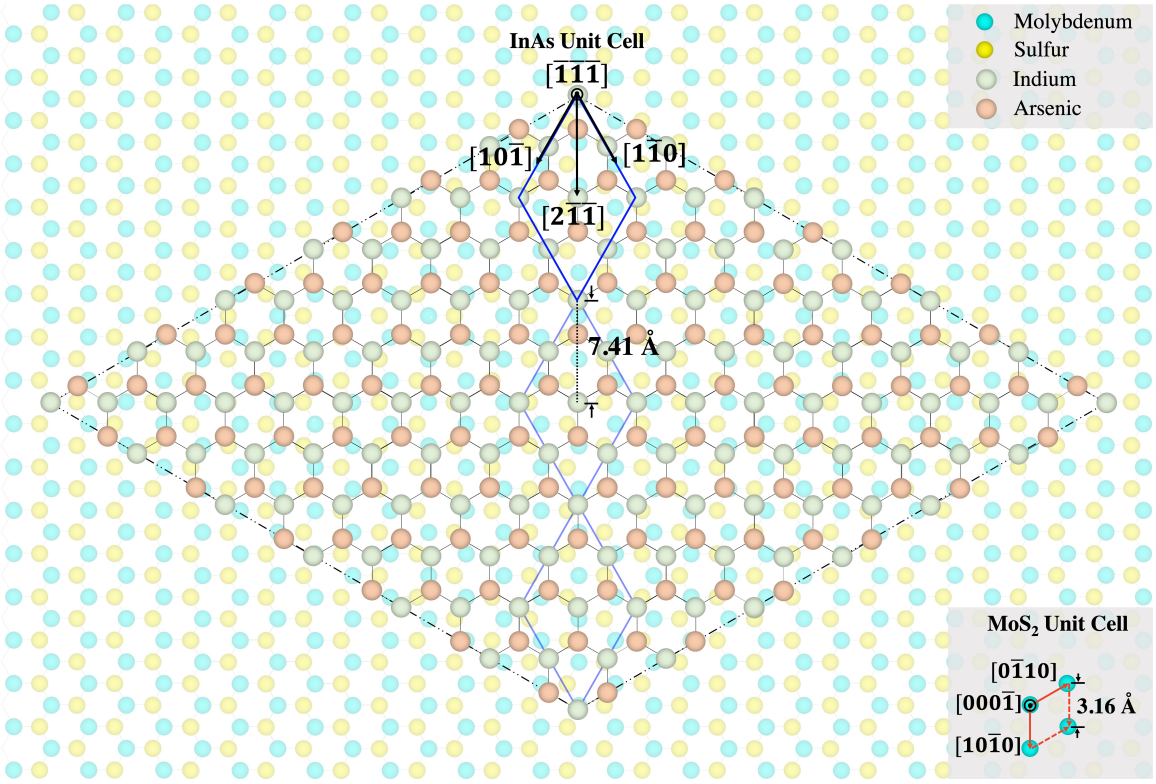

Figure 4.10: Atomic arrangement of cubic InAs and hexagonal MoS_2 lattices. The InAs (111) unit cell is highlighted as a reference along with hexagonal MoS_2 (000$\bar{1}$) unit cell. The legend shows Mo-, S-, In-, and As-atoms illustrated in blue, yellow, grey and orange, respectively.

between the NW and 2D micro-plate, a model for a nearly-commensurate super-cell lattice configuration for <111>-oriented InAs NWs on MoS_2 is proposed. Figure 4.10 depicts the relative atomic arrangement of InAs and MoS_2 compounds on equivalent ($\bar{1}\bar{1}\bar{1}$)- and (000$\bar{1}$)-oriented surfaces, where Mo-, S-, In-, and As-atoms are shown in blue, yellow, gray, and orange, respectively. The cubic 2×2 InAs unit cell is shown as a reference (i.e., rhombus highlighted with blue borders), along with the hexagonal MoS_2 (000$\bar{1}$) unit cell. As indicated in Figure 4.10, a common sub-lattice is formed such that a distance equal to three multiples of the cubic InAs unit cell along the [2$\bar{1}\bar{1}$] direction is nearly commensurate with a 14-fold multiple of the Mo-Mo (or S-S) spacing along the [10$\bar{1}$0] direction of hexagonal lattice. The proposed lattice registry is in agreement with the observations based on the top-view SEM image shown in

Figure 4.9, where the sidewall facets of the InAs core segment are parallel to the MoS_2 micro-flake facets.

4.4 Conclusions

In summary, SA-vdWE of vertically aligned InAs NW arrays on MoS_2 micro-plate via MOCVD has been reported. The growth parameter space is explored for optimizing positioning of single InAs NWs on discrete MoS_2 micro-plates with one-to-one NW-to-MoS_2 placement. The influence of pre-growth surface treatment is examined using PLL and DI water. The SA-vdWE growth condition is achieved for V/III = 25, T_G = 750 °C, and χ_{TMIn} = 8 μmol/min on PLL-treated MoS_2 micro-plates. The NWs grown under mentioned condition exhibit polytypic crystal phases, similar to the case of vdWE of InAs on graphitic surfaces. The sidewall faceting modulation during radial growth of NWs is observed using top view SEM images. It is shown that the sidewalls of the NWs core-segment are predominately {112}-oriented and in parallel with MoS_2 plate-edges. Finally, a nearly commensurate atomic arrangement of cubic InAs on hexagonal MoS_2 lattices is suggested, wherein one-half of the cubic InAs unit cell along the $[\overline{1}\overline{1}2]$ direction is approximately equal with a seven-fold multiple of the Mo-Mo (or S-S) spacing along the $[10\overline{1}0]$ direction of MoS_2 hexagonal lattice. This work offers a guide for integration of mixed-dimensional nanosystems based on vertically aligned III-V NWs on 2-D materials via SA-vdWE. Such a nano-hybrid system can be used as a basis for design of novel architectures for nanoelectronic and optoelectronic devices.

Chapter 5

Selective-Area Epitaxy of GaAsP Nanowire Arrays on Silicon for Tandem Junction Photovoltaic Solar Cells

5.1 Motivations

To date, the terrestrial PV market is dominated by crystalline Si SCs with record efficiency of 26.7% reaching the detailed balance limit for such a structure [9]. Planar III-V MJSCs with significantly higher efficiency of 38.8% could overcome the limitation of Si single-junction PV modules [191]. Due to their high fabrication cost, primarily because of III-V substrates and materials share of cost, planar III-V multijunction solar cells (MJSCs) technology is primarily attractive for space and concentrator PV applications. The tandem configuration of high-efficiency III-V MJSC cell on a cost efficient Si cell/substrate has been an attractive path toward the $/W reduction. There are two main techniques for realizing planar III-V-on-Si configurations; (1) mechanical stacking and (2) monolithic heteroepitaxy integration. In a joint study between NREL, CSEM and EFPF, mechanically stacked III-V sub-cells on Si was reported, where a double junction GaAs/Si with 32.8% and triple junction GaInP/GaAs/Si SCs with 35.9% efficiency was illustrated [192]. In these modules, a transparent adhesive material is used to mechanically stack the subcells. One of the challenges with mechanical stacking is that pre-growth bonded heterointerface can potentially suffer from the thermal coefficient mismatch between the layers leading to cracks or bowing in the layers. On the other hand, the option of post-growth bonding has its

own challenges such as the need for a sacrificial substrate and extra fabrication cost of two separate cells. Direct heteroepitaxially grown III-V compounds on Si is another approach that is promising for low cost and efficient cells [193]. The main challenges for this approach are (1) lattice mismatch criteria and thermal coefficient difference, (2) formation of antiphase domain defects due to growth of polar III-Vs on non-polar Si, (3) limitation in design of buffer layers. These topics are described in details in section 5.2.

In contrast, in heteroepitaxy of III-V NWs on Si, the induced strain at the heterointerface due to lattice mismatch can be relaxed through the NW sidewall surfaces. In this sense, NWs provide a platform for assembly of highly-crystalline III-V active cells on Si acting as either a growth surface or an active sub-cell [33]. In addition, compared to bulk III-V structures, NW nanostructures permit lowering the fabrication cost by substantial reduction in material usage. These facts combined by the already discussed advantages of NWs-based SCs in Chapter 1 are the main motivations for the research presented here.

5.2 Introduction

A novel architecture for multi-junction bifacial III-V-NWs-on-Si SC is proposed in section 5.2. The basic idea behind MJSCs is to be able to selectively absorb photons within a wide energy range. In MJSCs, the sequence of sub-cells is engineering in a way that photons with greatest (least) energy can be absorbed in the top (bottom) cell. De Vos calculated the detailed balance limit for tandem cells with n number of junctions and found 49% efficiency for an ideal three-junctions cell [10]. With Si (1.1 eV) as middle cell and bifacial growth substrate, a possible selection of III-V compounds for the other two sub-cells are $GaAs_{0.73}P_{0.27}$ (1.75 eV) and $InAs_{0.84}P_{0.16}$ (0.5 eV). Calculations show that such a stack of III-V/Si/III-V MJSC structure can reach to efficiency of 48% under one sun AM1.5G spectrum [10].

The schematic of the proposed III-V on Si MJSC is shown in Figure 5.1 (a). This design takes advantage of the two III-V NW array sub-cells on Si SC structures discussed in sections 5.2 and 5.2. This MJSC design is based on the SQ detailed balance efficiency calculation, shown in 5.1 (b), for a fixed middle cell with E_g of 1.12 eV where the maximum efficiency calculated for the triple junction device is 48% for a one sun AM1.5G spectrum. Based on this calculation, the maximum efficiency for such MJSC design can be achieved by adding a top cell with 1.75 eV bandgap ($GaAs_{0.73}P_{0.27}$) and a rear sub-cell with 0.5 eV bandgap ($InAs_{0.80}0P_{0.20}$). Fedorenko et al. performed a theoretical study to maximize the absorption and optimize the current matching between the three sub-cells by finding the suitable NWs diameter and spacing for the propsed MJSC design [194]. This work is summarized in this section. In this study, the Diffract MOD simulation engine of Synopsys TCAD RSoft software was used employing the Rigorous coupled wave analysis (RCWA) technique for calculating absorption in NW arrays. A typical single-crystalline Si solar cell thickness of 200 μm was used to find the absorption in the middle Si cell and the current matching optimization.

To optimize the top cell geometry, the J_{sc} for different diameter and pitch of

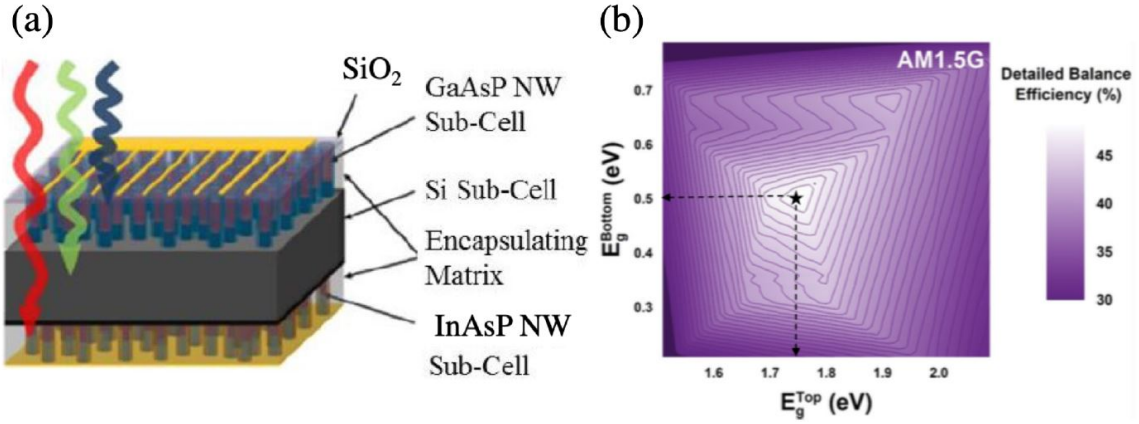

Figure 5.1: (a) Schematic of the proposed triple junction SC showing the top, middle and bottom sub-cells. (b) SQ detailed balance plot calculated for a triple MJSC with $GaAs_{0.73}P_{0.27}$ (1.75 eV) top cell, Si (1.1 eV) middle cell, and $InAs_{0.84}P_{0.16}$ (0.5 eV) bottom cell for AM1.5G spectrum [10].

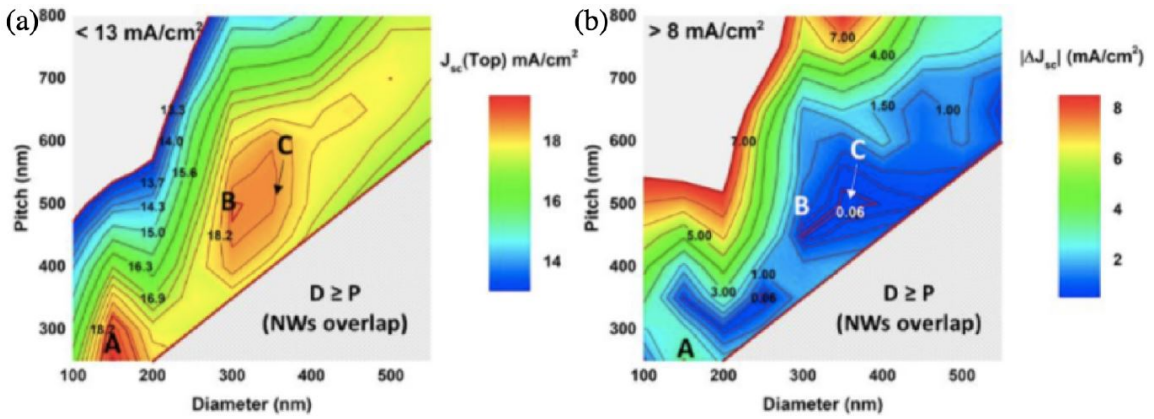

Figure 5.2: (a) J_{sc} of GaAsP NW arrays as a funciton of NWs diameter and center-to-center pitch for AM1.5G spectrum. The difference between the J_{sc} values of the GaAsP (top) and Si (middle) cells as a function of top cell geometry [194].

GaAsP NWs for AM1.5G spectrum is calculated and illustrated as Figure 5.2(a) [194]. This calculation shows two local maxima for top cell J_{sc} at D_A =150 nm, P_A =250 nm and D_B = 300 nm, P_B = 500 nm. To pick the best values for D and P, it is essential to map the difference between the Jsc values of the top and middle cell assuming that all absorbed flux is converted into electrical current. As it can be seen in Figure 5.2(b) [194], interestingly, although a maximum J_{sc} of 19.65 mA/cm^2 can be extracted from a top cell with arrangement A, the best current matching between top and middle cells can be achieved by configuration C with D_C = 350 nm and P_C = 500 nm with J_{sc} difference of 0.01 mA/cm^2.

Self-Assembly of InAsP Nanowire Array on Silicon Substrate

Growth and composition tuning of $InAs_yP_{1-y}$ NWs on SLG nanosheets were presented in section 3.3.2. With the similar growth recipe, self-assembly of high density vertical array of InAsP NWs on Si was developed. The growth of InAsP NWs is performed in an Aixtron 3×2" close coupled showerhead MOCVD reactor. Figure 5.3 (a), exhibits a half 2" Si (111) wafer after direct epitaxy of InAsP NWs. Prior to loading the sample in the reactor, the native oxide on the Si wafer was removed by submerging the sample in a BOE 10:1 solution. Next, poly-l-lysine (PLL) was deposited on the sample surface. After two minutes, the sample was dipped in DI water and was loaded into the reactor shortly after. Cross-sectional SEM image from the same sample is shown in Figure 5.3 (b). The average length of NWs was measured to be 18 μm (Figure 5.3 (c) and (d)).

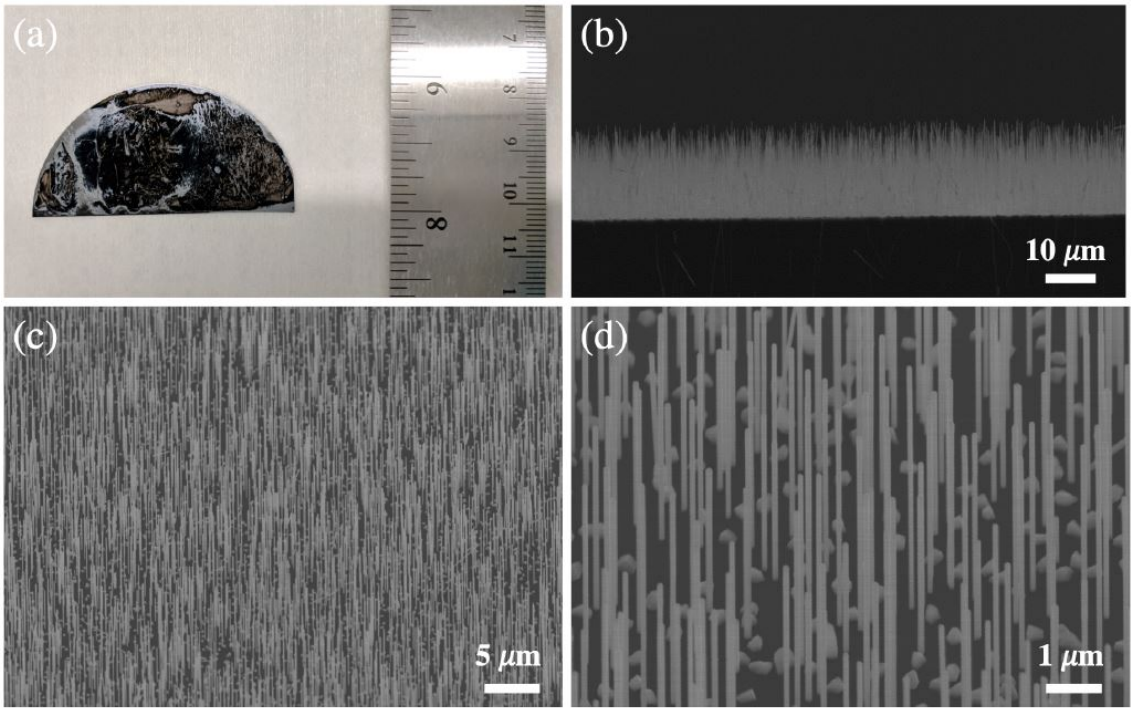

Figure 5.3: (a) Self-assembly of InAsP NWs on Si(111) wafer. The black regions on the sample are the dense arrays of NWs with average height of 18 μm shown in (b) cross-sesctional, (c) and (d) tilted view SEM images.

Selective Area Epitaxy of GaAsP Nanowire Array on Silicon Substrate

Heteroepitaxy of GaAsP NWs on Si(111) was demonstrated via self-catalyzed VLS technique using MBE [195, 196] and MOCVD [142]. In contrast, SAE of this ternary III-V compound on Si substrate was reported only by Fujisawa et al. [197]. For integration of GaAsP NWs via SAE, the first step is to define nanopore openings in the SiO_2 template on Si (111) substrate.

Here, SAE of GaAsP NWs was studied for different sizes and densities of nanopore in order to achieve epitaxy of large area NW arrays with uniform diameters and lengths. In addition, the effect of size and separation of patterned atomic sink regions surrounding NW arrays was studied. In this study, four different patterning techniques, nano-sphere lithography (NSL), photolithography, electron beam lithography (EBL) and Talbot displacement lithography (TDL) have been used. The cost-effective NSL samples were used in three set of experiments including, (i) the growth parameter space optimization and (ii) composition tuning. However, the lack of uniformity and repeatability in these samples motivated us to use photolithography, EBL and TDL techniques to pattern samples in subsequent growth experiments. Results for each set of experiments are discussed in this section.

5.3 Selective Area Epitaxy Using Nanosphere Lithography

5.3.1 Experimental Details

Nanosphere lithography (NSL) is a type of patterning technique with low fabrication cost compared to other types of lithography methods such as photolithography, nanoimprint and electron beam lithography. In this patterning method, no fix hard mask or mold is needed. However, tunability of this method is very limited. Meaning, diameter, spacing and in general the pattern shape is restricted.

Here the implemented NSL process flow is explained using the schematic diagram shown in Figure 5.1. First, a 170 nm SiO_2 layer was deposited on a Si (111) substrate using P5000 PECVD, following by annealing under N_2 flow at 600 °C in the Bruce furnace (not shown in the schematic). Next, 200 nm-diameter nanospheres were deposited on the SiO_2/Si surface. Using reactive ion etch (RIE) with O_2 plasma, the radius of the nanospheres was reduced to the targeted size. Nanosphere size can be tuned by power, partial pressure of chamber and RIE time. At this step, a 12 nm aluminum (Al) film was deposited on the sample by e-beam evaporation delete system.

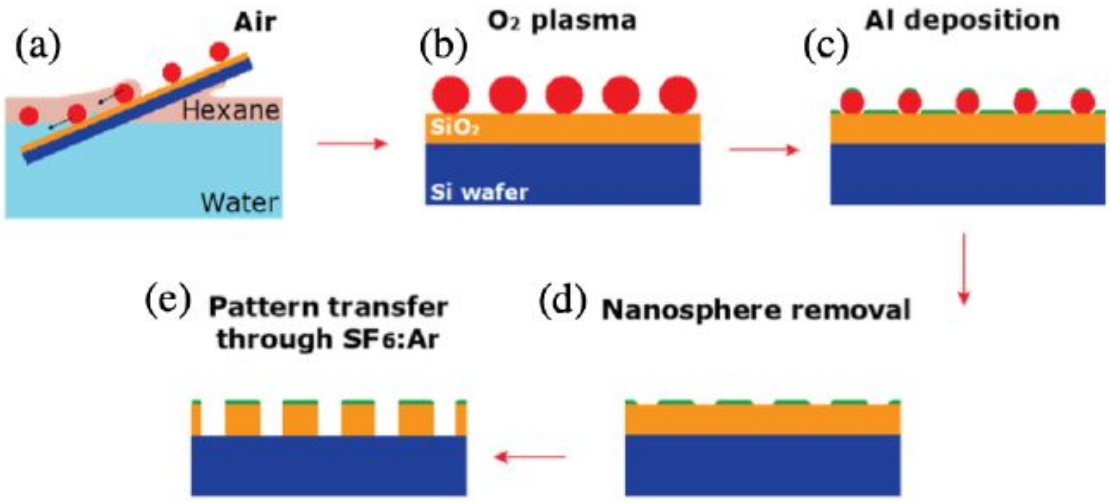

Figure 5.4: Fabrication steps for patterning by NSL, (a) nanosphere deposition, (b) reducing the nanospheres radius by O_2 plasma, (c) deposition of Al-film, (d) removal of nanospheres in toluene sonication bath, (e) RIE to transfer the pattern to the SiO_2 template.

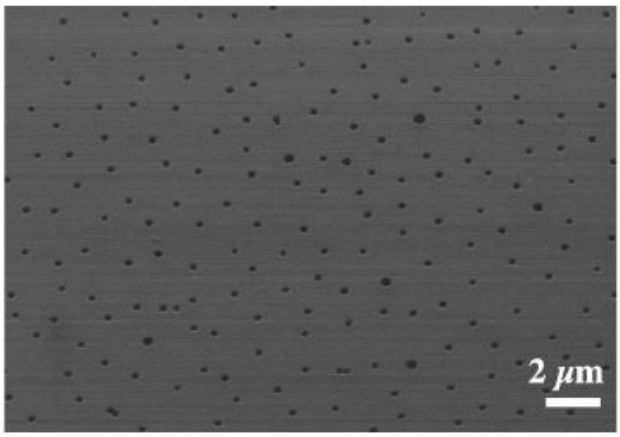

Figure 5.5: A 45° tilted view SEM image showing a random array of pores with D = 100 - 200 nm defined in SiO_2 by NSL technique.

This step was followed by removal of nanospheres in a toluene sonication bath. Next, nanosphere patterns were transferred in the silicon film by RIE, leaving behind a 20 nm-thick oxide film inside inside the pores. It should be noted here that the last step designed and optimized in a way that the 20 nm oxide keeps the Si surface undamaged during the dry etch step. This oxide layer is removed prior to loading of the sample into the MOCVD reactor. In the last step, the Al film is completely removed leaving no residue behind.

Shown in Figure 5.2 is a 45° tilted view SEM image of a random array of pores with diameters in range of 100-200 nm defined in the SiO_2 layer. It is worth mentioning here that generally NSL is not conducive to fabricaiton of an ordered array of patterns with specific pore diameters. However, the average diameter and spacing of patterns can be controlled to some extent by the initial nanosphere size and the RIE conditions.

5.3.2 Results and Discussions

Growth of NWs was performed in an Aixtron 3×2" close coupled showerhead MOCVD reactor. Trimethyl-gallium (TMGa, $(CH_3)_3Ga$), arsine (AsH_3), and phosphine (PH_3) were used as precursors for supply of Ga, As, and P growth species, respectively. During all growth runs, hydrogen (H_2) was used as the carrier gas with total flow of 14 L/min, and the reactor pressure was kept constant at 50 mbar. The NSL-patterned SiO_2 film on Si (111) substrate was used as the growth surface. As it was discussed in Chapter 2, in SAE for nucleation to be initiated, the growth surface should be exposed and free of native oxide layers. Thus, prior to loading the sample in the MOCVD reactor, the Si native oxide layer was removed in a 10:1 BOE solution. Then, samples were heated to 1000 °C and kept at this elevated temperature for a 10 min desorption step under a constant flow of group-V precursors. This was followed by adjustment in the growth surface temperature to T_G = 950 °C. At this point, flow of AsH_3 and PH_3 were set to growth values of 406 μmol/min and 487 μmol/min, respectively. The growth of NWs was initiated by introduction of TMGa flow into the reactor for the V/III ratio value of 500. After a growth duration of t_G = 40 min, heteroepitaxy of GaAsP NWs was terminating by stopping TMGa flow. Lastly, to avoid desorption, samples were cooled under a constant group-V flow. As-grown NW samples were

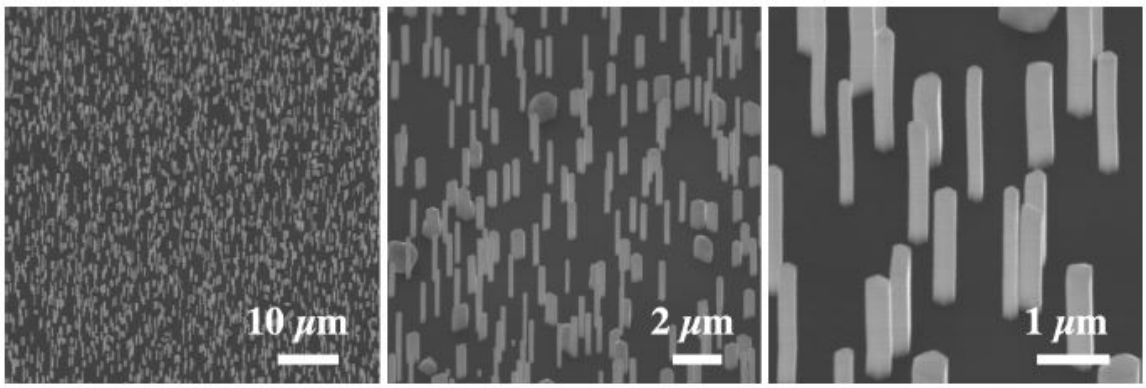

Figure 5.6: Tilted view SEM images of SAE of GaAsP NWs grown by MOCVD on a NSL-patterned sample are shown at three different magnifications.

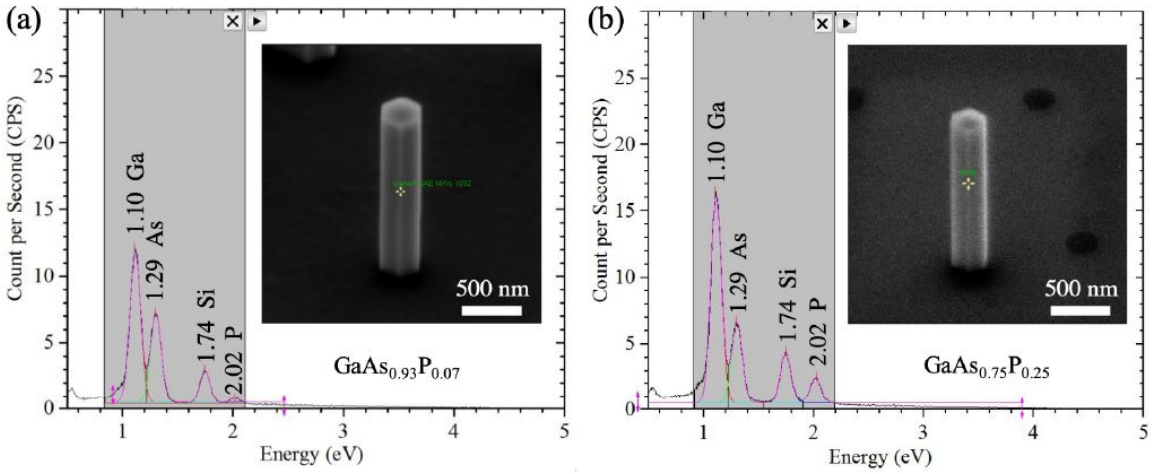

Figure 5.7: Single point EDX analysis of GaAsP NWs grown by SAE on Si(111), composition values of (a) $GaAs_{0.93}P_{0.07}$, (b) $GaAs_{0.75}P_{0.25}$ were measured.

imaged for morphology measurements using a Hitachi S-4000 SEM. The results for heteroepitaxy of vertical GaAsP NWs on Si are shown in Figure 5.3. The variation in diameter of NWs is due to the difference in size of pores.

To evaluate the solid phase incorporation of PH_3, a TESCAN MIRA3 SEM equipped with energy dispersive x-ray spectrometry (EDXS) capability was used. The result of a point scan from a single NW (shown as an inset) is demonstrated in Figure 5.4 (a). By calculating the integrated intensity of detected peaks of the EDX spectrum, the composition was shown to be $GaAs_{0.93}P_{0.07}$. In order to achieve the target $GaAs_yP_{1-y}$ composition of y = 0.73, the flowrate of PH_3 was increased by a factor of 5, while keeping AsH_3 and TMGa flowrates at fixed values. The EDX measurment showed that this 5-fold increase in availability of PH_3, lead to ∼3.5 times increase in solid incorporation of P-content (Figure 5.7(b)).

Selective Area Epitaxy of GaAsP NW Arrays Using Photolithography

In order to generate an ordered array of NWs with full wafer coverge, photolithography was performed using the ASML stepper at the SMFL facilities at RIT. The common problem with SAE on NSL samples is illustrated in Figure 5.5(a). Unlike the sample prepared by photolithography (Figure 5.8(b)), only part of the NSL-patterned sample was suitable for NW growth. For photolithography, first a 50 nm SiO_2 layer was deposited on a 6" Si(111) wafer by PECVD. After spin coating of AZ MIR 701 photoresist, the wafer was patterned with the optimum exposure condition using a mask containing an array of pores with 500 nm diamter and center to center pitch of 1 μm. The result is shown in the 45°-tilted view SEM image shown in Figure 5.6(a).

The heteroepitaxy of GaAsP NWs using these fabricated samples were performed using the similar experimental method explained in the previous section. Here the motivation is to use the low-cost patterning technique of photolithography which leads to realization of holes larger in diameter than the target NW dimensions. However, this challenge can be addressed by adding a simple fabrication step between epitaxy of core and shell segments. As an example, this can be done by forming an isolating layer of spin on glass (SOG) after growth of the NW core segments.

Even though for III-V compounds such as InAs, it is possible to grow NW arrays with smaller diameter than the diamter of pattern itself, unfortunately this was not

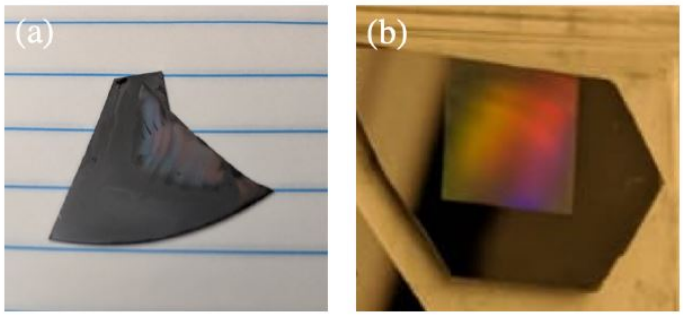

Figure 5.8: (a) Partial coverage of NWs growth on a sample prepared by NSL method. (b) Full coverage of a sample patterned by photolithography.

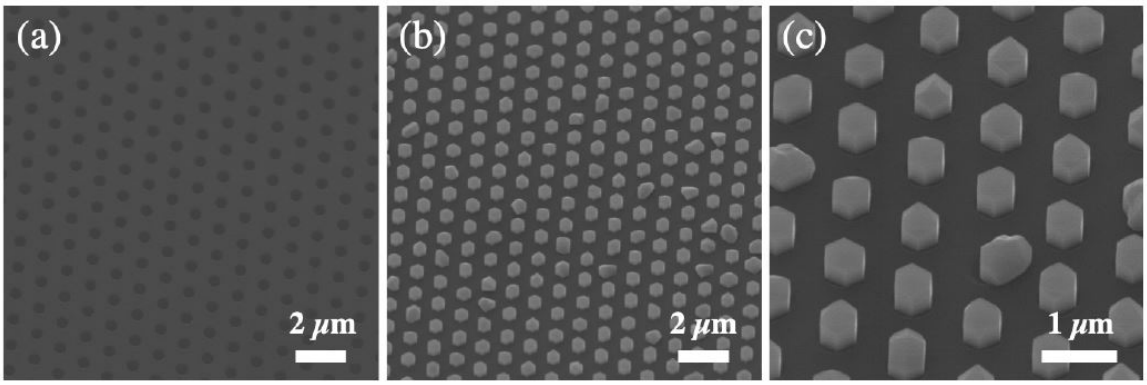

Figure 5.9: (a) Patterns on a Si (111) wafer prepared by photolithography, (b) Heteroepitaxy of GaAsP NWs on the same sample in (a). (c) high radial growth rate of GaAsP NWs is conducive to integration of features with low aspect ratio.

feasible for SAE of GaAsP in our explored growth parameter space. Here, for the constant flow of 3580 nmol/min TMGa, the V/III ratio was changed between 800 and 1600 by doubling both PH_3 and AsH_3 flowrates. These flowrate values were repeated for T_G equal to, (i) 850°, (ii) 950°, and (iii) dual temperature growth mode of 850°-950°. In all cases, the resulted height of NWs did not exceed 0.5 μm, as demonstrated in Figure 5.6. This unsuitable SAE results for fabrication of NW-based SCs led us to use of EBL, which is explained in the next section.

5.4 Selective Area Epitaxy Using Electron Beam Lithography

5.4.1 Experimental Details

Electron-beam lithography (EBL) is a technique that uses a focused electron-beam (e-beam) to generate a custom pattern on a surface covered with an e-beam resist. For a positive (negative) resist, rastering of the e-beam changes the solubility of the chemical and enables a selective removal of the exposed (unexposed) part of the sample by submerging it in a solvent. The main advantages of EBL are: (1) capability of generating small size patterns on the order of ∼10 nm or less and (2) no need for a physical hard mask. Both features offer great flexibility for testing new ideas during a design trial phase of an experiment.

Here, the JEOL JBX9500FS EBL system, located at Cornell NanoScale Science and Technology Facility (CNF), was used to generate an ordered array of nanopores with diameter ∼200 nm and center-to-center pitch of 500 nm in SiO_2 layer on Si (111) substrates. This tool operates at accelerating voltage of 100 kV, with maximum beam current of 100 nA. With field size of 1 mm and minimum beam diameter of 3.2 nm, JEOL 9500 is capable of writing large area patterns with features as small as 6 nm.

Before exposing the substrate, two sets of preparations are needed: (1) providing the desired pattern file and write condition details for the JEOL 9500, (2) sample preparation prior to loading the substrate in the tool. This process initiates with preparing the pattern files using a CAD tool and extracting the file in .gds format. Here, the L-Edit software was used to draw arrays of dots and borders in two separate files. Next, using a Beamer software the .gds file should be converted to .v30 files. This step translates the pattern file for the JEOL 9500, meaning type of pattern, shape and pitch of shots, and beam step size for each specific pattern are defined for the EBL tool. Next, specific code scripts as job (.jdf) and schedule (.sdf) files bridge

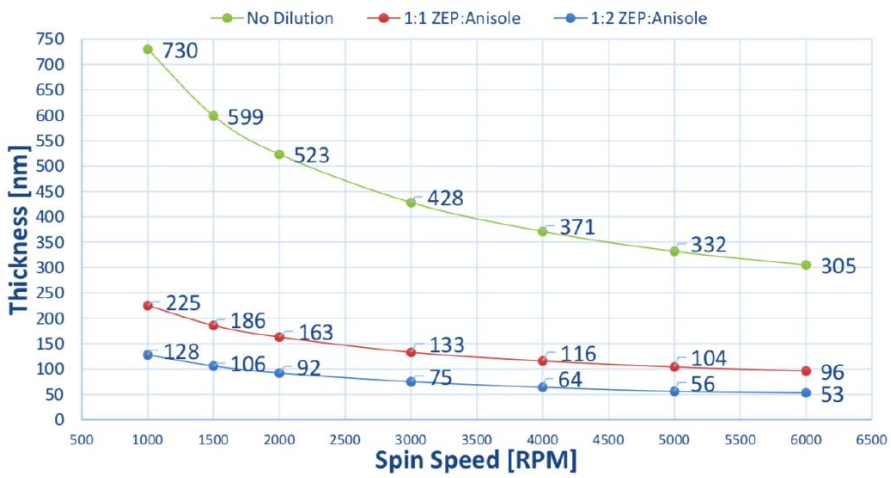

Figure 5.10: Spin curve for ZEP520A e-beam resist for diluted and not diluted solution. Here, ZEP520A with no dilution (green curve) is used [198].

the information embedded in .v30 files and the details of the writing procedure. The prepared and translated pattern and write conditions should be checked in the JEOL 9500 software. Finally, before starting the exposure, the tool should be calibrated for beam current reading, correct alignment of sample, and a very precise electron gun column alignment. It is important to note that if an EBL write uses more than one beam current, the electron gun column should be calibrated for each value of beam current. This is the case here and will be discussed more in the following paragraphs.

Prior to initiating EBL, a 2" Si (111) wafer was cleaned using the RCA process. Next, a ∼50 nm SiO_2 film was deposited using the P5000 PECVD. This step was followed by measuring the film thickness using a Woollam VASE ellipsometer, via averaging multiple point measurements. For 5 sec deposition of low stress TEOS, using "1kA-TEOS-LS" recipe, the average thickness of the film was measured to be ∼50 nm. Here ZEP-520A was chosen as the positive e-beam resist. Compared to poly(methyl methacrylate) (PMMA), ZEP 520A is 5 times more sensitive to the e-beam. This characteristic allows for a faster writing speed and makes ZEP-520A economically a better choice. ZEP 520A was spin coated on the prepared wafer at 5500 rpm for 30 sec followed by 2 min bake at 170 °C. The thickness of spin coated resist was measured to

be ∼300 nm using using the FilMetrics F50-EXR optical film measurment instrument at the CNF. This value is in good agreement with the expected thickness for undiluted ZEP520A at 5500 rpm (Figure 5.10).

5.4.2 Results and Discussions

For the desired SAE pattern, the size of the main two features of nanopores (d = 200 nm) and border (w = 100 μm) differ by three orders of magnitude. Therefore, to optimize the EBL write duration, and thus make the patterning step more cost-efficient, two separate sets of exposure conditions were used. The dose matrices tests revealed the optimum write conditions for these features. For realizing holes, a 60 μm objective aperture was selected, along with minimum beam current of 2 nm and areal dose of 592 $\mu C/cm^2$. The combination of these conditions lead to a beam size of 5 nm. In contrast, to pattern borders with mesa size of 400 μm, a 110 μm objective aperture, a beam current of 20 nm, and areal dose of 350 $\mu C/cm^2$ was used. For the specific case of JEOL 9500, this advanced double beam exposure technique takes advantage of a precise automatic positioning of apertures.

A representative SAE masking template patterned using this procedure is shown in Figure 5.11. After exposure and developing the e-beam resist, the 100 μm wide border and an array of dots can be seen in the optical image shown in Figure 5.11 (a). The regions with/without e-beam resist, as well as array of holes, are marked on this figure. The planar view SEM image of the same feature, after emerging the sample in 10:1 BOE and stripping the extra e-beam resist, is shown in Figure 5.11 (b). Higher magnification images of the same region of the sample show a well-defined array of nanopores in the SiO_2 layer (Figures 5.11 (c-d)). The exposed Si (111) substrate inside the holes will be the growth surface for SAE of GaAsP NWs. A series of various optimization steps lead to write time of 14 min (22 min) for 230 patterns of nanopore arrays (border).

After the e-beam the writing step, the post-exposure development of the resist was performed by submerging the sample in ZED-N50 (n- amyl acetate) for 45 sec, followed by 30 sec in methyl isobutyl ketone (MIBK) and 30 sec spraying isopropyl alcohol (IPA) solvent. Lastly, RIE was used to transfer the pattern to the SiO_2 film.

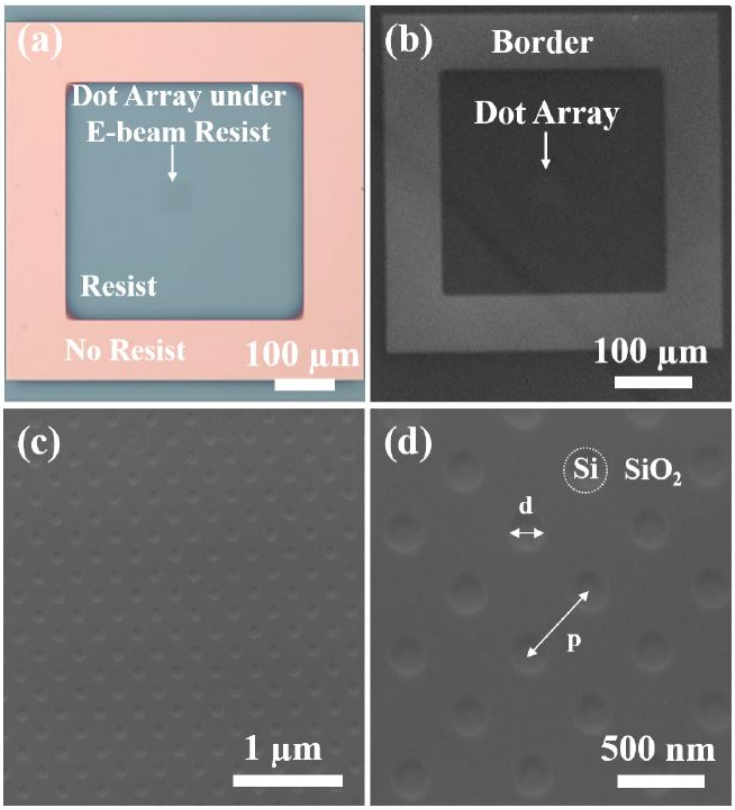

Figure 5.11: (a) An optical image of an array of dots surrounded by 100 μm wide borders after e-beam exposure and development, (b) top view SEM image of the same pattern after RIE and resist removal, (c) and (d) top view SEM images showing array of dots from the same pattern.

The RIE step was optimized for a 20 nm/min etch rate on planar SiO_2 film. Differnt RIE times were tested in order to find a RIE condition conducive to exposing the Si surface in all of the patterned pores. Since NW growth via SAE is very sensetive to the uniformity of exposed Si surface, 200% of time needed to remove 50 nm SiO_2 film was selected to clear the pores. It is worth noting here that the e-beam resist, ZEP-520A, showed a very good stability during the RIE step and was removed by a descum step followed by RIE using the P5000 PECVD instrument at the SMFL.

So far, realization of SAE-suitable masking templates via EBL is described. Here the reasons for design of such a pattern, and initial results on SAE of GaAsP will be discussed. Based on rigorous coupled-wave analysis (RCWA) modeling performed at RIT, for GaAsP NWs on Si cell, arrays of NWs with the pitch of 500 nm and diameter

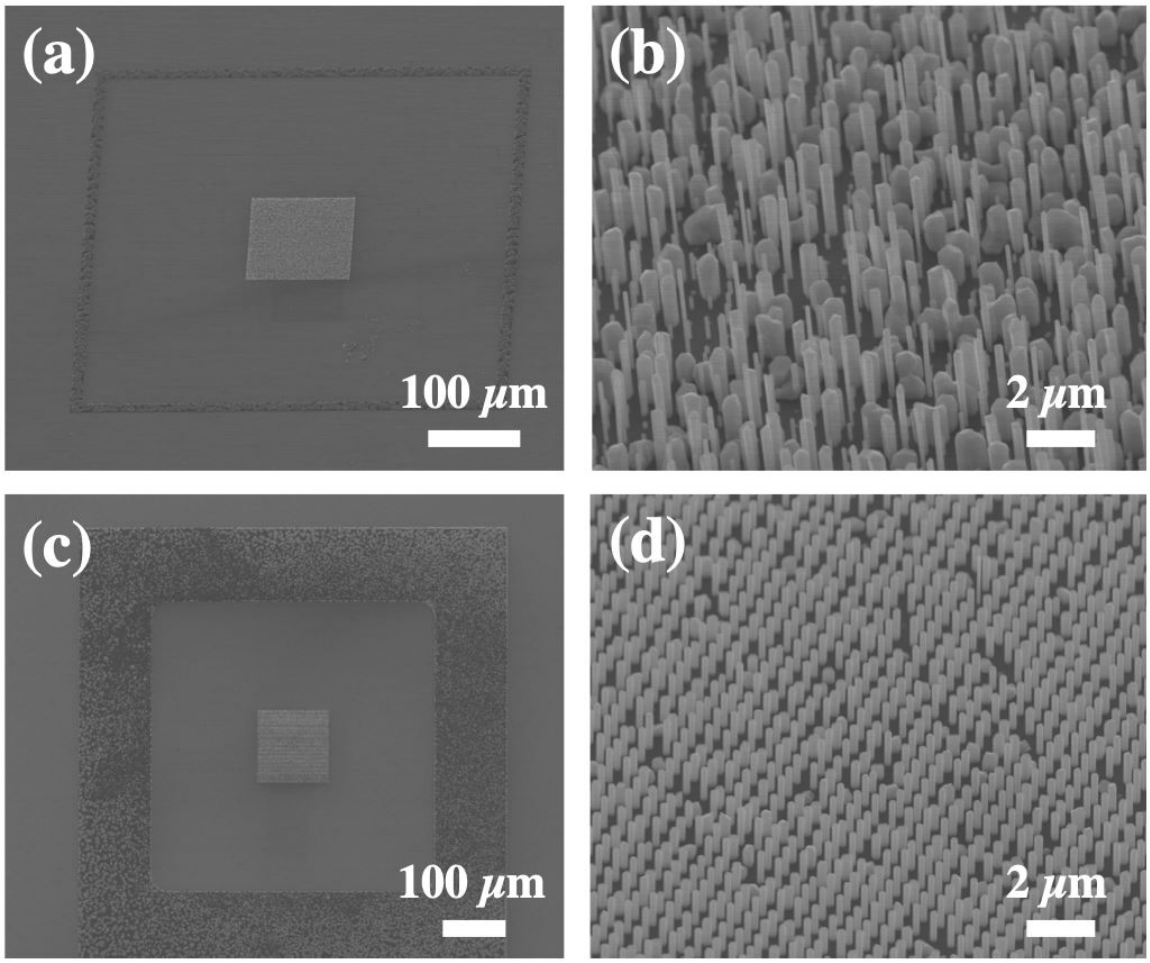

Figure 5.12: The influence of mesa border (atomic sink region) on the morphology of NWs grown by SAE. (a) An array of GaAsP NWs in the center of aof a mesa with border width of 10 μm after MOCVD growth, (b) Tilted view SEM image zomed-in on the array of NWs, (c) A NW array centered in a mesa with border width of 100 μm, (c) NWs at the center of the pattern shown in panel (c).

of 350 nm enables optimal light absorption and current-matching with a Si sub-cell in a tandem-junction device. Thus, the same values were targeted in the preparation of pattern files for EBL except the diameter was set to 200 nm for NW core segment. In this way, the SiO_2 template acts to isolate conduction pathways from NW shell segments through the substrate in a coaxial NW device design. As for border, it allows for realization of a more controllable NW growth regime and acts as an atomic sink for excess of materials. This concept is illustrated in Figure 5.12, where results from a single MOCVD GaAsP NWs SAE growth run are compared between NW arrays

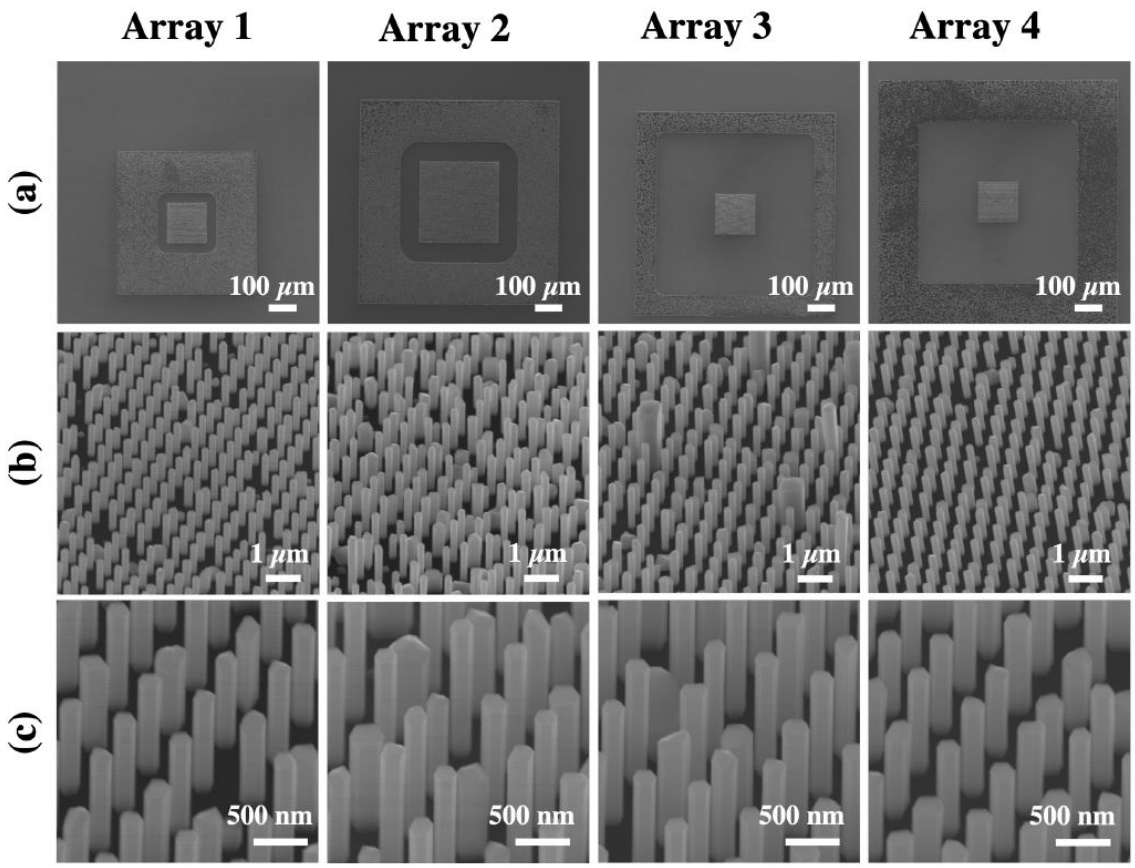

Figure 5.13: The influence of masking template geometry on morphology and yield of SAE-grown NWs. (a) Top view SEM images of arrays; Array 1 with W = 100 μm and M = 150 μm × 150 μm, Array 2 with W = 50 μm and M = 150 μm × 150 μm, Array 3 with W = 50 μm and M = 400 μm × 400 μm, Array 4 with W = 100μm and M = 400 μm × 400 μm. (b) and (c) Tilted view SEM image of the corresponding NW arrays.

shown in panels (a) and (c). In both cases, a 100 μm × 100 μm field of nanopores with similar size and seperation is centered on a 400 μm × 400μm mesa surrounded by borders with width of 10 μm in panel (a) and 100 μm in panel (c). The 45° tilted-view SEM images in Figure 5.12 (b) and (d) demonstrates how the growth rate of NWs can be controlled by the size of atomic sink regions (mesa borders). In panel (d), due to larger border size (100 μm), the SAE growth rate enhancement effect is mitigated, meaning that growth is more controlled and an array of ordered non-tapered NWs is achieved. In panel (b), however, the 10 μm border acts as a weak sink and the high growth rate leads to overgrowth of islands and non-homogeneous growth of NWs.

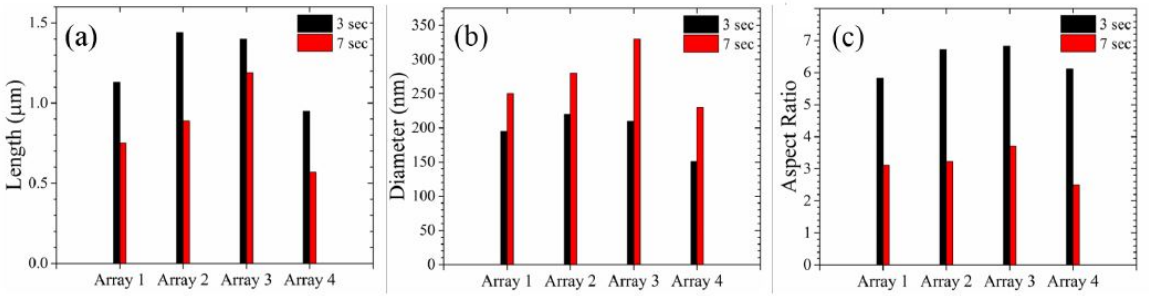

Figure 5.14: Average length, diameter and aspect ratio of NWs in Figure 5.13 for Arrays 1 through 4, on samples with 3 sec (black bars) and 7 sec (red bars) pre-growth BOE treatment.

To further explore suitable patterns for SAE of NWs on Si, a combination of two mesa sizes (M) an two border widths (W) were tested in the four patterns shown in Figure 5.13(a). In all four cases, a 100 μm $\times$ 100 μm array of nanopores with diameter D = 200 nm and center-to-center pitch P = 500 nm is used, centered in mesas of different sizes with exposed borders of different widths. Top view SEM images shown in Figure 5.13(a) represent; Array 1 with W = 100 μm and M = 150 μm $\times$ 150 μm, array 2 with W = 50 μm and M =150 μm $\times$ 150 μm, Array 3 with W = 50 μm and M = 400 μm $\times$ 400 μm, Array 4 with W =100 μm and M= 400 μm $\times$ 400 μm. To evalute the effect of mesa and border sizes on SAE of GaAsP NWs, a sample was prepared with EBL containg all four different patterns, and the NW lengths, diameters, and aspect ratio, as well as NW yield, were measured by post-growth SEM imaging. The growth of NWs in the array of pores and overgrowth of parasitic islands in the border area is shown in Figure 5.13(a). Since SAE is a templated epitaxy technique, nucleation sites are limited to the exposed Si surface only and SiO_2 film suppresses any form of growth outside of the array and border areas. This selectivity is not limited to the SiO_2 PECVD prepared template layer, even the native oxide on Si surface inside the pores can be a diminishing factor for the total yield of a NW array. This means that a pre-growth wet etch step prior to loading the sample into the reactor has a strong influence on NW growth. In this

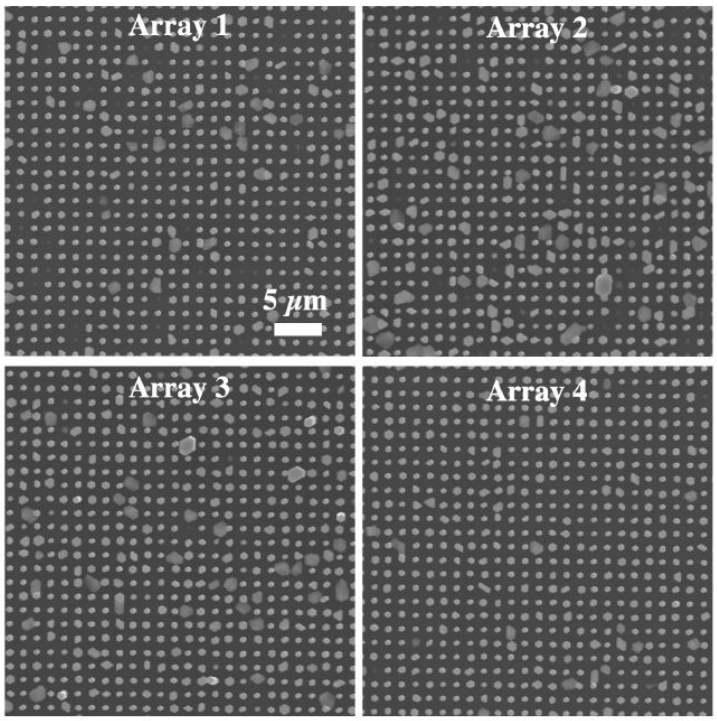

Figure 5.15: Top view SEM images from Array 1, 2, 3 and 4 shown in Figure 5.10(a). The width and area of the borders in Array 4 allows heteroepitaxy of GaAsP NWs on Si with high yield.

sense, to find the optimal pre-growth oxide removal step, 3 sec and 7 sec oxide removal treatment were performed on two sets of samples by submerging the samples in a 10:1 BOE solution follow by a quick rinse in DI water.

The 45°-tilted SEM images in Figures 5.13(b) and (c) shows the result of GaAsP NWs heteroepitaxy on Si (111) in the four arrays illustrated in Figure 5.13(a), labeled by Array 1 through 4. Average NW lengths and diameters were measured for 100 NWs in each array for the two sets of samples with 3 sec and 7 sec pre-growth BOE treatment. The results of these measurments are plotted in Figure 5.14. As expected for the sample with 7 sec BOE treatment, in all four arrays, the NWs height (diameter) is less (more) than the wires grown on the sample with 3 sec BOE treatment. This is because the wet etch is not a directional etch process and therefore the pre-growth treatment leads to unavoidable increase in a diameter of the patterned pores, and consequently a decrease in NWs length. Array 1 and 2, as well as Array 3 and 4,

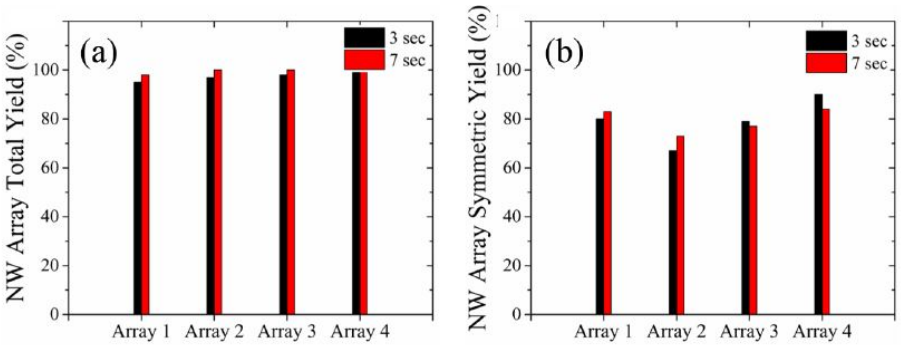

Figure 5.16: The measured (a) total, and (b)symmetric yields of NW arrays shown in Figure 5.15 for arrays 1 through 4, on samples with 3 sec (black bars) and 7 sec (red bars) pre-growth BOE treatment.

share the same mesa size. Therefore the direct comparison between these arrays is straightforward. For two arrays with the same mesa area, the array with larger border area allows a smaller amount of material to be captured by the exposed area in the nanopores arrays. Naturally this leads to smaller average length and diameter for the NWs. For example, Figures 5.14(a) and (b) show that the NWs in Array 1 exhibit a reduced average length and diameter compared to the NWs in Array 2, due to the larger atomic sink region surrounding Array 1. Similar results are observed for Array 4 compared to Array 3. Although the measurments in Figure 5.14(c) illustrate the highest aspect ratio belongs to Array 3 and 2, but the tilted SEM images in Figure 5.13(b) and (c) exhibit superior uniformity in Array 1 and 4. To have a better understanding of areal coverage of NWs in each array, top view SEM images are shown in Figure 5.15. This Figure shows the difference in NW yield between Arrays 1 - 4 for samples subjected to a 3 sec pre-growth BOE treatment.

To evaluate the best pattern, evaluate the best pattern two types of yield measures for NW arrays are defined and measured in Figure 5.16(a) and (b). The total yield is defined as the ratio of total number of NWs to total number of pores, which is an indication of global NW areal coverage. As Figure 5.16(a) illustrates, the longer pre-growth wet etch treatment leads to a slightly higher number of pores with exposed Si surface. The symmetric yield shown in Figure 5.16(b), on the other hand, is defined

as the ratio of total number of hexagonally symmetric NWs to the total number of pores. The symmetric yield demonstrates if the ratio of exposed area in the borders and size of the mesa are suitable for heteroepitaxy of NWs with target value of NW diameter. Based on 5.13 (a) and (b), array 4 on the sample with 3 sec BOE shows the highest values of total and symmetric yield. These measurments are in agreement with Figure 5.13(b) and (c), and Figure 5.15.

5.5 Selective Area Epitaxy Using Talbot Displacement Lithography

5.5.1 Experimental Details

As described in section 5.3, samples prepared using NSL were used to establish SAE of GaAsP and composition study. Unlike NSL, a specific array of nanopores with targeted diameter and pitch can be defined using EBL. The EBL-prepared samples were used to explore SAE of GaAsP NW array, presented in section 5.4.2. The EBL

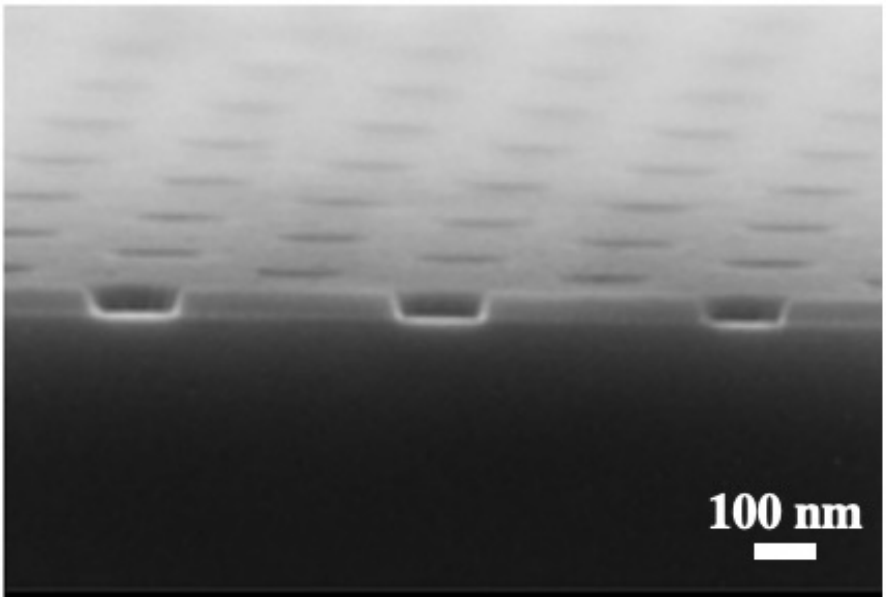

Figure 5.17: Cross-sectional SEM image of patterned SiO_2 template on Si substrate using TDL method (prepared by NanoLund lab).

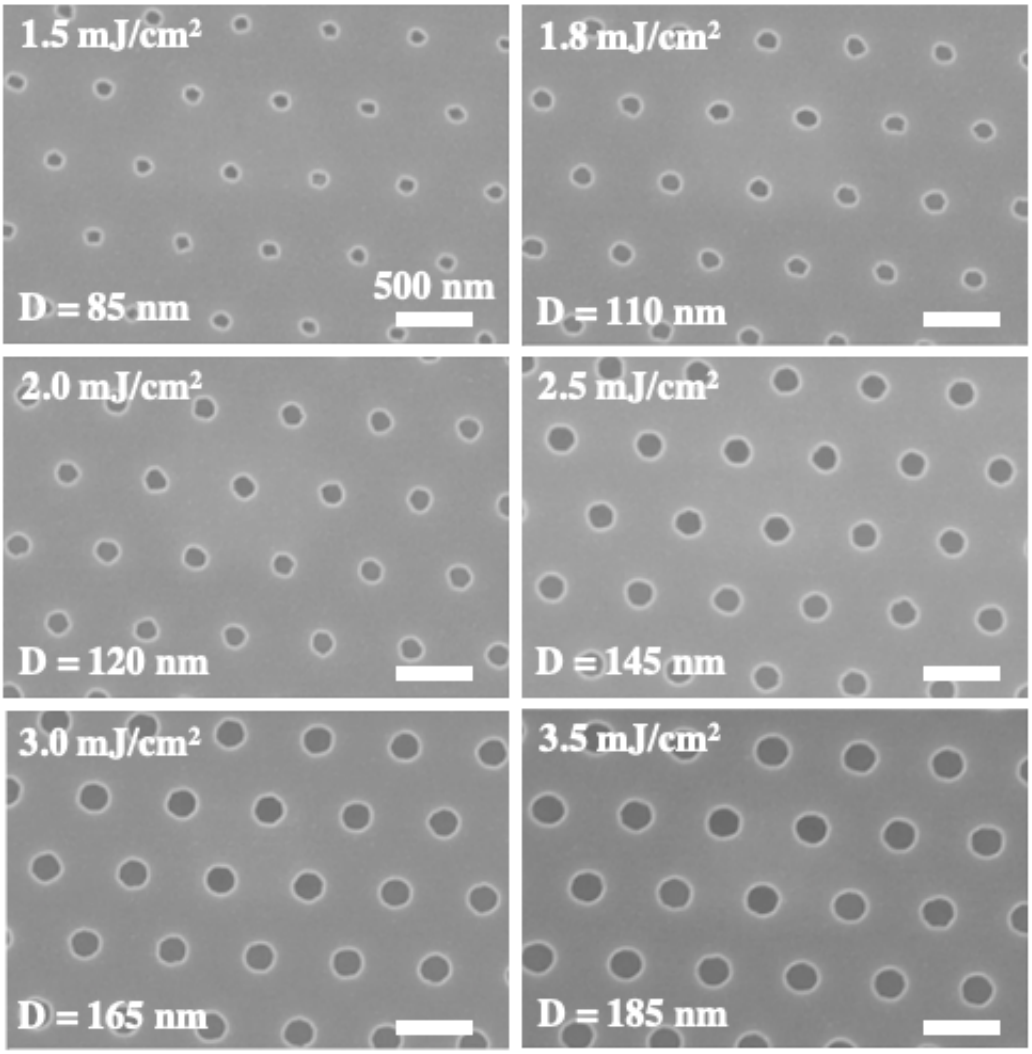

Figure 5.18: Top view SEM images showing results of dose exposure matrix for doses in the range of 1.5 mJ/cm^2 to 3.5 mJ/cm^2. The average diameter for each dose test is indicated on each panel. All scale bars represent 500 nm (prepared by NanoLund lab).

technique is conducive to small area patterning and it is not cost effective to use this lithography method for wafer scale patterning. Therefore, TDL was used to pattern samples for large area SAE trials. The process flow of TDL performed in collaboration with the NanoLund Lab (Lund University, Sweden) is listed below. Figure 5.17 shows a cross-sectional SEM image of a Si substrate patterned with TDL method. The deposited SiO_2 film acts as a template for the SAE of NWs. The results of dose exposure matrix performed by NanoLund lab is shown in Figure 5.18.

1. Wafer dehumidifying
2. Resist spining and baking
3. Exposure in TDL-Phabler 100DUV for 1.5 mJ/cm^2 to 3.5 mJ/cm^2
4. Post exposure baking
5. Development
6. Dry etch of SiO_2 in RIE Sirius T2 for 180 sec, with 20 sccm CHF_3, with chamber pressure of 20 mT, with set point power of 75 Watts
7. Oxygen plasma for 3 $\times$ 1 min, with chamber pressure of 5 mBar
8. Remover 1165 at 100 °C for 5 min, DI water flowing 5 min, N_2 drying
9. Oxygen plasma for 1 min, with chamber pressure of 5 mBar

5.5.2 Results and Discussions

Here, highly n-doped single side polished 2" Si (111) wafers with 0° off-cut is used as growth surface for assembly of NWs. First, ∼50 nm SiO_2 film is deposited as the growth template for SAE of GaAsP-GaP core-shell NW arrays. This step was perfomed using the PECVD P5000 tool at the SMFL facility at RIT. Next, samples were sent to NanoLund lab for TDL patterning. The details of TDL process is explained in the previous seciton. Prior to loading samples into the MOCVD reactor, BOE surface treatment was used on patterned Si substrates to remove the native oxide and expose the Si surface inside the pores. Trimethylgallium (TMGa), diethylzinc (DEZn), arsine (AsH_3), phosphine (PH_3), and disilane (Si_2H_6) are used as metal organic and hydride precursors. Prior to initiation of NW growth, a desorb step was performed at 970 °C for a duration of 10 minutes under AsH_3 and PH_3 flow. Then, the susceptor temperature was stabalized at the growth temperature (T_G) of 930 °C, and AsH_3 and PH_3 flowrates were set to 10 sccm and 60 sccm, respectively. The NW growth step was marked by flow of TMGa and Si_2H_6 into the reactor chamber for duration of 45 minutes. To adjust the growth parameters for growth of the GaP shell segment, the flow of TMGa and Si_2H_6 were stoped while the T_G was set to 830 °C, AsH_3 flowrate was terminated and PH_3 flowrate was set to 70 sccm. The GaP shell segment

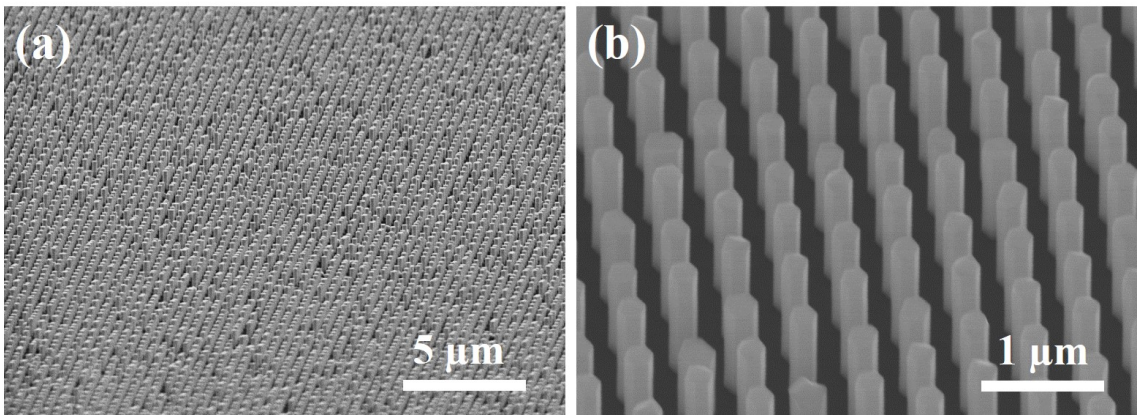

Figure 5.19: SAE of GaAsP:Si-GaP:Zn core-shell NW arrays on patterned n-type Si substrate.

Table 5.1: Comparison between simulated and experimental parameters for GaAsP-GaP core-shell NW heterostructures.

Parameter	Units	Simulation	Experiment
NW Length	µm	1.50	1.58
NW pitch	nm	500	500
Total NW Diameter	nm	380	265
GaAsP Core Thickness	nm	350	235
GaP Shell Thickness	nm	30	~ 30
GaAsP Core Doping Concentration	$1/cm^3$	5×10^{18}	$\sim 5 \times 10^{18}$
GaP Shell Doping Concentration	$1/cm^3$	1.5×10^{18}	$\sim 1.5 \times 10^{18}$

was grown for a period of 10 minutes by flowing TMGa and DEZn at the reduced temperature, after which samples were cooled under a constant flow of AsH_3 and PH_3. For both core and shell segments the V/III ratio was set to 795. It is crucial to ensure that the core segment of NWs fully fill the patterned pores, and the SiO_2 layer isolates the shell layer from the substrate. This was done by performing a radial growth rate study to calculate that the growth time for the core segment. The resulted GaAsP:Si-GaP:Zn core-shell NW arrays is showen in Figure 5.19.

Table 5.1 compares the parameters obtained from simulation and experimental trials for GaAsP-GaP core-shell NW arrays. A series of growth trials were carried out to tune and measure the growth rate of the core GaAsP segment. The presented values for NW length and diameter are average values obtained from measurements done on 50 NWs using tilted-view SEM images. It should be noted that the thickness correlated to the overgrowth of shell segment is an estimation based on the studies

carried out on the core segment morphology. Furthermore, the doping concentrations are targeted values based on previous growth calibrations of GaAs planar film. These targeted values are counted as a fair estimation for doping concentrations in NW arrays.

5.6 Conclusions

In the photovoltaics market, Si-based solar cells have 95% of the production share and are capable of producing a maximum theoretical efficiency of ∼30%. III-V semiconductor solar cells can exceed the Si conversion efficiency threshold, particularly with use of tandem junction device structures; however, III-V photovoltaics suffer from high materials and manufacturing costs. To resolve these challenges, tandem junction devices comprised of III-V semiconductors coupled with Si are one of the most promising candidates. The main obstacle in heteroepitaxy of high crystal quality III-V semiconductors on Si can be addressed via growth of high aspect ratio NW structures. Due to their large surface-area-to-volume ratio and small footprints, NWs can effectively accommodate heterointerfacial strain without risk of threading dislocation formation during highly lattice mismatched heteroepitaxy. Ternary III-V compounds of $GaAs_{0.73}P_{0.27}$ with the band gap energy of 1.75 eV provide an optimal solution as a top-surface III-V sub-cell in tandem with a Si sub-cell. Reports on epitaxy of GaAsP NWs on Si(111) is limited to the vapor-liquid-solid approach.

Here, for the first time, SAE of vertically-aligned $GaAs_yP_{1-y}$ NW arrays on patterned Si(111) substrates using MOCVD is presented. Trimethyl-gallium (TMGa), arsine (AsH_3), and phosphine (PH_3) are used as precursors for the supply of Ga, As, and P growth species, respectively. In prior work, we have theoretically determined that maximum current density in a current-matched GaAsP NW array on Si tandem device can be realized using GaAsP NWs with 350 nm diameter, center-to-center distance of 500 nm, and heights of 1.5 μm. Here, SiO_2 SAE masking templates

on n-type Si substrates are patterned with 200 nm diameter pores for growth of n-type GaAsP NW core segments, and subsequent lateral extension of p-type NW shell segments with thickness of 75 nm, to reach the targeted diameter of 350 nm. The SAE condition is established for V/III ratios between 500 and 1600 at growth temperatures between 850 °C and 950 °C. Compositional tuning of $GaAs_yP_{1-y}$ NWs toward a targeted composition of y = 0.73 is realized by altering the molar flow ratio of hydride precursors between 0.55 and 0.86.

The effect of growth rate on morphology, total yield, and symmetric yield of GaAsP NWs is explored through modulation of the effective local supply of growth species. Here, nanopores are patterned within arrays of 100 μm × 100 μm dimensions at the center of oxide mesas, which are surrounded by mesa borders where the underlying Si substrate surface is exposed. Various configurations of mesa areas and mesa border widths are examined for a constant array size. Thus, by customizing the area of exposed Si in the mesa borders, which serves as an atomic sink, the yield and morphology of resulting SAE NWs is controlled. Under optimized growth conditions, $> 90\%$ yield of hexagonally symmetric GaAsP NWs on Si is realized using 400 μm × 400 μm mesas with border widths of 100 μm. This work is presented as a practical low-cost platform for high-efficiency III-V-on-Si tandem junction photovoltaic solar cells.

Chapter 6

Dissertation Conclusions

This dissertation presents heteroepitaxy of vertically aligned III-V NW arrays on foreign substrates using MOCVD. The three main growth surfaces used here are: (i) graphene, explored in Chapter 3, (ii) MoS_2, reported in Chapter 4, (iii) Si, described in Chapter 5. In this chapter, a summary of conclusions from all the projects is presented.

Chapter 3 focuses on an in-depth study of vdWE of InAs-based binary and ternary compounds on graphene via heteroepitaxy of high aspect ratio, vertical NWs. This work is categorized into two main parts. In the first part, the MOCVD growth parameter space had been explored to optimize length, diameter and number density of InAs NWs, as well as, areal coverage of parasitic islands. Epitaxy parameters including growth temperature (T_G), V/III ratio, and absolute flow rate of precursors are tuned for 650 °C $\leq T_G \leq$ 700 °C, 5 $\leq V/III \leq$ 250, 8 μmol/min $\leq \chi_{TMIn} \leq$ 32 μmol/min. The MOCVD growth trials showed that the growth parameters can be set to T_G= 650 °C, V/III = 25, and χ_{TMIn}=16 μmol/min for maximal NW aspect ratio, number density and minimal parasitic growth coverage. Next, an extensive TEM study revealed that NWs crystal structure is a characteristic polytypic and disordered phases of ZB and WZ and is invariant of the explored parameter space. Furthermore, to sudy the NWs growth evolution, a set of growth trials with fixed growth parameters and incremental growth durations were performed. This study showed that both axial and radial growth rates exhibit a gradual reduction, most likely due to a supply-limited

competitive growth regime. To further optimize the vdWE of NWs, two approaches were introduced. Firstly, by removing a pre-growth in situ AsH_3 treatment from the growth recipe, parasitic island coverage has been reduced by a factor of ∼0.62, with simultaneous enhancement of both NW aspect ratio and number densities. This is likely due to the reduction of growth species surface adsorption during the vdWE of InAs on SLG. Secondly, a two-step flow-modulated growth technique has been used to for integration of dense fields of high aspect ratio InAs NWs. The result of this work is published in [159], where the highest axial growth rate of 840 nm/min and NW number density of $\sim 8.3 \times 10^8$ cm^{-2} for vdWE of high aspect ratio (>80) InAs NW arrays on graphitic surfaces is reported.

In the second part of Chapter 3, the growth parameters of $InAs_yP_{1-y}$ ($1 \leq y \leq 0.8$) and $In_xAl_{1-x}As$ ($1 \leq x \leq 0.5$) NWs have been explored by alloying group-V and group-III, respectively. In the case of InAsP, the goal was set to achieve bandgap energy of 0.5 eV. This allows for incorporation of InAsP NW arrays as a bottom cell in a triple junction solar cell design with Si as a middle cell, which is described in Chapter 5. To increase the P-content beyond the MFC limits, one way is to increase the T_G. However, it has been shown that the NW number density suffers significantly under elevated T_G. To overcome this challenge, a two-temperature growth regime has been applied, where a dense array of InAs stubs were grown under the optimal growth condition, followed by InAsP segments grown under high axial growth rate. Next, composition and morphology of $In_xAl_{1-x}As$ NWs have been investigated as a function of T_G and flow rates of group-III precursors. Formation of vertically aligned InAlAs NWs under T_G=650 °C and ρ=0.5 has been shown. The result of this work is published in [121], where integration of InAlAs NWs on graphene was reported for the first time.

Chapter 4 reports integration of a novel nanohybrid system consist of InAs NWs grown on MoS_2 micro-plates, with one-to-one NW-to-MoS_2 placement. In this study, selective-area van der Waals epitaxy (SA-vdWE) of NWs was achieved for T_G=750

°C, V/III=25, and χ_{TMIn}=8 μmol/min, using a PLL-treated MoS_2 samples. The TEM study showed that similar to the case of InAs NWs formed on graphitic surface, the NWs grown under mentioned condition also exhibit polytypic crystal phases. Furthermore, the top-view SEM imaging showed a sidewall faceting modulation during radial growth of NWs. Specifically, it is shown that the sidewalls of the NWs core-segment are predominately {112}-oriented and in parallel with MoS_2 plate-edges. Finally, a nearly commensurate atomic arrangement of cubic InAs on hexagonal MoS_2 lattices is suggested, wherein one-half of the cubic InAs unit cell along the $[\overline{1}\overline{1}2]$ direction is approximately equal with a seven-fold multiple of the Mo-Mo (or S-S) spacing along the $[10\overline{1}0]$ direction of MoS_2 hexagonal lattice. This work offers a guide for integration of mixed-dimensional nanosystems based on vertically aligned III-V NWs on 2-D materials via SA-vdWE. Such a nano-hybrid system can be used as a basis for design of novel architectures for nanoelectronic and optoelectronic devices.

Chapter 5 presents integration of core-multi shell heterostructure of GaAsP NW arrays on Si substrate via SAE technique. The SAE of GaAsP NWs is achieved for TMGa flow rate of 3580 μmol/min, V/III=800, and T_G= 950 °C. The composition was tuned for $GaAs_{0.73}P_{0.27}$ NWs, aiming for band gap energy of 1.75 eV, by altering the molar flow ratio of hydride precursors between 0.55 and 0.86. This allows for incorporation of NW arrays as a top-cell in a III-V-on-Si tandem junction SC. Next, the influence of growth rate on morphology, total yield, and symmetric yield of GaAsP NWs has been studied by altering the effective local supply of growth species. This was achieved by using a set of four different patterns prepared by EBL. Under the optimized SAE growth condition, $>$ 90% yield of hexagonally symmetric GaAsP NWs on Si is realized using a 100 μm $\times$ 100 μm field of nano-hole arrays in the center of a 400 μm $\times$ 400 μm mesa with border width of 100 μm. This work is presented as a practical low-cost platform for high-efficiency III-V-on-Si tandem junction photovoltaic solar cells.

Chapter 7

Future Works

7.1 Fabrication of III-V-on-Si Tandem Solar Cells

The focus of this chapter is to explore experimental steps toward fabrication of III-V-NWs-on-Si tandem junction solar cells (SCs). The process steps for fabrication of GaAsP NWs on Si is presented. However, under unfortunate circumstance of a nation wide shutdown during the COVID-19 pandamic, the laboratories at RIT were closed. As a result, further testing and optimization of the SC device is incomplete in the presented work. The future works for completion of device fabrication is details here.

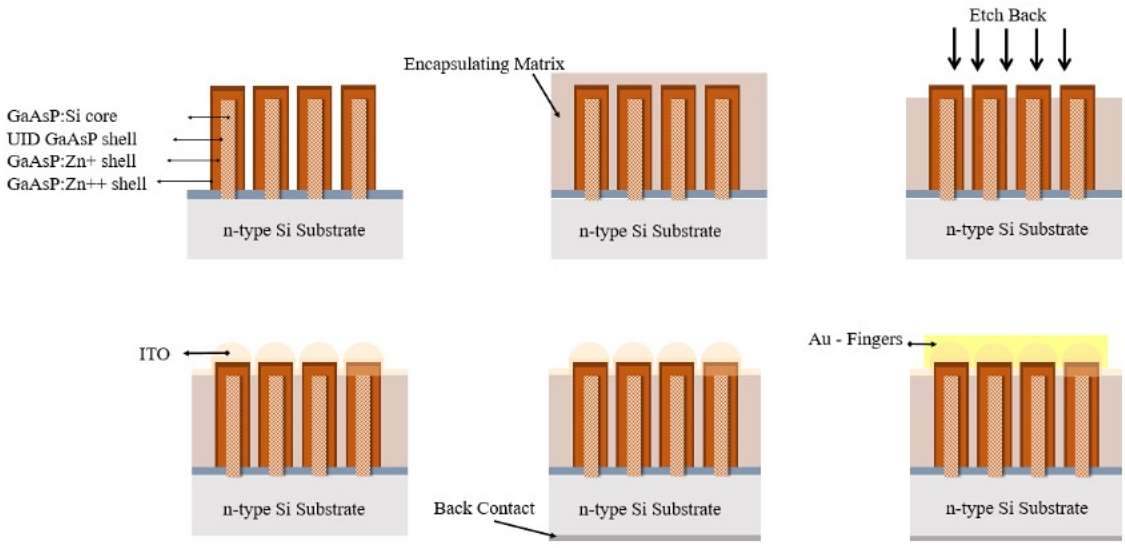

Figure 7.1: Schematic representation of process steps for fabrication of single junction GaAsP NWs on Si substrate.

7.2 Fabrication Process Flow

In this section the fabrication process for single-junction GaAsP NW array-based solar cells on Si is described. The fabrication steps are presernted in Figure 7.1. First, growth of NW arrays with core-shell hetrostructure is presented (Figure 7.1(a)). Next, planarization of vertical NW arrays is detailed wherein methods for encapsulating matrix (Figure 7.1(b)) and exposing NWs tips (Figure 7.1(c)) are demonstrated. The formation of transparent conductive oxide (TCO) on NWs and encapsulation matrix is explored. Finally, deposition of back and top surface contacts is presented (Figure 7.1(d)).

7.2.1 Planarization of Vertical Nanowire Arrays

To planarize the NW arrays, AZ Mir 701 photoresist (PR) was spin coated on the samples for 30 seconds at 5500 rpm. Next, samples were baked at 110 °C for 60 seconds using a hot plate. Figure 7.2(a) and (b) show 45°-tilted SEM images of NW arrays encapsulated in a PR matrix. To expose NW tips for contacting NW arrays,

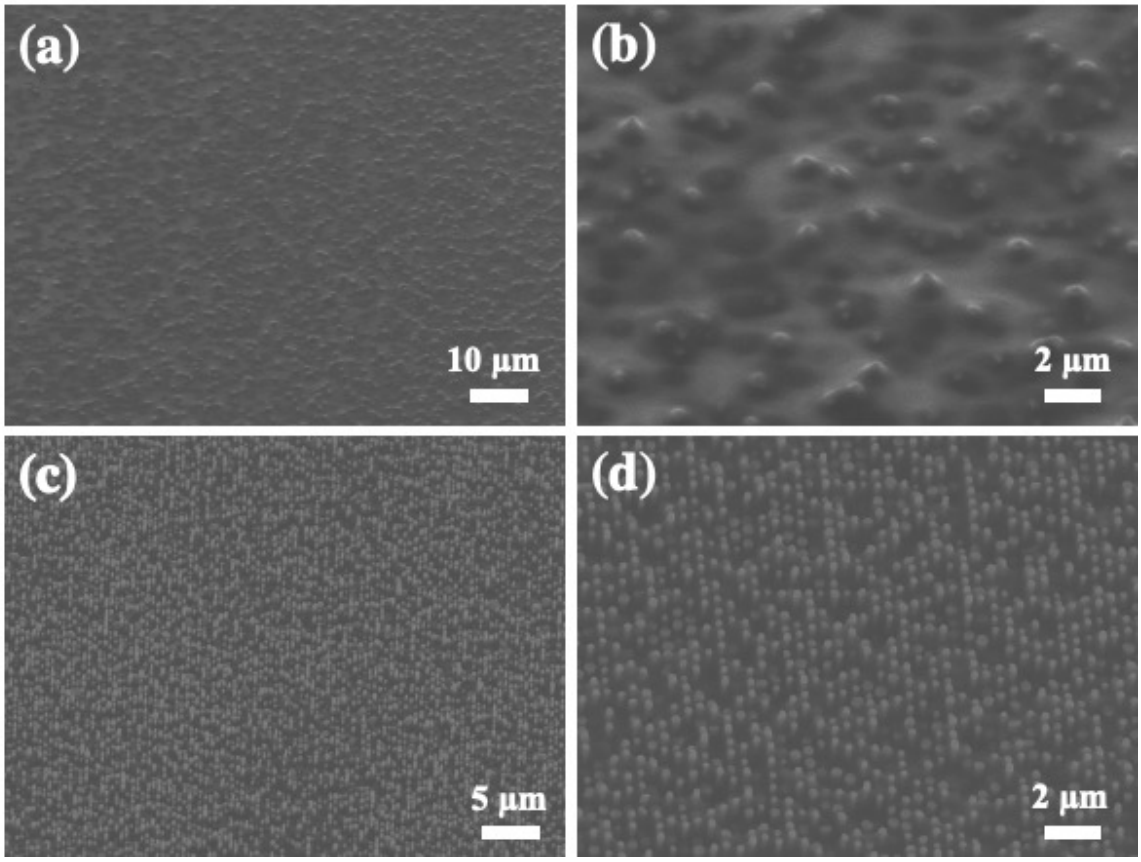

Figure 7.2: Planarization step: 45°-tilted view SEM images of (a), (b) NW arrays are encapsulated in a photoresist matrix, (c), (d) NWs tips are exposed using a RIE etch back step.

the PR matrix was etched back using reactive ion etch (RIE). After a 60 seconds initial stabalization step, 100 sccm of O_2 and 50 sccm of He gases were used, at 224 mTorr under 225 watts for 45 seconds. This step was performed using LAM 490 tool at SMFL facility. Figure 7.2(c) and (d) show 45°-tilted SEM images of NW array after the etch back step. Finally, samples were baked at 250 °C for 30 minutes. This step locks the PR encapsulation matrix and makes it unsusceptible to change during the following fabrication steps.

7.2.2 Transparent Conductive Oxide

Next, indium tin oxide (ITO) was used as the TCO layer. This step was performed using the CVC 601 sputter at SMFL facility. Figure 7.3 shows ITO sputtered on the

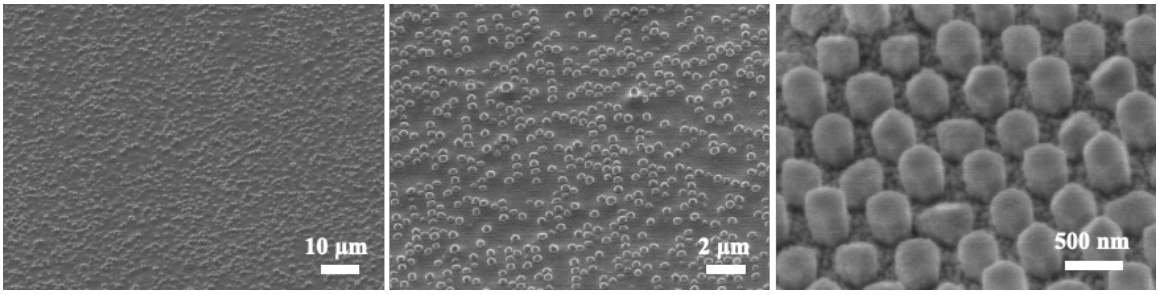

Figure 7.3: 45°-tilted view SEM images of NW arrays with sputtered ITO film as the top layer.

NW arrays shown in Figure 7.2(c) and (d). In this step, pulsed DC sputtering mode was used. The chamber vaccum level was reached to 5×10^{-8} Torr. First, while the shutter was closed, the power level was stabalized to 180 Watts at chamber pressure of 5 mTorr for 300 seconds. The Ar gas flow was stabalized at 40 sccm. Next, by opening the shutter, a 2000 Å ITO film was sputtered on the samples. A deposition rate of

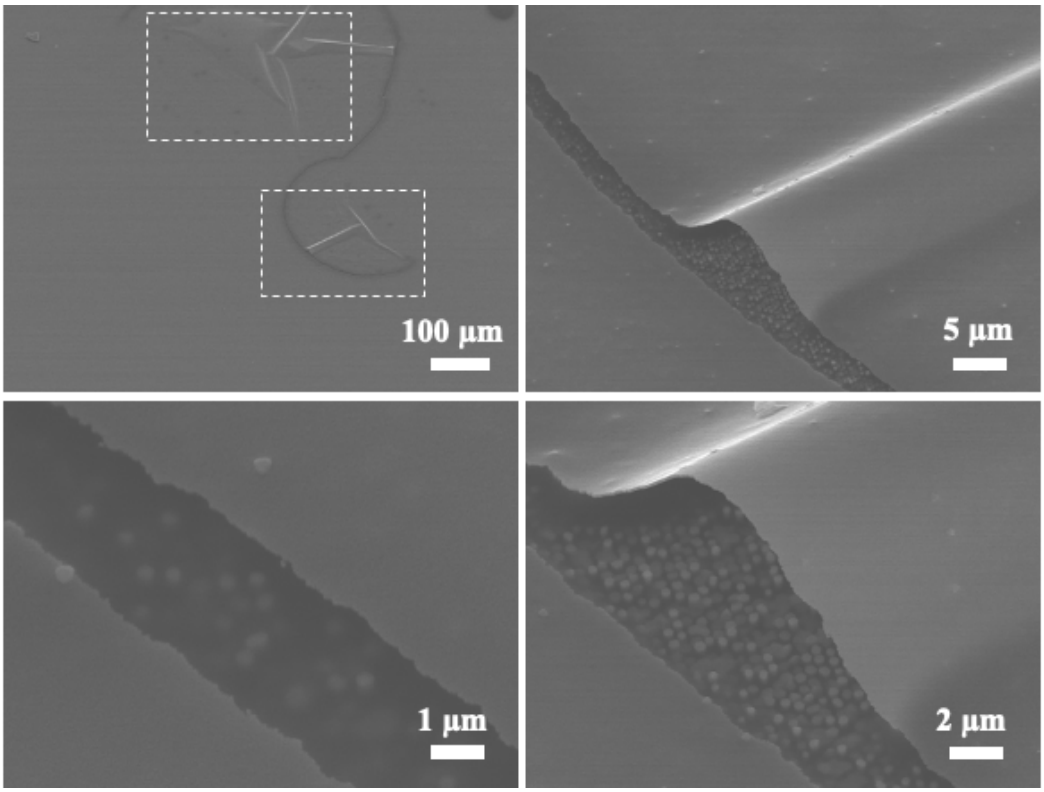

Figure 7.4: Low magnification, 45°-tilted view SEM images of ITO layer on NW arrays. Blistering and delamination defects can be seen in the ITO film. Defected areas are highlighted in dotted white borders.

0.64 Å/sec was measured for this process. Next, samples were baked at 250 °C for 30 minutes using a hot plate. As shown in Figure 7.4, the ITO film showed blistering and delamination defects. This can be attributed to lack of adhesion between the ITO, NWs tips and the PR matrix.

7.2.3 Back and Top Surface Contacts

For the back surface contact, a blanket film of Al was sputtered on backside of the Si substrates using CVC 601 sputtering. Prior to loading, backside of the samples were cleaned using IPA and acetone to remove any organic residues. In this process, the chamber pressure, power level, and Ar flowrate were set to 5 mTorr, 1000 Watts, and 20 sccm, respectively. The deposition rate was measured to be 2 Å/sec. Next, an array of patterns were defined for the top surface contact using photolithogrpahy using a Suss MA56 mask aligner. After exposure and developing steps, samples were loaded in the Lasker PVD75 thermal evaporator for deposition of Au. First, a 10 Å Ti film was deposited acting as an adhesion layer between ITO and Au. Then, 100 Å of Au film was deposited as top contact. Figures 7.5 shows an array of fabricated devices. The Au film is patterned in different sizes to contact NWs arrays.

As shown in Figure 7.6 and Figure 7.7, extensive blistering and delamination

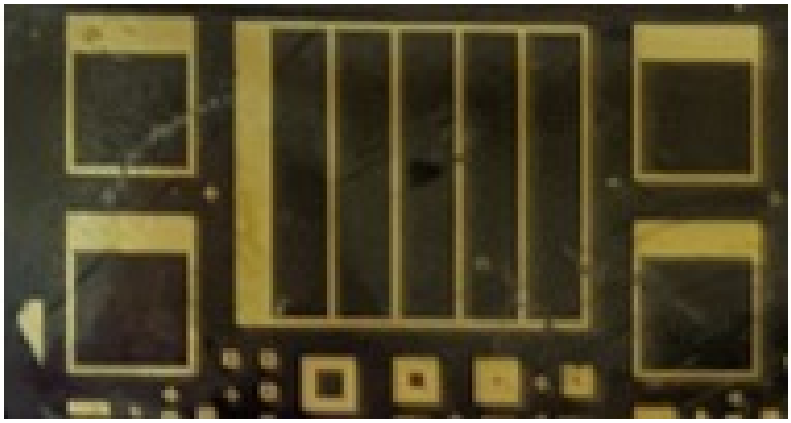

Figure 7.5: Photograph of an array of SC devices based on GaAsP:Si-GaP:Zn core-shell NW arrays on a n-type Si substrate.

defects are observed by SEM and optical images. These failures can be attributed to lack of adhesion between NW/PR matrix and ITO, as well as, at ITO and Ti/Au interface. To reduce these defect, an adhesion layer can be incorporated at the NW/PR matrix and ITO interface. Additionally, the thickness of the Ti adhesion layer could be optimized to ease the delamination problem. By patterning the ITO film the global problems associated with contacting NWs can be localized. Furthermore, by improving the quality of the ITO film, the absorption and delamination challenges can be addressed.

Moreover, in the presented study, the doping concentrations are targeted values based on previous growth calibrations of GaAs planar film, wherein the thickness of film layers were measured by *in situ* emissivity-corrected pyrometry and doping concentrations were measured with Hall effect. These targeted values can be counted

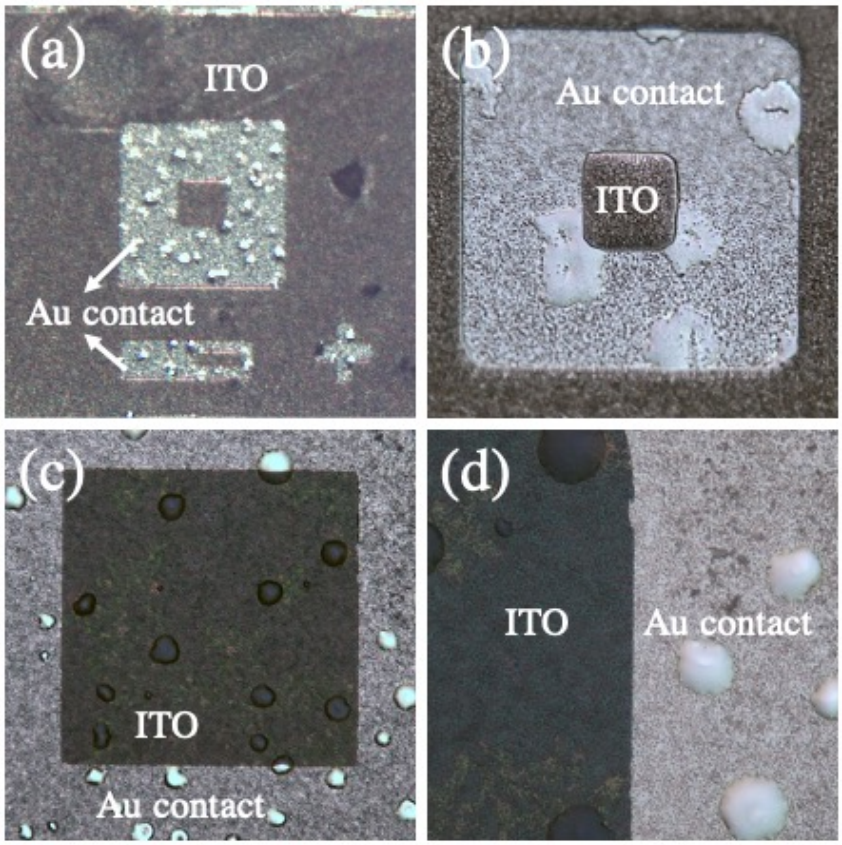

Figure 7.6: Optical images of SC devices showing blistering and delamination defects.

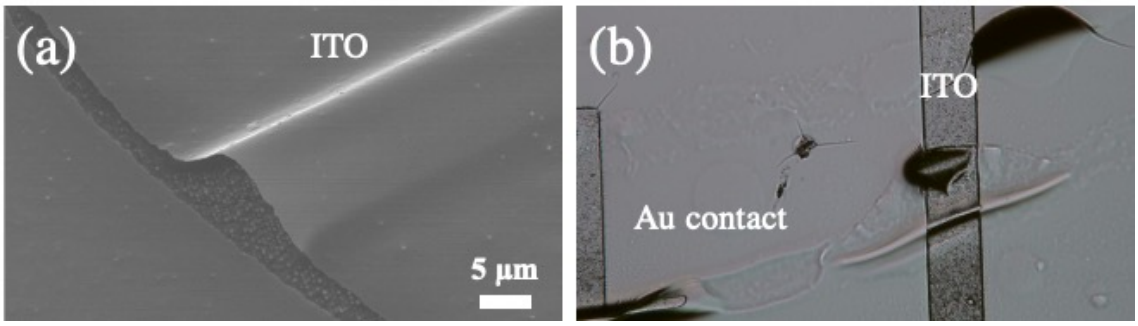

Figure 7.7: (a) 45°-tilted view SEM image after ITO deposition and anneal at 250 °C for 30 minutes, (b) Optical image of same sample as shown in panel (a), after Au deposition and lift-off.

as a fair estimation for doping concentrations in NWs core-shell hetrostructures. However, the difference in growth conditions between NWs SAE and planar films (i.e. growth temperature, V/III ratio and flowrates) suggests a possible divergence in the resulted doping concentrations of the two structrues. Therefore, the radial p-n junction in GaAsP-GaP heterostructure NWs could be independently investigated by mapping the doping profile of each segment. This allowss a more accurate design of growth parameter space for doping of core and shell segments.

Chapter 8

Research Products

8.1 Peer-Reviewed Publications

8.1.1 First-Author Publications

1. **M. A. Baboli**, M. A. Slocum, H. Kum, T. S. Wilhelm, S. J. Polly, S. M. Hubbard, and P. K. Mohseni, "Improving Pseudo-van der Waals Epitaxy of Self-Assembled InAs Nanowires on Graphene via MOCVD Parameter Space Mapping", *CrystEngComm* 21 (4), 602-615 (2019)

   **This work was selected as the back cover article of CrustEngComm, January (Issue 4), 2019.

2. **M. A. Baboli**, M. A. Slocum, A Giussani, S. M. Hubbard, and P. K. Mohseni, "Self-Assembled InAsP and lnAlAs Nanowires on Graphene Via Pseudo-Van Der Waals Epitaxy", *2018 IEEE 18th International Conference on Nanotechnology (IEEE-NANO)*, 1-5, (2018) (DOI: 10.1109/NANO.2018.8626308)

8.1.2 Co-Author Publications

1. T. S. Wilhelm, C. W. Soule, **M. A. Baboli**, C. J. O'Connell, and P. K. Mohseni, "Fabrication of Suspended III-V Nanofoils by Inverse Metal-Assisted Chemical Etching of $In_{0.49}Ga_{0.51}P$/GaAs Heteroepitaxial Films", *ACS Appl. Mater. Interfaces* 10 (2), 2058-2066 (2018)

2. T. S. Wilhelm, Z. Wang, **M. A. Baboli**, J. Yan, S. F. Preble, and P. K. Mohseni, "Ordered $Al_xGa_{1-x}As$ Nanopillar Arrays via Inverse Metal-Assisted Chemical Etching", *ACS Appl. Mater. Interfaces* 10 (32), 27488-27497 (2018)

3. D. Liu, S. J. Cho, J. H. Seo, K. Kim, M. Kim, J. Shi, X. Yin, W. Choi, C. Zhang, J. Kim, **M. A. Baboli** , J. Park, J. Bong, I. K. Lee, J. Gong, S. Mikael, J. H. Ryu, P. K Mohseni, X. Li, S. Gong, X. Wang, Z. Ma, "Lattice-mismatched semiconductor heterostructures", arXiv:1812.10225, 2018.

4. T. S. Wilhelm*, A. P. Kolberg*, **M. A. Baboli**, A. Abrand, K. A. Bertness, and P. K. Mohseni, "Black GaAs with Sub-Wavelength Nanostructures Fabricated via Lithography-Free Metal-Assisted Chemical Etching", *ECS J. Solid State Sci. Technol.* 8 (6) Q134-Q136 (2019)
   *Equal contribution authorship

5. T. S. Wilhelm*, I. L. Kecskes*, **M. A. Baboli**, A. Abrand, M. S. Pierce, B. J. Landi, I. Puchades, and P. K. Mohseni, "Fabrication of Ordered Si Micropillar Arrays via Carbon Nanotube-Assisted Chemical Etching", Submitted to *ACS Applied Nano Materials* on September 23, 2019, manuscript ID: an-2019-01838h
   *Equal contribution authorship

6. A. Fedorenko, **M. A. Baboli**, P. K. Mohseni, S. M. Hubbard,"Design and Simulation of the Bifacial III-V-Nanowire-on-Si Solar Cell", *MRS Advances* 1-8, (2019)

7. A. Fedorenko, **M. A. Baboli**, P. K. Mohseni, S. M. Hubbard,"Towards High-Efficiency Triple-Junction Bifacial III-V Nanowire-on-Silicon Solar Cells: Design Approaches Enabling the Concept", *2019 IEEE 46th Photovoltaic Specialists Conference (PVSC)* 3191-3194, (2019) (DOI: 10.1109/PVSC40753.2019.8981265)

8. D. Liu, S. J. Cho, A. Hardy, J. Kim, CJ. Herrera-Rodriguez, E. Swinnich, **M. A. Baboli**, J. Gong, X. Konstantinou, J. Papapolymerou, P.K. Mohseni, M. Becker, J.H. Seo, J.D. Albrecht, T. Grotjohn, Z. Ma,"Toward Diamond-Collector Heterojunction Bipolar Transistors via grafted GaAs-Diamond np junction", *2019 IEEE BiCMOS and Compound semiconductor Integrated Circuits and Technology Symposium (BCICTS)* 1-4 (2019) (DOI: 10.1109/BCICTS45179.2019.8972766)

Bibliography

[1] "Data.GISS: GISS Surface Temperature Analysis (v3): Analysis Graphs and Plots," https://data.giss.nasa.gov/gistemp/graphs/.

[2] C. Lesk, P. Rowhani, and N. Ramankutty, "Influence of extreme weather disasters on global crop production," *Nature*, vol. 529, no. 7584, pp. 84–87, Jan. 2016.

[3] M. Franchini and P. M. Mannucci, "Impact on human health of climate changes," *European Journal of Internal Medicine*, vol. 26, no. 1, pp. 1–5, Jan. 2015.

[4] J. Cook, D. Nuccitelli, S. A. Green, M. Richardson, B. Winkler, R. Painting, R. Way, P. Jacobs, and A. Skuce, "Quantifying the consensus on anthropogenic global warming in the scientific literature," *Environmental Research Letters*, vol. 8, no. 2, p. 024024, May 2013.

[5] J. Cook, N. Oreskes, P. T. Doran, W. R. L. Anderegg, B. Verheggen, E. W. Maibach, J. S. Carlton, S. Lewandowsky, A. G. Skuce, S. A. Green, D. Nuccitelli, P. Jacobs, M. Richardson, B. Winkler, R. Painting, and K. Rice, "Consensus on consensus: A synthesis of consensus estimates on human-caused global warming," *Environmental Research Letters*, vol. 11, no. 4, p. 048002, Apr. 2016.

[6] "Global Energy Transformation: A Roadmap to 2050," p. 76.

[7] F. Ise, "Photovoltaics Report," p. 47.

[8] "Solar Cells Market Size - Industry Share Analysis Report 2024," https://www.gminsights.com/industry-analysis/solar-cells-market.

[9] M. A. Green, Y. Hishikawa, E. D. Dunlop, D. H. Levi, J. Hohl-Ebinger, and A. W. Y. Ho-Baillie, "Solar cell efficiency tables (version 52)," *Progress in Photovoltaics: Research and Applications*, vol. 26, no. 7, pp. 427–436, 2018.

[10] A. D. Vos, "Detailed balance limit of the efficiency of tandem solar cells," *Journal of Physics D: Applied Physics*, vol. 13, no. 5, pp. 839–846, May 1980.

[11] B. Tian, X. Zheng, T. J. Kempa, Y. Fang, N. Yu, G. Yu, J. Huang, and C. M. Lieber, "Coaxial silicon nanowires as solar cells and nanoelectronic power sources," *Nature*, vol. 449, no. 7164, pp. 885–889, Oct. 2007.

[12] M. E. Reimer, G. Bulgarini, N. Akopian, M. Hocevar, M. B. Bavinck, M. A. Verheijen, E. P. Bakkers, L. P. Kouwenhoven, and V. Zwiller, "Bright single-photon sources in bottom-up tailored nanowires," *Nature communications*, vol. 3, p. 737, 2012.

[13] R. Yan, D. Gargas, and P. Yang, "Nanowire photonics," *Nature photonics*, vol. 3, no. 10, p. 569, 2009.

[14] R. Beanland, D. J. Dunstan, and P. J. Goodhew, "Plastic relaxation and relaxed buffer layers for semiconductor epitaxy," *Advances in Physics*, vol. 45, no. 2, pp. 87–146, 1996.

[15] J. F. Geisz, J. M. Olson, M. J. Romero, C. S. Jiang, and A. G. Norman, "Lattice-mismatched GaAsP solar cells grown on silicon by OMVPE," in *Photovoltaic Energy Conversion, Conference Record of the 2006 IEEE 4th World Conference On*, vol. 1. IEEE, 2006, pp. 772–775.

[16] J. F. Geisz, D. J. Friedman, J. S. Ward, A. Duda, W. J. Olavarria, T. E. Moriarty, J. T. Kiehl, M. J. Romero, A. G. Norman, and K. M. Jones, "40.8% efficient inverted triple-junction solar cell with two independently metamorphic junctions," *Applied Physics Letters*, vol. 93, no. 12, p. 123505, 2008.

[17] R. W. McClelland, C. O. Bozler, and J. C. C. Fan, "A technique for producing epitaxial films on reuseable substrates," *Applied Physics Letters*, vol. 37, no. 6, pp. 560–562, 1980.

[18] Y. Ujiie and T. Nishinaga, "Epitaxial lateral overgrowth of GaAs on a Si substrate," *Japanese Journal of Applied Physics*, vol. 28, no. 3A, p. L337, 1989.

[19] B.-Y. Tsaur, R. W. McClelland, J. C. Fan, R. P. Gale, J. P. Salerno, B. A. Vojak, and C. O. Bozler, "Low-dislocation-density GaAs epilayers grown on Ge-coated Si substrates by means of lateral epitaxial overgrowth," *Applied Physics Letters*, vol. 41, no. 4, pp. 347–349, 1982.

[20] J.-S. Park, J. Bai, M. Curtin, B. Adekore, M. Carroll, and A. Lochtefeld, "Defect reduction of selective Ge epitaxy in trenches on Si (001) substrates using aspect ratio trapping," *Applied Physics Letters*, vol. 90, no. 5, p. 052113, 2007.

[21] J. Bai, J.-S. Park, Z. Cheng, M. Curtin, B. Adekore, M. Carroll, A. Lochtefeld, and M. Dudley, "Study of the defect elimination mechanisms in aspect ratio trapping Ge growth," *Applied Physics Letters*, vol. 90, no. 10, p. 101902, 2007.

[22] J. Z. Li, J. Bai, J.-S. Park, B. Adekore, K. Fox, M. Carroll, A. Lochtefeld, and Z. Shellenbarger, "Defect reduction of GaAs epitaxy on Si (001) using selective aspect ratio trapping," *Applied physics letters*, vol. 91, no. 2, p. 021114, 2007.

[23] P. K. Mohseni, C. Maunders, G. A. Botton, and R. R. LaPierre, "GaP/GaAsP/GaP core–multishell nanowire heterostructures on (111) silicon," *Nanotechnology*, vol. 18, no. 44, p. 445304, 2007.

[24] T. M\a artensson, C. P. T. Svensson, B. A. Wacaser, M. W. Larsson, W. Seifert, K. Deppert, A. Gustafsson, L. R. Wallenberg, and L. Samuelson, "Epitaxial III-V nanowires on silicon," *Nano Letters*, vol. 4, no. 10, pp. 1987–1990, 2004.

[25] G. E. Cirlin, V. G. Dubrovskii, I. P. Soshnikov, N. V. Sibirev, Y. B. Samsonenko, A. D. Bouravleuv, J. C. Harmand, and F. Glas, "Critical diameters and

temperature domains for MBE growth of III–V nanowires on lattice mismatched substrates," *physica status solidi (RRL)-Rapid Research Letters*, vol. 3, no. 4, pp. 112–114, 2009.

[26] E. P. A. M. Bakkers, J. A. van Dam, S. D. Franceschi, L. P. Kouwenhoven, M. Kaiser, M. Verheijen, H. Wondergem, and P. van der Sluis, "Epitaxial growth of InP nanowires on germanium," *Nature Materials*, vol. 3, no. 11, pp. 769–773, Nov. 2004.

[27] S. Plissard, G. Larrieu, X. Wallart, and P. Caroff, "High yield of self-catalyzed GaAs nanowire arrays grown on silicon via gallium droplet positioning," *Nanotechnology*, vol. 22, no. 27, p. 275602, 2011.

[28] J. C. Shin, A. Lee, P. Katal Mohseni, D. Y. Kim, L. Yu, J. H. Kim, H. J. Kim, W. J. Choi, D. Wasserman, and K. J. Choi, "Wafer-Scale Production of Uniform InAs y P1–y Nanowire Array on Silicon for Heterogeneous Integration," *ACS nano*, vol. 7, no. 6, pp. 5463–5471, 2013.

[29] J. C. Shin, P. K. Mohseni, K. J. Yu, S. Tomasulo, K. H. Montgomery, M. L. Lee, J. A. Rogers, and X. Li, "Heterogeneous integration of InGaAs nanowires on the rear surface of Si solar cells for efficiency enhancement," *ACS nano*, vol. 6, no. 12, pp. 11 074–11 079, 2012.

[30] V. Dhaka, T. Haggren, H. Jussila, H. Jiang, E. Kauppinen, T. Huhtio, M. Sopanen, and H. Lipsanen, "High quality GaAs nanowires grown on glass substrates," *Nano letters*, vol. 12, no. 4, pp. 1912–1918, 2012.

[31] P. K. Mohseni, G. Lawson, A. Adronov, and R. R. LaPierre, "Hybrid GaAs-nanowire–carbon-nanotube flexible photovoltaics," *IEEE Journal of Selected Topics in Quantum Electronics*, vol. 17, no. 4, pp. 1070–1077, 2011.

[32] "Solar Spectral Irradiance: Air Mass 1.5," https://rredc.nrel.gov/solar//spectra/am1.5/.

[33] J. Wallentin, N. Anttu, D. Asoli, M. Huffman, I. Åberg, M. H. Magnusson, G. Siefer, P. Fuss-Kailuweit, F. Dimroth, B. Witzigmann, H. Q. Xu, L. Samuelson, K. Deppert, and M. T. Borgström, "InP Nanowire Array Solar Cells Achieving 13.8% Efficiency by Exceeding the Ray Optics Limit," *Science*, vol. 339, no. 6123, pp. 1057–1060, Mar. 2013.

[34] F. Qian, S. Gradečak, Y. Li, C.-Y. Wen, and C. M. Lieber, "Core/Multishell Nanowire Heterostructures as Multicolor, High-Efficiency Light-Emitting Diodes," *Nano Letters*, vol. 5, no. 11, pp. 2287–2291, Nov. 2005.

[35] A. C. Scofield, S.-H. Kim, J. N. Shapiro, A. Lin, B. Liang, A. Scherer, and D. L. Huffaker, "Bottom-up Photonic Crystal Lasers," *Nano Letters*, vol. 11, no. 12, pp. 5387–5390, Dec. 2011.

[36] Y. Zhang, J. Wu, M. Aagesen, and H. Liu, "III–V nanowires and nanowire optoelectronic devices," *Journal of Physics D: Applied Physics*, vol. 48, no. 46, p. 463001, Oct. 2015.

[37] N. Huang, C. Lin, and M. L. Povinelli, "Limiting efficiencies of tandem solar cells consisting of III-V nanowire arrays on silicon," *Journal of Applied Physics*, vol. 112, no. 6, p. 064321, Sep. 2012.

[38] J. C. Shin, K. H. Kim, K. J. Yu, H. Hu, L. Yin, C.-Z. Ning, J. A. Rogers, J.-M. Zuo, and X. Li, "InxGa1-xAs Nanowires on Silicon: One-Dimensional Heterogeneous Epitaxy, Bandgap Engineering, and Photovoltaics," *Nano Letters*, vol. 11, no. 11, pp. 4831–4838, Nov. 2011.

[39] J. V. Holm, H. I. Jørgensen, P. Krogstrup, J. Nygård, H. Liu, and M. Aagesen, "Surface-passivated GaAsP single-nanowire solar cells exceeding 10% efficiency grown on silicon," *Nature Communications*, vol. 4, p. 1498, Feb. 2013.

[40] N. Tajik, Z. Peng, P. Kuyanov, and R. R. LaPierre, "Sulfur passivation and contact methods for GaAs nanowire solar cells," *Nanotechnology*, vol. 22, no. 22, p. 225402, Apr. 2011.

[41] R. R. LaPierre, A. C. E. Chia, S. J. Gibson, C. M. Haapamaki, J. Boulanger, R. Yee, P. Kuyanov, J. Zhang, N. Tajik, N. Jewell, and K. M. A. Rahman, "III–V nanowire photovoltaics: Review of design for high efficiency," *physica status solidi (RRL) – Rapid Research Letters*, vol. 7, no. 10, pp. 815–830, 2013.

[42] R. R. LaPierre, M. Robson, K. M. Azizur-Rahman, and P. Kuyanov, "A review of III–V nanowire infrared photodetectors and sensors," *Journal of Physics D: Applied Physics*, vol. 50, no. 12, p. 123001, Feb. 2017.

[43] C. Zhang and X. Li, "III–V Nanowire Transistors for Low-Power Logic Applications: A Review and Outlook," *IEEE Transactions on Electron Devices*, vol. 63, no. 1, pp. 223–234, Jan. 2016.

[44] S. M. Vernon, V. E. Haven, S. P. Tobin, and R. G. Wolfson, "Metalorganic chemical vapor deposition of GaAs on Si for solar cell applications," *Journal of Crystal Growth*, vol. 77, no. 1, pp. 530–538, Sep. 1986.

[45] T. Soga, T. Kato, M. Yang, M. Umeno, and T. Jimbo, "High efficiency AlGaAs/Si monolithic tandem solar cell grown by metalorganic chemical vapor deposition," *Journal of Applied Physics*, vol. 78, no. 6, pp. 4196–4199, Sep. 1995.

[46] S. Almosni, C. Robert, T. Nguyen Thanh, C. Cornet, A. Létoublon, T. Quinci, C. Levallois, M. Perrin, J. Kuyyalil, L. Pedesseau, A. Balocchi, P. Barate, J. Even, J. M. Jancu, N. Bertru, X. Marie, O. Durand, and A. Le Corre, "Evaluation of InGaPN and GaAsPN materials lattice-matched to Si for multi-junction solar cells," *Journal of Applied Physics*, vol. 113, no. 12, p. 123509, Mar. 2013.

[47] B.-T. Tran, E.-Y. Chang, H.-D. Trinh, C.-T. Lee, K. C. Sahoo, K.-L. Lin, M.-C. Huang, H.-W. Yu, T.-T. Luong, C.-C. Chung, and C.-L. Nguyen, "Fabrication and characterization of n-In0.4Ga0.6N/p-Si solar cell," *Solar Energy Materials and Solar Cells*, vol. 102, pp. 208–211, Jul. 2012.

[48] E. Yablonovitch and G. D. Cody, "Intensity enhancement in textured optical sheets for solar cells," *IEEE Transactions on Electron Devices*, vol. 29, no. 2, pp. 300–305, 1982.

[49] Y. B. Bolkhovityanov and O. P. Pchelyakov, "GaAs epitaxy on Si substrates: Modern status of research and engineering," *Physics-Uspekhi*, vol. 51, no. 5, p. 437, 2008.

[50] G. W. Neudeck, *The PN Junction Diode*. Addison-Wesley, 1983, vol. 2.

[51] J. Merten, J. M. Asensi, C. Voz, A. V. Shah, R. Platz, and J. Andreu, "Improved equivalent circuit and analytical model for amorphous silicon solar cells and modules," *IEEE Transactions on electron devices*, vol. 45, no. 2, pp. 423–429, 1998.

[52] K. Nishioka, N. Sakitani, Y. Uraoka, and T. Fuyuki, "Analysis of multicrystalline silicon solar cells by modified 3-diode equivalent circuit model taking leakage current through periphery into consideration," *Solar Energy Materials and Solar Cells*, vol. 91, no. 13, pp. 1222–1227, 2007.

[53] J. S. You, D. Kim, J. Y. Huh, H. J. Park, J. J. Pak, and C. S. Kang, "Experiments on anisotropic etching of Si in TMAH," *Solar Energy Materials and Solar Cells*, vol. 66, no. 1, pp. 37–44, Feb. 2001.

[54] D. S. Ruby, S. H. Zaidi, S. Narayanan, B. M. Damiani, and A. Rohatgi, "Rie-texturing of multicrystalline silicon solar cells," *Solar Energy Materials and Solar Cells*, vol. 74, no. 1, pp. 133–137, Oct. 2002.

[55] Y.-T. Cheng, J.-J. Ho, S.-Y. Tsai, Z.-Z. Ye, W. Lee, D.-S. Hwang, S.-H. Chang, C.-C. Chang, and K. L. Wang, "Efficiency improved by acid texturization for multi-crystalline silicon solar cells," *Solar Energy*, vol. 85, no. 1, pp. 87–94, Jan. 2011.

[56] S. Sivasubramaniam and M. M. Alkaisi, "Inverted nanopyramid texturing for silicon solar cells using interference lithography," *Microelectronic Engineering*, vol. 119, pp. 146–150, May 2014.

[57] A. W. Smith and A. Rohatgi, "Ray tracing analysis of the inverted pyramid texturing geometry for high efficiency silicon solar cells," *Solar Energy Materials and Solar Cells*, vol. 29, no. 1, pp. 37–49, Feb. 1993.

[58] A. Mavrokefalos, S. E. Han, S. Yerci, M. S. Branham, and G. Chen, "Efficient Light Trapping in Inverted Nanopyramid Thin Crystalline Silicon Membranes

for Solar Cell Applications," *Nano Letters*, vol. 12, no. 6, pp. 2792–2796, Jun. 2012.

[59] J. Zhu, Z. Yu, S. Fan, and Y. Cui, "Nanostructured photon management for high performance solar cells," *Materials Science and Engineering: R: Reports*, vol. 70, no. 3, pp. 330–340, Nov. 2010.

[60] L. Tsakalakos, J. E. Balch, J. Fronheiser, M.-Y. Shih, S. F. LeBoeuf, M. Pietrzykowski, P. J. Codella, B. A. Korevaar, O. Sulima, J. Rand, A. Davuluru, and U. D. Rapol, "Strong broadband optical absorption in silicon nanowire films," *Journal of Nanophotonics*, vol. 1, no. 1, p. 013552, Jul. 2007.

[61] O. L. Muskens, J. G. Rivas, R. E. Algra, E. P. A. M. Bakkers, and A. Lagendijk, "Design of Light Scattering in Nanowire Materials for Photovoltaic Applications," *Nano Letters*, vol. 8, no. 9, pp. 2638–2642, Sep. 2008.

[62] S. L. Diedenhofen, G. Grzela, E. Haverkamp, G. Bauhuis, J. Schermer, and J. G. Rivas, "Broadband and omnidirectional anti-reflection layer for III/V multi-junction solar cells," *Solar Energy Materials and Solar Cells*, vol. 101, pp. 308–314, Jun. 2012.

[63] P. Hiralal, C. Chien, N. N. Lal, W. Abeygunasekara, A. Kumar, H. Butt, H. Zhou, H. Emrah Unalan, J. J. Baumberg, and G. A. J. Amaratunga, "Nanowire-based multifunctional antireflection coatings for solar cells," *Nanoscale*, vol. 6, no. 23, pp. 14 555–14 562, 2014.

[64] S. L. Diedenhofen, G. Vecchi, R. E. Algra, A. Hartsuiker, O. L. Muskens, G. Immink, E. P. A. M. Bakkers, W. L. Vos, and J. G. Rivas, "Broad-band and Omnidirectional Antireflection Coatings Based on Semiconductor Nanorods," *Advanced Materials*, vol. 21, no. 9, pp. 973–978, 2009.

[65] H. Guo, L. Wen, X. Li, Z. Zhao, and Y. Wang, "Analysis of optical absorption in GaAs nanowire arrays," *Nanoscale Research Letters*, vol. 6, no. 1, p. 617, Dec. 2011.

[66] X. Zhang, X.-H. Sun, H. Huang, X. Wang, Y. Huang, and X. Ren, "Optical absorption in InP/InGaAs/InP double-heterostructure nanopillar arrays for solar cells," *Applied Physics Letters*, vol. 104, no. 6, p. 061110, Feb. 2014.

[67] J. Tang, Z. Huo, S. Brittman, H. Gao, and P. Yang, "Solution-processed core–shell nanowires for efficient photovoltaic cells," *Nature Nanotechnology*, vol. 6, no. 9, pp. 568–572, Sep. 2011.

[68] K. P. Musselman, A. Marin, L. Schmidt-Mende, and J. L. MacManus-Driscoll, "Incompatible Length Scales in Nanostructured Cu2O Solar Cells," *Advanced Functional Materials*, vol. 22, no. 10, pp. 2202–2208, 2012.

[69] H. P. Yoon, Y. A. Yuwen, C. E. Kendrick, G. D. Barber, N. J. Podraza, J. M. Redwing, T. E. Mallouk, C. R. Wronski, and T. S. Mayer, "Enhanced conversion efficiencies for pillar array solar cells fabricated from crystalline silicon with short minority carrier diffusion lengths," *Applied Physics Letters*, vol. 96, no. 21, p. 213503, May 2010.

[70] J. D. Christesen, X. Zhang, C. W. Pinion, T. A. Celano, C. J. Flynn, and J. F. Cahoon, "Design Principles for Photovoltaic Devices Based on Si Nanowires with Axial or Radial p–n Junctions," *Nano Letters*, vol. 12, no. 11, pp. 6024–6029, Nov. 2012.

[71] B. M. Kayes, H. A. Atwater, and N. S. Lewis, "Comparison of the device physics principles of planar and radial p-n junction nanorod solar cells," *Journal of Applied Physics*, vol. 97, no. 11, p. 114302, May 2005.

[72] W. Shockley and H. J. Queisser, "Detailed Balance Limit of Efficiency of p-n Junction Solar Cells," *Journal of Applied Physics*, vol. 32, no. 3, pp. 510–519, Mar. 1961.

[73] W. Ruppel and P. Wurfel, "Upper limit for the conversion of solar energy," *IEEE Transactions on Electron Devices*, vol. 27, no. 4, pp. 877–882, Apr. 1980.

[74] U. Rau, U. W. Paetzold, and T. Kirchartz, "Thermodynamics of light management in photovoltaic devices," *Physical Review B*, vol. 90, no. 3, p. 035211, Jul. 2014.

[75] Y. Xu, T. Gong, and J. N. Munday, "The generalized Shockley-Queisser limit for nanostructured solar cells," *Scientific Reports*, vol. 5, p. 13536, Sep. 2015.

[76] L. C. Hirst and N. J. Ekins-Daukes, "Fundamental losses in solar cells," *Progress in Photovoltaics: Research and Applications*, vol. 19, no. 3, pp. 286–293, 2011.

[77] A. Polman and H. A. Atwater, "Photonic design principles for ultrahigh-efficiency photovoltaics," *Nature Materials*, vol. 11, pp. 174–177, Feb. 2012.

[78] J. Nelson, *The Physics of Solar Cells*. World Scientific Publishing Company, May 2003.

[79] E. Yablonovitch, "Statistical ray optics," *JOSA*, vol. 72, no. 7, pp. 899–907, Jul. 1982.

[80] D. M. Callahan, J. N. Munday, and H. A. Atwater, "Solar Cell Light Trapping beyond the Ray Optic Limit," *Nano Letters*, vol. 12, no. 1, pp. 214–218, Jan. 2012.

[81] P. Würfel, S. Finkbeiner, and E. Daub, "Generalized Planck's radiation law for luminescence via indirect transitions," *Applied Physics A*, vol. 60, no. 1, pp. 67–70, Jan. 1995.

[82] A. Luque and S. Hegedus, *Handbook of Photovoltaic Science and Engineering*. John Wiley & Sons, Mar. 2011.

[83] I. Åberg, G. Vescovi, D. Asoli, U. Naseem, J. P. Gilboy, C. Sundvall, A. Dahlgren, K. E. Svensson, N. Anttu, M. T. Björk, and L. Samuelson, "A GaAs Nanowire Array Solar Cell With 15.3% Efficiency at 1 Sun," *IEEE Journal of Photovoltaics*, vol. 6, no. 1, pp. 185–190, Jan. 2016.

[84] D. van Dam, N. J. J. van Hoof, Y. Cui, P. J. van Veldhoven, E. P. A. M. Bakkers, J. Gómez Rivas, and J. E. M. Haverkort, "High-Efficiency Nanowire Solar Cells with Omnidirectionally Enhanced Absorption Due to Self-Aligned Indium–Tin–Oxide Mie Scatterers," *ACS Nano*, vol. 10, no. 12, pp. 11 414–11 419, Dec. 2016.

[85] I. Hwang, H.-D. Um, B.-S. Kim, M. Wober, and K. Seo, "Flexible crystalline silicon radial junction photovoltaics with vertically aligned tapered microwires," *Energy & Environmental Science*, vol. 11, no. 3, pp. 641–647, 2018.

[86] J. V. Holm, M. Aagesen, Y. Zhang, J. Wu, S. Hatch, and H. Liu, "Bandgap optimized III–V (GaAsP) nanowire on silicon tandem solar cell, device and data," in *2014 IEEE 40th Photovoltaic Specialist Conference (PVSC)*, Jun. 2014, pp. 1041–1044.

[87] G. Mariani, P.-S. Wong, A. M. Katzenmeyer, F. Léonard, J. Shapiro, and D. L. Huffaker, "Patterned Radial GaAs Nanopillar Solar Cells," *Nano Letters*, vol. 11, no. 6, pp. 2490–2494, Jun. 2011.

[88] G. Mariani, A. C. Scofield, C.-H. Hung, and D. L. Huffaker, "GaAs nanopillar-array solar cells employing *in situ* surface passivation," *Nature Communications*, vol. 4, p. 1497, Feb. 2013.

[89] A. Nowzari, M. Heurlin, V. Jain, K. Storm, A. Hosseinnia, N. Anttu, M. T. Borgström, H. Pettersson, and L. Samuelson, "A Comparative Study of Absorption in Vertically and Laterally Oriented InP Core–Shell Nanowire Photovoltaic Devices," *Nano Letters*, vol. 15, no. 3, pp. 1809–1814, Mar. 2015.

[90] J. P. Boulanger, A. C. E. Chia, B. Wood, S. Yazdi, T. Kasama, M. Aagesen, and R. R. LaPierre, "Characterization of a Ga-Assisted GaAs Nanowire Array Solar Cell on Si Substrate," *IEEE Journal of Photovoltaics*, vol. 6, no. 3, pp. 661–667, May 2016.

[91] H. Goto, K. Nosaki, K. Tomioka, S. Hara, K. Hiruma, J. Motohisa, and T. Fukui, "Growth of Core–Shell InP Nanowires for Photovoltaic Application by Selective-Area Metal Organic Vapor Phase Epitaxy," *Applied Physics Express*, vol. 2, no. 3, p. 035004, Feb. 2009.

[92] T. Fukui, M. Yoshimura, E. Nakai, and K. Tomioka, "Position-Controlled III–V Compound Semiconductor Nanowire Solar Cells by Selective-Area Metal–Organic Vapor Phase Epitaxy," *AMBIO*, vol. 41, no. 2, pp. 119–124, Mar. 2012.

[93] G. B. Stringfellow, *Organometallic Vapor-Phase Epitaxy: Theory and Practice*. Elsevier, Mar. 1999.

[94] M. R. Islam, R. V. Chelakaea, J. G. Neff, K. G. Fertitta, P. A. Grudowski, A. L. Holmes, F. J. Ciuba, R. D. Dupuis, and J. E. Fouquet, "The growth and characterization of AlGaAs double heterostructures for the evaluation of reactor and source quality," *Journal of Electronic Materials*, vol. 24, no. 6, pp. 787–792, Jun. 1995.

[95] L. Yang, J. Motohisa, J. Takeda, K. Tomioka, and T. Fukui, "Selective-area growth of hexagonal nanopillars with single InGaAs/GaAs quantum wells on GaAs(111)B substrate and their temperature-dependent photoluminescence," *Nanotechnology*, vol. 18, no. 10, p. 105302, Jan. 2007.

[96] D. K. Schroder, *Semiconductor Material and Device Characterization*. John Wiley & Sons, 2006.

[97] C. A. Volkert and A. M. Minor, "Focused Ion Beam Microscopy and Micromachining," *MRS Bulletin*, vol. 32, no. 05, pp. 389–399, May 2007.

[98] A. Koma, "Van der Waals epitaxy for highly lattice-mismatched systems," *Journal of Crystal Growth*, vol. 201-202, pp. 236–241, May 1999.

[99] P. K. Mohseni, A. Behnam, J. D. Wood, X. Zhao, K. J. Yu, N. C. Wang, A. Rockett, J. A. Rogers, J. W. Lyding, and E. Pop, "Monolithic III-V nanowire solar cells on graphene via direct van der waals epitaxy," *Advanced Materials*, vol. 26, no. 22, pp. 3755–3760, 2014.

[100] A. M. Munshi, D. L. Dheeraj, V. T. Fauske, D.-C. Kim, A. T. J. van Helvoort, B.-O. Fimland, and H. Weman, "Vertically Aligned GaAs Nanowires on Graphite and Few-Layer Graphene: Generic Model and Epitaxial Growth," *Nano Letters*, vol. 12, no. 9, pp. 4570–4576, Sep. 2012.

[101] Y. J. Hong, W. H. Lee, Y. Wu, R. S. Ruoff, and T. Fukui, "Van der Waals Epitaxy of InAs Nanowires Vertically Aligned on Single-Layer Graphene," *Nano Letters*, vol. 12, no. 3, pp. 1431–1436, Mar. 2012.

[102] J. Wallentin, D. Kriegner, J. Stangl, and M. T. Borgström, "Au-Seeded Growth of Vertical and in-Plane III–V Nanowires on Graphite Substrates," *Nano Letters*, vol. 14, no. 4, pp. 1707–1713, Apr. 2014.

[103] Y. J. Hong and T. Fukui, "Controlled van der Waals heteroepitaxy of InAs nanowires on carbon honeycomb lattices," *ACS nano*, vol. 5, no. 9, pp. 7576–7584, 2011.

[104] E. A. Anyebe, A. M. Sanchez, S. Hindmarsh, X. Chen, J. Shao, M. K. Rajpalke, T. D. Veal, B. J. Robinson, O. Kolosov, F. Anderson, R. Sundaram, Z. M. Wang, V. Falko, and Q. Zhuang, "Realization of Vertically Aligned, Ultrahigh

Aspect Ratio InAsSb Nanowires on Graphite," *Nano Letters*, vol. 15, no. 7, pp. 4348–4355, Jul. 2015.

[105] E. A. Anyebe, I. Sandall, Z. M. Jin, A. M. Sanchez, M. K. Rajpalke, T. D. Veal, Y. C. Cao, H. Li, R. Harvey, and Q. D. Zhuang, "Optimization of self-catalyzed InAs Nanowires on flexible graphite for photovoltaic infrared photodetectors," *Scientific Reports*, vol. 7, p. 46110, 2017.

[106] A. Mazid Munshi and H. Weman, "Advances in semiconductor nanowire growth on graphene," *physica status solidi (RRL)-Rapid Research Letters*, vol. 7, no. 10, pp. 713–726, 2013.

[107] Y. Alaskar, S. Arafin, D. Wickramaratne, M. A. Zurbuchen, L. He, J. McKay, Q. Lin, M. S. Goorsky, R. K. Lake, and K. L. Wang, "Towards van der Waals epitaxial growth of GaAs on Si using a graphene buffer layer," *Advanced Functional Materials*, vol. 24, no. 42, pp. 6629–6638, 2014.

[108] V. Kumaresan, L. Largeau, A. Madouri, F. Glas, H. Zhang, F. Oehler, A. Cavanna, A. Babichev, L. Travers, and N. Gogneau, "Epitaxy of GaN nanowires on graphene," *Nano letters*, vol. 16, no. 8, pp. 4895–4902, 2016.

[109] P. K. Mohseni, A. Behnam, J. D. Wood, C. D. English, J. W. Lyding, E. Pop, and X. Li, "InxGa1–xAs Nanowire Growth on Graphene: Van der Waals Epitaxy Induced Phase Segregation," *Nano Letters*, vol. 13, no. 3, pp. 1153–1161, Mar. 2013.

[110] G. Fiori, F. Bonaccorso, G. Iannaccone, T. Palacios, D. Neumaier, A. Seabaugh, S. K. Banerjee, and L. Colombo, "Electronics based on two-dimensional materials," *Nature Nanotechnology*, vol. 9, no. 10, pp. 768–779, Oct. 2014.

[111] F. H. L. Koppens, T. Mueller, P. Avouris, A. C. Ferrari, M. S. Vitiello, and M. Polini, "Photodetectors based on graphene, other two-dimensional materials and hybrid systems," *Nature nanotechnology*, vol. 9, no. 10, p. 780, 2014.

[112] A. Pospischil, M. M. Furchi, and T. Mueller, "Solar-energy conversion and light emission in an atomic monolayer pn diode," *Nature nanotechnology*, vol. 9, no. 4, pp. 257–261, 2014.

[113] M.-L. Tsai, M.-Y. Li, J. R. D. Retamal, K.-T. Lam, Y.-C. Lin, K. Suenaga, L.-J. Chen, G. Liang, L.-J. Li, and H. He Jr, "Single Atomically Sharp Lateral Monolayer p-n Heterojunction Solar Cells with Extraordinarily High Power Conversion Efficiency," *Advanced Materials*, vol. 29, no. 32, 2017.

[114] F. Xia, H. Wang, D. Xiao, M. Dubey, and A. Ramasubramaniam, "Two-dimensional material nanophotonics," *Nature Photonics*, vol. 8, no. 12, p. 899, 2014.

[115] F. Ning, D. Wang, Y.-X. Feng, L.-M. Tang, Y. Zhang, and K.-Q. Chen, "Strong interfacial interaction and enhanced optical absorption in graphene/InAs and MoS 2/InAs heterostructures," *Journal of Materials Chemistry C*, vol. 5, no. 36, pp. 9429–9438, 2017.

[116] C. Yelgel, G. P. Srivastava, and R. H. Miwa, "Ab initio investigation of the electronic properties of graphene on InAs (111) A," *Journal of Physics: Condensed Matter*, vol. 24, no. 48, p. 485004, 2012.

[117] K. T. Chan, J. B. Neaton, and M. L. Cohen, "First-principles study of metal adatom adsorption on graphene," *Physical Review B*, vol. 77, no. 23, p. 235430, Jun. 2008.

[118] K. Nakada and A. Ishii, "Migration of adatom adsorption on graphene using DFT calculation," *Solid State Communications*, vol. 151, no. 1, pp. 13–16, 2011.

[119] Y. J. Hong, J. W. Yang, W. H. Lee, R. S. Ruoff, K. S. Kim, and T. Fukui, "Van der Waals epitaxial double heterostructure: InAs/single-layer graphene/InAs," *Advanced Materials*, vol. 25, no. 47, pp. 6847–6853, 2013.

[120] J. Miao, W. Hu, N. Guo, Z. Lu, X. Liu, L. Liao, P. Chen, T. Jiang, S. Wu, and J. C. Ho, "High-Responsivity Graphene/InAs Nanowire Heterojunction Near-Infrared Photodetectors with Distinct Photocurrent On/Off Ratios," *small*, vol. 11, no. 8, pp. 936–942, 2015.

[121] M. A. Baboli, M. A. Slocum, A. Giussani, S. M. Hubbard, and P. K. Mohseni, "Self-Assembled InAsP and InAlAs Nanowires on Graphene via Pseudo-van der Waals Epitaxy," in *18th IEEE International Conference on Nanotechnology*, 2018.

[122] C. A. Larsen, N. I. Buchan, and G. B. Stringfellow, "Reaction mechanisms in the organometallic vapor phase epitaxial growth of GaAs," *Applied physics letters*, vol. 52, no. 6, pp. 480–482, 1988.

[123] U. P. Gomes, D. Ercolani, N. V. Sibirev, M. Gemmi, V. G. Dubrovskii, F. Beltram, and L. Sorba, "Catalyst-free growth of InAs nanowires on Si (111) by CBE," *Nanotechnology*, vol. 26, no. 41, p. 415604, 2015.

[124] U. P. Gomes, D. Ercolani, V. Zannier, J. David, M. Gemmi, F. Beltram, and L. Sorba, "Nucleation and growth mechanism of self-catalyzed InAs nanowires on silicon," *Nanotechnology*, vol. 27, no. 25, p. 255601, 2016.

[125] T. Grap, T. Rieger, C. Blömers, T. Schäpers, D. Grützmacher, and M. I. Lepsa, "Self-catalyzed VLS grown InAs nanowires with twinning superlattices," *Nanotechnology*, vol. 24, no. 33, p. 335601, 2013.

[126] S. A. Dayeh, E. T. Yu, and D. Wang, "III- V nanowire growth mechanism: V/III ratio and temperature effects," *Nano letters*, vol. 7, no. 8, pp. 2486–2490, 2007.

[127] G. Koblmüller, S. Hertenberger, K. Vizbaras, M. Bichler, F. Bao, J. P. Zhang, and G. Abstreiter, "Self-induced growth of vertical free-standing InAs nanowires on Si (111) by molecular beam epitaxy," *Nanotechnology*, vol. 21, no. 36, p. 365602, 2010.

[128] P. Paiano, P. Prete, N. Lovergine, and A. M. Mancini, "Size and shape control of GaAs nanowires grown by metalorganic vapor phase epitaxy using tertiarybutylarsine," *Journal of applied physics*, vol. 100, no. 9, p. 094305, 2006.

[129] S. A. Fortuna, J. Wen, I. S. Chun, and X. Li, "Planar GaAs nanowires on GaAs (100) substrates: Self-aligned, nearly twin-defect free, and transfer-printable," *Nano Letters*, vol. 8, no. 12, pp. 4421–4427, 2008.

[130] K. A. Dick, K. Deppert, L. S. Karlsson, L. R. Wallenberg, L. Samuelson, and W. Seifert, "A new understanding of Au-assisted growth of III–V semiconductor nanowires," *Advanced Functional Materials*, vol. 15, no. 10, pp. 1603–1610, 2005.

[131] S. N. Mohammad, "General theoretical model for the vapor-phase growth and growth rate of semiconductor nanowires," *Journal of Vacuum Science & Technology B, Nanotechnology and Microelectronics: Materials, Processing, Measurement, and Phenomena*, vol. 28, no. 2, pp. 329–352, 2010.

[132] K. A. Dick, J. Bolinsson, M. E. Messing, S. Lehmann, J. Johansson, and P. Caroff, "Parameter space mapping of InAs nanowire crystal structure," *Journal of Vacuum Science & Technology B, Nanotechnology and Microelectronics: Materials, Processing, Measurement, and Phenomena*, vol. 29, no. 4, p. 04D103, 2011.

[133] K. A. Dick, P. Caroff, J. Bolinsson, M. E. Messing, J. Johansson, K. Deppert, L. R. Wallenberg, and L. Samuelson, "Control of III–V nanowire crystal structure by growth parameter tuning," *Semiconductor Science and Technology*, vol. 25, no. 2, p. 024009, 2010.

[134] N. I. Buchan, C. A. Larsen, and G. B. Stringfellow, "Mass spectrometric studies of trimethylindium pyrolysis," *Journal of Crystal Growth*, vol. 92, no. 3-4, pp. 591–604, 1988.

[135] F. Glas, J.-C. Harmand, and G. Patriarche, "Why does wurtzite form in nanowires of III-V zinc blende semiconductors?" *Physical review letters*, vol. 99, no. 14, p. 146101, 2007.

[136] V. G. Dubrovskii and N. V. Sibirev, "Growth thermodynamics of nanowires and its application to polytypism of zinc blende III-V nanowires," *Physical review B*, vol. 77, no. 3, p. 035414, 2008.

[137] V. G. Dubrovskii, N. V. Sibirev, J. C. Harmand, and F. Glas, "Growth kinetics and crystal structure of semiconductor nanowires," *Physical Review B*, vol. 78, no. 23, p. 235301, 2008.

[138] D. L. Dheeraj, G. Patriarche, H. Zhou, T. B. Hoang, A. F. Moses, S. Grønsberg, A. T. van Helvoort, B.-O. Fimland, and H. Weman, "Growth and characterization of wurtzite GaAs nanowires with defect-free zinc blende GaAsSb inserts," *Nano letters*, vol. 8, no. 12, pp. 4459–4463, 2008.

[139] P. Caroff, K. A. Dick, J. Johansson, M. E. Messing, K. Deppert, and L. Samuelson, "Controlled polytypic and twin-plane superlattices in III–V nanowires," *Nature nanotechnology*, vol. 4, no. 1, p. 50, 2009.

[140] S. Lehmann, J. Wallentin, D. Jacobsson, K. Deppert, and K. A. Dick, "A general approach for sharp crystal phase switching in InAs, GaAs, InP, and GaP nanowires using only group V flow," *Nano letters*, vol. 13, no. 9, pp. 4099–4105, 2013.

[141] M. Li, J. Wang, K. Li, Y. Xing, and H. Q. Xu, "Growth of InAs nanowires with the morphology and crystal structure controlled by carrier gas flow rate," *Journal of Crystal Growth*, vol. 430, pp. 87–92, 2015.

[142] Z. Zhang, Z. Lu, H. Xu, P. Chen, W. Lu, and J. Zou, "Structure and quality controlled growth of InAs nanowires through catalyst engineering," *Nano Research*, vol. 7, no. 11, pp. 1640–1649, 2014.

[143] J. Bao, D. C. Bell, F. Capasso, N. Erdman, D. Wei, L. Fröberg, T. M\a artensson, and L. Samuelson, "Nanowire-Induced Wurtzite InAs Thin Film on Zinc-Blende InAs Substrate," *Advanced Materials*, vol. 21, no. 36, pp. 3654–3658, 2009.

[144] K. Tomioka, J. Motohisa, S. Hara, and T. Fukui, "Crystallographic structure of InAs nanowires studied by transmission electron microscopy," *Japanese Journal of Applied Physics*, vol. 46, no. 12L, p. L1102, 2007.

[145] ——, "Control of InAs nanowire growth directions on Si," *Nano letters*, vol. 8, no. 10, pp. 3475–3480, 2008.

[146] K. Tomioka, F. Izhizaka, and T. Fukui, "Selective-area growth of InAs nanowires on Ge and vertical transistor application," *Nano letters*, vol. 15, no. 11, pp. 7253–7257, 2015.

[147] H. Paetzelt, V. Gottschalch, J. Bauer, G. Benndorf, and G. Wagner, "Selective-area growth of GaAs and InAs nanowires—homo-and heteroepitaxy using SiNx templates," *Journal of Crystal Growth*, vol. 310, no. 23, pp. 5093–5097, 2008.

[148] J. C. Shin, K. H. Kim, K. J. Yu, H. Hu, L. Yin, C.-Z. Ning, J. A. Rogers, J.-M. Zuo, and X. Li, "In x Ga1-x As Nanowires on Silicon: One-Dimensional Heterogeneous Epitaxy, Bandgap Engineering, and Photovoltaics," *Nano letters*, vol. 11, no. 11, pp. 4831–4838, 2011.

[149] M. T. Robson and R. R. LaPierre, "InAs nanowire growth modes on Si (111) by gas source molecular beam epitaxy," *Journal of Crystal Growth*, vol. 436, pp. 1–11, 2016.

[150] M. Borg, H. Schmid, K. E. Moselund, G. Signorello, L. Gignac, J. Bruley, C. Breslin, P. Das Kanungo, P. Werner, and H. Riel, "Vertical III–V nanowire device integration on Si (100)," *Nano letters*, vol. 14, no. 4, pp. 1914–1920, 2014.

[151] J. Becker, M. O. Hill, M. Sonner, J. Treu, M. Döblinger, A. Hirler, H. Riedl, J. J. Finley, L. Lauhon, and G. Koblmüller, "Correlated Chemical and Electrically Active Dopant Analysis in Catalyst-Free Si-Doped InAs Nanowires," *ACS nano*, vol. 12, no. 2, pp. 1603–1610, 2018.

[152] E. Dimakis, M. Ramsteiner, C.-N. Huang, A. Trampert, A. Davydok, A. Biermanns, U. Pietsch, H. Riechert, and L. Geelhaar, "In situ doping of catalyst-free InAs nanowires with Si: Growth, polytypism, and local vibrational modes of Si," *Applied Physics Letters*, vol. 103, no. 14, p. 143121, 2013.

[153] S. Wirths, K. Weis, A. Winden, K. Sladek, C. Volk, S. Alagha, T. E. Weirich, M. von der Ahe, H. Hardtdegen, and H. Lüth, "Effect of Si-doping on InAs nanowire transport and morphology," *Journal of applied physics*, vol. 110, no. 5, p. 053709, 2011.

[154] X. Ji, X. Yang, W. Du, H. Pan, and T. Yang, "Selective-area MOCVD growth and carrier-transport-type control of InAs (Sb)/GaSb core–shell nanowires," *Nano letters*, vol. 16, no. 12, pp. 7580–7587, 2016.

[155] M. T. Soo, K. Zheng, Q. Gao, H. H. Tan, C. Jagadish, and J. Zou, "Growth of catalyst-free epitaxial InAs nanowires on Si wafers using metallic masks," *Nano letters*, vol. 16, no. 7, pp. 4189–4193, 2016.

[156] Z. Liu, C. Merckling, R. Rooyackers, O. Richard, H. Bender, Y. Mols, M. Vila, J. Rubio-Zuazo, G. R. Castro, and N. Collaert, "Correlation between surface reconstruction and polytypism in InAs nanowire selective area epitaxy," *Physical Review Materials*, vol. 1, no. 7, p. 074603, 2017.

[157] S. Hertenberger, D. Rudolph, M. Bichler, J. J. Finley, G. Abstreiter, and G. Koblmüller, "Growth kinetics in position-controlled and catalyst-free InAs nanowire arrays on Si (111) grown by selective area molecular beam epitaxy," *Journal of Applied Physics*, vol. 108, no. 11, p. 114316, 2010.

[158] M. T. Björk, H. Schmid, C. M. Breslin, L. Gignac, and H. Riel, "InAs nanowire growth on oxide-masked< 111> silicon," *Journal of crystal growth*, vol. 344, no. 1, pp. 31–37, 2012.

[159] M. A. Baboli, M. A. Slocum, H. Kum, T. S. Wilhelm, S. J. Polly, S. M. Hubbard, and P. K. Mohseni, "Improving pseudo-van der Waals epitaxy of self-assembled InAs nanowires on graphene via MOCVD parameter space mapping," *CrystEngComm*, vol. 21, no. 4, pp. 602–615, Jan. 2019.

[160] D. W. Squire, C. S. Dulcey, and M. C. Lin, "Mechanistic studies of the decomposition of trimethylaluminum on heated surfaces," *Journal of Vacuum Science*

& Technology B: Microelectronics Processing and Phenomena, vol. 3, no. 5, pp. 1513–1519, Sep. 1985.

[161] C. Agert, P. Lanyi, and A. W. Bett, "MOVPE of GaSb, (AlGa)Sb and (AlGa)(AsSb) in a multiwafer planetary reactor," *Journal of Crystal Growth*, vol. 225, no. 2, pp. 426–430, May 2001.

[162] D. Jariwala, V. K. Sangwan, L. J. Lauhon, T. J. Marks, and M. C. Hersam, "Emerging Device Applications for Semiconducting Two-Dimensional Transition Metal Dichalcogenides," *ACS Nano*, vol. 8, no. 2, pp. 1102–1120, Feb. 2014.

[163] J. A. Wilson, F. J. Di Salvo, and S. Mahajan, "Charge-Density Waves in Metallic, Layered, Transition-Metal Dichalcogenides," *Physical Review Letters*, vol. 32, no. 16, pp. 882–885, Apr. 1974.

[164] G. H. Han, D. L. Duong, D. H. Keum, S. J. Yun, and Y. H. Lee, "Van der Waals Metallic Transition Metal Dichalcogenides," *Chemical Reviews*, vol. 118, no. 13, pp. 6297–6336, Jul. 2018.

[165] T. Shishidou, A. J. Freeman, and R. Asahi, "Effect of GGA on the half-metallicity of the itinerant ferromagnet ${\mathrm{CoS}}_{2}$," *Physical Review B*, vol. 64, no. 18, p. 180401, Oct. 2001.

[166] B. Radisavljevic, A. Radenovic, J. Brivio, V. Giacometti, and A. Kis, "Single-layer MoS 2 transistors," *Nature Nanotechnology*, vol. 6, no. 3, pp. 147–150, Mar. 2011.

[167] K. Taniguchi, A. Matsumoto, H. Shimotani, and H. Takagi, "Electric-field-induced superconductivity at 9.4 K in a layered transition metal disulphide MoS2," *Applied Physics Letters*, vol. 101, no. 4, p. 042603, Jul. 2012.

[168] A. Sajedi-Moghaddam, C. C. Mayorga-Martinez, E. Saievar-Iranizad, Z. Sofer, and M. Pumera, "Exfoliated transition metal dichalcogenide (MX2; M=Mo, W; X=S, Se, Te) nanosheets and their composites with polyaniline nanofibers for electrochemical capacitors," *Applied Materials Today*, vol. 16, pp. 280–289, Sep. 2019.

[169] K.-A. N. Duerloo, Y. Li, and E. J. Reed, "Structural phase transitions in two-dimensional Mo- and W-dichalcogenide monolayers," *Nature Communications*, vol. 5, no. 1, pp. 1–9, Jul. 2014.

[170] H. Zeng, G.-B. Liu, J. Dai, Y. Yan, B. Zhu, R. He, L. Xie, S. Xu, X. Chen, W. Yao, and X. Cui, "Optical signature of symmetry variations and spin-valley coupling in atomically thin tungsten dichalcogenides," *Scientific Reports*, vol. 3, no. 1, pp. 1–5, Apr. 2013.

[171] H. Schmidt, S. Wang, L. Chu, M. Toh, R. Kumar, W. Zhao, A. H. Castro Neto, J. Martin, S. Adam, B. Özyilmaz, and G. Eda, "Transport Properties of Monolayer MoS2 Grown by Chemical Vapor Deposition," *Nano Letters*, vol. 14, no. 4, pp. 1909–1913, Apr. 2014.

[172] A. Splendiani, L. Sun, Y. Zhang, T. Li, J. Kim, C.-Y. Chim, G. Galli, and F. Wang, "Emerging Photoluminescence in Monolayer MoS2," *Nano Letters*, vol. 10, no. 4, pp. 1271–1275, Apr. 2010.

[173] J. Kang, W. Liu, and K. Banerjee, "High-performance MoS2 transistors with low-resistance molybdenum contacts," *Applied Physics Letters*, vol. 104, no. 9, p. 093106, Mar. 2014.

[174] M. Amani, M. L. Chin, A. G. Birdwell, T. P. O'Regan, S. Najmaei, Z. Liu, P. M. Ajayan, J. Lou, and M. Dubey, "Electrical performance of monolayer MoS2 field-effect transistors prepared by chemical vapor deposition," *Applied Physics Letters*, vol. 102, no. 19, p. 193107, May 2013.

[175] R. Cheng, D. Li, H. Zhou, C. Wang, A. Yin, S. Jiang, Y. Liu, Y. Chen, Y. Huang, and X. Duan, "Electroluminescence and Photocurrent Generation from Atomically Sharp WSe2/MoS2 Heterojunction p–n Diodes," *Nano Letters*, vol. 14, no. 10, pp. 5590–5597, Oct. 2014.

[176] O. Lopez-Sanchez, D. Lembke, M. Kayci, A. Radenovic, and A. Kis, "Ultrasensitive photodetectors based on monolayer MoS_2," *Nature Nanotechnology*, vol. 8, no. 7, pp. 497–501, Jul. 2013.

[177] M.-L. Tsai, S.-H. Su, J.-K. Chang, D.-S. Tsai, C.-H. Chen, C.-I. Wu, L.-J. Li, L.-J. Chen, and J.-H. He, "Monolayer MoS2 Heterojunction Solar Cells," *ACS Nano*, vol. 8, no. 8, pp. 8317–8322, Aug. 2014.

[178] X. Zhou, N. Zhou, C. Li, H. Song, Q. Zhang, X. Hu, L. Gan, H. Li, J. Lü, J. Luo, J. Xiong, and T. Zhai, "Vertical heterostructures based on SnSe 2 /MoS 2 for high performance photodetectors," *2D Materials*, vol. 4, no. 2, p. 025048, Mar. 2017.

[179] M. Long, E. Liu, P. Wang, A. Gao, H. Xia, W. Luo, B. Wang, J. Zeng, Y. Fu, K. Xu, W. Zhou, Y. Lv, S. Yao, M. Lu, Y. Chen, Z. Ni, Y. You, X. Zhang, S. Qin, Y. Shi, W. Hu, D. Xing, and F. Miao, "Broadband Photovoltaic Detectors Based on an Atomically Thin Heterostructure," *Nano Letters*, vol. 16, no. 4, pp. 2254–2259, Apr. 2016.

[180] L. Ye, H. Li, Z. Chen, and J. Xu, "Near-Infrared Photodetector Based on MoS2/Black Phosphorus Heterojunction," *ACS Photonics*, vol. 3, no. 4, pp. 692–699, Apr. 2016.

[181] Y. Liu, Y. Huang, and X. Duan, "Van der Waals integration before and beyond two-dimensional materials," *Nature*, vol. 567, no. 7748, pp. 323–333, Mar. 2019.

[182] D. Jariwala, T. J. Marks, and M. C. Hersam, "Mixed-dimensional van der Waals heterostructures," *Nature Materials*, vol. 16, no. 2, pp. 170–181, Feb. 2017.

[183] Y. Zhang, J. Wu, M. Aagesen, and H. Liu, "III–V nanowires and nanowire optoelectronic devices," *Journal of Physics D: Applied Physics*, vol. 48, no. 46, p. 463001, 2015.

[184] K. Tomioka, M. Yoshimura, and T. Fukui, "A III–V nanowire channel on silicon for high-performance vertical transistors," *Nature*, vol. 488, no. 7410, p. 189, 2012.

[185] K. S. Novoselov, A. K. Geim, S. V. Morozov, D. Jiang, Y. Zhang, S. V. Dubonos, I. V. Grigorieva, and A. A. Firsov, "Electric Field Effect in Atomically Thin Carbon Films," *Science*, vol. 306, no. 5696, pp. 666–669, Oct. 2004.

[186] A. M. Munshi and H. Weman, "Advances in semiconductor nanowire growth on graphene," *physica status solidi (RRL) – Rapid Research Letters*, vol. 7, no. 10, pp. 713–726, 2013, _eprint: https://onlinelibrary.wiley.com/doi/pdf/10.1002/pssr.201308010.

[187] U. W. Pohl, *Epitaxy of Semiconductors: Introduction to Physical Principles*. Springer Science & Business Media, Jan. 2013.

[188] S. Umehara, N. Pourmand, C. D. Webb, R. W. Davis, K. Yasuda, and M. Karhanek, "Current Rectification with Poly-l-Lysine-Coated Quartz Nanopipettes," *Nano letters*, vol. 6, no. 11, pp. 2486–2492, Nov. 2006.

[189] P. Chen, W. Xu, Y. Gao, P. Holdway, J. H. Warner, and M. R. Castell, "Thermal Degradation of Monolayer MoS2 on SrTiO3 Supports," *The Journal of Physical Chemistry C*, vol. 123, no. 6, pp. 3876–3885, Feb. 2019.

[190] D. Zhou, H. Shu, C. Hu, L. Jiang, P. Liang, and X. Chen, "Unveiling the Growth Mechanism of MoS2 with Chemical Vapor Deposition: From Two-Dimensional Planar Nucleation to Self-Seeding Nucleation," *Crystal Growth & Design*, vol. 18, no. 2, pp. 1012–1019, Feb. 2018.

[191] M. A. Green and S. P. Bremner, "Energy conversion approaches and materials for high-efficiency photovoltaics," *Nature Materials*, vol. 16, no. 1, pp. 23–34, Jan. 2017.

[192] S. Essig, C. Allebé, T. Remo, J. F. Geisz, M. A. Steiner, K. Horowitz, L. Barraud, J. S. Ward, M. Schnabel, A. Descoeudres, D. L. Young, M. Woodhouse, M. Despeisse, C. Ballif, and A. Tamboli, "Raising the one-sun conversion efficiency of III–V/Si solar cells to 32.8% for two junctions and 35.9% for three junctions," *Nature Energy*, vol. 2, no. 9, p. 17144, Sep. 2017.

[193] S. Essig, M. A. Steiner, C. Allebé, J. F. Geisz, B. Paviet-Salomon, S. Ward, A. Descoeudres, V. LaSalvia, L. Barraud, N. Badel, A. Faes, J. Levrat, M. Despeisse,

C. Ballif, P. Stradins, and D. L. Young, "Realization of GaInP/Si Dual-Junction Solar Cells With 29.8% 1-Sun Efficiency," *IEEE Journal of Photovoltaics*, vol. 6, no. 4, pp. 1012–1019, Jul. 2016.

[194] A. Fedorenko, M. A. Baboli, P. K. Mohseni, and S. M. Hubbard, "Design and Simulation of the Bifacial III-V-Nanowire-on-Si Solar Cell," *MRS Advances*, no. 4, pp. 929–936, 2019.

[195] Y. Zhang, M. Aagesen, A. M. Sanchez, R. Beanland, J. Wu, and H. Liu, "GaAsP nanowires and nanowire devices grown on silicon substrates," in *Quantum Sensing and Nano Electronics and Photonics XIV*, vol. 10111. International Society for Optics and Photonics, Jan. 2017, p. 101110X.

[196] C. Himwas, S. Collin, P. Rale, N. Chauvin, G. Patriarche, F. Oehler, F. H. Julien, L. Travers, J.-C. Harmand, and M. Tchernycheva, "In situ passivation of GaAsP nanowires," *Nanotechnology*, vol. 28, no. 49, p. 495707, Nov. 2017.

[197] S. Fujisawa, T. Sato, S. Hara, J. Motohisa, K. Hiruma, and T. Fukui, "Growth and Characterization of a GaAs Quantum Well Buried in GaAsP/GaAs Vertical Heterostructure Nanowires by Selective-Area Metal Organic Vapor Phase Epitaxy," *Japanese Journal of Applied Physics*, vol. 50, no. 4S, p. 04DH03, Apr. 2011.

[198] G. Lopez, "Zep520a spin curves and dilution characterization," p. 4, Dec. 2016.